Electronic Thesis and Dissertation Repository

12-17-2012 12:00 AM

Automatic Assessment of Cardiac Left Ventricular Function Via Magnetic Resonance Images

Mariam Afshin
The University of Western Ontario

Supervisor
Terry Peters
The University of Western Ontario Joint Supervisor
Shuo Li
The University of Western Ontario

Graduate Program in Biomedical Engineering
A thesis submitted in partial fulfillment of the requirements for the degree in Doctor of Philosophy
© Mariam Afshin 2012

Follow this and additional works at: https://ir.lib.uwo.ca/etd

Part of the Biomedical Engineering and Bioengineering Commons

Recommended Citation

AUTOMATIC ASSESSMENT OF CARDIAC LEFT VENTRICULAR
FUNCTION VIA MAGNETIC RESONANCE IMAGES
(Thesis format: Integrated Article)

by

Mariam <u>Afshin</u>

Graduate Program in Biomedical Engineering

Submitted in partial fulfillment
of the requirements for the degree of
Doctorate of Philosophy

The School of Graduate and Postdoctoral Studies
Western University
London, Ontario, Canada

WESTERN UNIVERSITY
School of Graduate and Postdoctoral Studies

CERTIFICATE OF EXAMINATION

Supervisors:

....
Drs. T. M. Peters and S. Li

Supervisory Committee:

....
Dr. Grace Parraga

....
Dr. Gerard M. Guiraudon

Examiners:

....
Dr. Aaron Fenster

....
Dr. James Johnson

....
Dr. Michael Chu

....
Dr. Kaleem Siddiqi

The thesis by

Mariam Afshin

entitled:

**AUTOMATIC ASSESSMENT OF CARDIAC LEFT VENTRICULAR FUNCTION
VIA MAGNETIC RESONANCE IMAGES**

is accepted in partial fulfillment of the
requirements for the degree of
Doctorate of Philosophy

....
Date

....
Chair of the Thesis Examination Board

ii

Abstract

Automating global and segmental (regional) assessments of cardiac Left Ventricle (LV) function in Magnetic Resonance Images (MRI) has recently sparked an impressive research effort, which has resulted a number of techniques delivering promising performances. However, despite such an effort, the problem is still acknowledged to be challenging, with substantial room for improvements in regard to accuracy. Furthermore, most of the existing techniques are labour intensive, requiring delineations of the endo- and/or epi-cardial boundaries in all frames of a cardiac sequence.

On the one hand, global assessments of LV function focus on estimation of the Ejection Fraction (EF), which quantifies how much blood the heart is pumping within each beat. On the other hand, regional assessments focus on comprehensive analysis of the wall motions within each of the standardized segments of the myocardium, the muscle which contracts and sends the blood out of the LV.

In clinical practice, the EF is often estimated via manual segmentation of several images in a cardiac sequence which is prohibitively time consuming, or via automatic segmentation, which is a challenging and computationally expensive task that may result in high estimation errors. Additionally, the diagnosis of the segmental dysfunction is based on visual LV assessment, which is subject to high inter-observer variability.

In this thesis, we propose accurate methods to estimate both global and regional LV function with minimal user inputs in real-time from statistics estimated in MRI. From a simple user input, we build image statistics for all the images in a subject dataset. We demonstrate that these statistics are correlated with regional as well as global LV function. Different machine learning techniques have been employed to find these correlations. The regional dysfunction is investigated in terms of a binary/multi-classification problem.

A comprehensive evaluation over 20 subjects demonstrated that the estimated EFs correlated very well with those obtained from independent manual segmentations. Furthermore, comparisons with estimating EF based on recent segmentation algorithms showed that the pro-

posed method yielded a very competitive performance. For regional binary classification, we report a comprehensive experimental evaluation of the proposed algorithm over 928 cardiac segments obtained from 58 subjects. Compared against ground-truth evaluations by experienced radiologists, the proposed algorithm performed competitively, with an overall classification accuracy of 86.09% and a kappa measure of 0.73. We also report a comprehensive experimental evaluation of the proposed multi-classification algorithm over the same dataset. Compared against ground-truth labels assessed by experienced radiologists, the proposed algorithm yielded an overall 4-class accuracy of 74.14%.

Acknowlegements

I owe this success to a number of people without whom none of this would have been possible.

I would like to express my sincere thanks to my supervisors Dr. Terry Peters and Dr. Shuo Li for all their help and encouragements throughout my program. I would like to thank Dr. Peters for giving me the opportunity to be part of his group and supporting me during last four years. I also, would like to thank Dr. Shuo Li for giving me the opportunity to join Biomedical Engineering program at Western, believing in me and pushing me to achieve goals that I sometimes considered unachievable.

Special thanks to Dr. Ismail Ben Ayed whose expertise was crucial to my success. I thank Ismail for inspiring and challenging me, and for sharing his research insight and passion with me during my Ph.D. I thank Dr. Kumaradevan Punithakumar and Dr. Max Law for sharing their vast technical knowledge and experience with me.

I would like to thank my advisory committee members, Dr. Grace Parraga and Dr. Gerard Guiraudon for their continuous support and positive feedbacks. During my advisory meetings, they motivated me to learn and overcome the technical challenges.

I would like to thank all the lab members in Dr Peters' group as well as members in Digital Imaging Group of London. Also, thanks to my wonderful friends for their help.

Last, but not least, special thanks to my family especially my father, my mother, my brother, my sister and my nephews, Hossein and Kamyar, for their unconditional love and support in every step of my life. Thanks for encouraging me to follow my dreams. Huge thanks to my boyfriend Pouyan whose love is the reason I start everyday with a smile. Thanks for your continuous love and support.

Contents

List of Figures

xiv

xv

List of Tables

List of Abbreviations

2D   Two-Dimensional

3D   Three-Dimensional

HF   Heart Failure

LV   Left Ventricle

RV   Right Ventricle

LA   Left Atrium

RA   Right Atrium

MRI   Magnetic Resonance Imaging

CMR   Cardiac Magnetic Resonance

RF   Radio Frequency

MR   Magnetic Resonance

SSFP   Steady-State Free Precession

CT   Computed Tomography

EF   Ejection Fraction

AHA   American Heart Association

IHD   Ischemic Heart Disease

LVEF   Left ventricular Ejection Fraction

GMM   Gaussian Mixture Model

ROI   Region Of Interest

ASM   Active Shape Model

PDF   Probability Density Function

PCA   Principal Component Analysis

AAM   Active Appearance Models

ANN   Artificial Neural Network

HMM   Hidden Markov Model

SDE   Shannons Differential Entropy

ICA   Independent Component Analysis

LDA   Linear Discriminant Analysis

LSVM   Linear Support Vector Machine

SVM   Support Vector Machine

FIESTA   fast-imaging employing steady-state acquisition

ROC   Receiver Operating Characteristic

AUC   Area Under the Curve

List of Appendices

Chapter 1

Introduction

Cardiovascular disease in general is the leading cause of death worldwide [17], and Heart Failure (HF), in particular is a prevalent disease that can be caused by various heart conditions [9]. Clinically, HF has a poor prognosis and its early stage diagnosis can play an essential role for radiologists in planning the stages of the treatment. Since some patients require specific treatment, early and accurate diagnosis of HF is very important. Approximately 25% of patients with HF diagnosis are re-admitted to hospitals and 40% of them die within one year following the first hospitalization. Furthermore, early and accurate diagnosis can lead to more effective treatment, reducing the re-hospitalization rate and, consequently, decrease the associated financial burden on the public healthcare system [17].

1.1   Heart Failure

The heart is considered as the engine of the body that continuously pumps oxygenated blood to the cells (Fig. 1.1) [1]. Body cells function properly when they receive sufficient nutrient-rich blood. When a patient suffers from a serious HF condition, his heart may not be able to provide the required nutrition for the cells to function properly.

The heart consists of four chambers: the left and right ventricles and the left and right atria.

---

[1]please refer to: http://lsa.colorado.edu/essence/texts/heart.html

HF occurs under one or a combination of the following conditions:

- The Left Ventricle (LV) muscle, the myocardium, is too weak to pump an adequate amount of blood (systolic heart failure) in each heart beat;

- The LV is not sufficiently filled with blood (diastolic heart failure) in each cycle;

- An insufficient amount of blood is supplied to the heart as a result of coronary artery disease, particularly due to a narrowing of coronary arteries; and

- An infection weakens the heart muscle (cardiomayopathy).

There are also less common situations such as congenital heart disease, heart valve disease and some types of abnormal heart rhythms (arrhythmia) that may lead to HF [2].

---

[2]Please refer to: http://www.nlm.nih.gov/medlineplus/ency/article/000158.htm
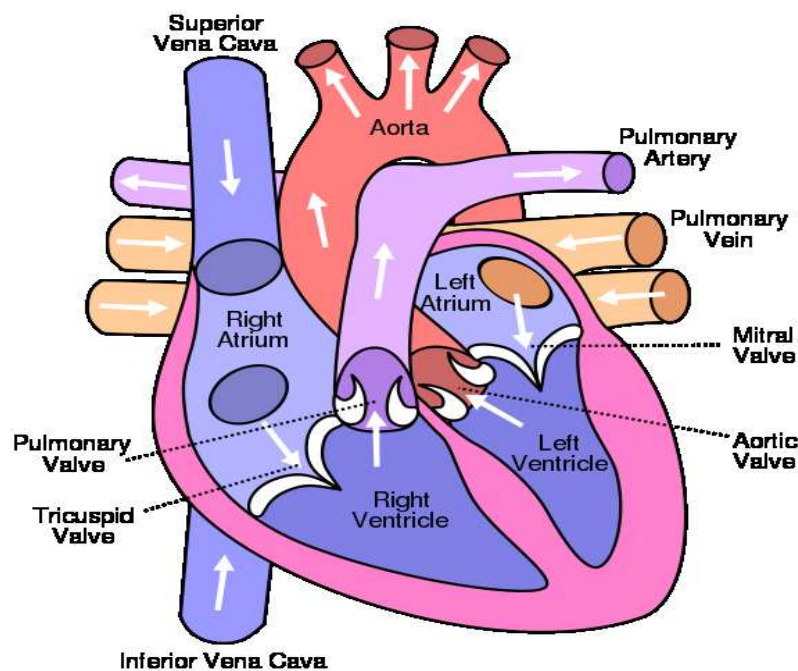
Figure 1.1: Blood Circulation. The figure is adopted from:
http://en.wikipedia.org/wiki/Circulatory_system

1.2 Blood Circulation

The heart is slightly larger than a fist, continuously pumping the blood through out the body. The ventricles are the two main chambers of the heart that receive and send blood. The Right Ventricle (RV) pumps the blood to the lungs and the left ventricle (LV), pumps the blood to the whole body in each heart beat. The ventricles have thicker walls and generate higher blood pressures comparing to the atria. Since the LV is required to pump the blood to the whole body, its wall is thicker compared to the RV. Therefore, early and precise diagnosis of left ventricular abnormalities plays an essential role in taking the treatment steps following prognosis.

When the heart contracts, it pushes the blood out into two major loops: a systemic loop happens when oxygenated blood is circulated into the body and wasted carbon dioxide is collected from cells; pulmonary loop happens when the blood circulates to and from the lungs in order to release the carbon dioxide and pick up new oxygen. The systemic loop is controlled by the left side of the heart where the pulmonary loop is controlled by the right side.

The systemic loop begins when oxygenated blood from the lungs enters the the upper left chamber, called the Left Atrium (LA). When the LA is filled, the mitral valve is opened by high blood pressure and blood flows down into the LV. When the LV contracts in each heart beat, it pushes the blood into the aorta, the largest artery of the body (usually 2 to 3cm wide). The oxygenated blood leaving the aorta brings oxygen to the body cells through a network of arteries and capillaries. The de-oxygenated blood from body cells returns to the heart via the venous system. All de-oxygenated blood from the body returns to the heart by two large veins called superior and inferior vena cavae. The superior vena cava receives blood from upper organs of the body, while the inferior vena cava receives blood from the lower ones. Both of these veins fill the blood into the Right Atrium (RA). The pulmonary loop begins by sending the blood from the RA to the RV through the tricuspid valve. When the RV contracts, blood is pushed into the pulmonary artery. The fresh, oxygen-rich blood returns to the LA of the heart through the pulmonary veins (refer to Fig. 1.1).

Both of the circulatory system loops occur simultaneously. The contraction of the heart muscle begins from the two atria, which forces the blood into the ventricles. Then the walls of the ventricles contract together at the same time, pumping the blood out into the arteries. The aorta delivers the oxygenated blood to the body, and the pulmonary artery sends the blood to the lungs to be oxygenated. Afterwards, the heart muscle relaxes, allowing the blood to flow in from the veins, filling the atria again for the next cycle. The heart rate is about 72 beats per minute in a healthy individual, but can be increased or decreased in different situations. It takes about 30 seconds for each portion of the blood to complete a full cycle (from lungs to the heart and the heart to the body, from body back to the heart and out to the lungs again).

1.3 Cardiovascular Magnetic Resonance Imaging

Magnetic Resonance Imaging (MRI) is a non-invasive imaging technique that plays an essential role assessing heart conditions before and following a HF by providing accurate and reproducible diagnostic information. It is therefore considered as the gold-standard imaging modality for comprehensive assessments of regional and global dysfunctions of the heart [6].

Cardiac Magnetic Resonance (CMR) Images are commonly acquired at a magnetic field strength of 1.5 T (3.0 T in some centers) [6]. This strong constant magnetic field is applied to align the magnetization of hydrogen atoms of the organ being scanned. The hydrogen nuclei are then excited by applying another magnetic field at a certain frequency (RF field) that deflects their magnetization from this alignment. The signal emitted from these excited nuclei, when they realign to their initial configuration, is measured by RF sensors and used to form an image. In MR imaging, signals received from a particular tissue (e.g., heart muscle, fat, etc) are determined by the density of hydrogen atoms (proton density), and by two distinct MR relaxation parameters, longitudinal relaxation time (T1) and transverse relaxation time (T2). Proton density, T1, and T2 are significantly varied for different tissue types, and are used to generate contrast in MR images. Also, image contrast can be modified by modulating the way the radiofrequency signals are applied (the MR sequence) [6].

An MR Imaging sequence refers to a specific combination of radiofrequency pulses, magnetic gradient field switches, and timed data acquisitions, all used to generate the MRI image. In CMR, for anatomic imaging and tissue characterization, spin echo sequences are used, whereas gradient echo sequences are used to acquire cine images which depict fat and blood with high signal intensities. The most recent standard protocol for cardiac MR employs the Steady-State Free Precession (SSFP) sequence. This sequence provides the best contrast between myocardium (dark) and the blood in the chamber (white) for imaging cardiac function. For a better visualization, fat suppression sequences may be applied to allow signal from fat to be specifically suppressed with special pre-pulses [6].

To assess heart function, a full cardiac cycle is divided into 20-30 frames, each consisting of

10-12 slices corresponding to a specific plane of the heart. The standard imaging plane (short axis view) used for LV assessments is perpendicular to the long axis of the heart (apex-base). A single cardiac MRI can therefore consist of around 200-250 short axis images, making the analysis of such a volume of data quite challenging [6].

1.3.1 Clinical significance of using Cardiovascular Magnetic Resonance Imaging

Cardiac MRI can image in any desired plane and with a nearly unrestricted field of view, allowing the flexibility to evaluate abnormal structure of ventricles with different sizes and shapes, even those that have been extensively remodeled [22, 19]. The inherent 3-dimensional nature of CMR makes it suitable for studying the RV, which is challenging to assess due to its complex and variable morphology. Moreover, using steady-state free-precession sequences, CMR is suitable for regional assessments of the LV because it provides excellent intensity contrast between blood and myocardium [18]. With regard to regional ventricular function, CMR enables accurate assessments of regional wall motion abnormalities [18].

Since CMR is accurate and reproducible [7, 12, 8] patients can undergo several CMR scans without being exposed to ionizing radiation [20], making it an ideal technique for monitoring disease treatment and progression.

It is predicted that the application of CMR imaging for patients with HF will be substantially developed in the coming years [20]. Furthermore, improvements in developing CMR software and hardware will lead to shorter scan time and, eventually, allow the use of real-time imaging with higher spatial and temporal resolution [20].

1.3.2 Cardiovascular Magnetic Resonance Imaging Safety

In CMR scanning, the patient is not exposed to ionizing radiation, and there are no other harmful side effects reported. However, there are certain safety protocols to be followed regarding

to the proximity of a strong magnetic field. Items with ferromagnetic materials can be pulled into the magnet's core with high speed, and cause serious damage that restricts application of some equipments. However, the majority of medical implants are safe for MR scans, including orthopedic implants, coronary and vascular stents, and prosthetic cardiac valves. Patients with embedded ferromagnet implants such as pacemakers or defibrillators cannot be admitted for MR scanning [20]. Currently, there are many researches on MR compatible implants and devices that can change the development of MR machines in the future. However, when MR compatibility of a certain device is not clear, its safety status needs to be checked by referring to the information provided by the corresponding manufacture [6].

1.4 Diagnosis of Cardiovascular disease

The diagnosis, treatment and follow-up of LV pathologies can rely on numerous cardiac imaging modalities, which include echography, CT (Computed Tomography), coronary angiography and MRI (cardiac Magnetic Resonance Imaging). Among others, MRI provides precise information on morphology, tissue viability, muscle perfusion and blood flow, using suitable protocols [13].

In clinical practice, however, assessment of the LV relies mainly on manual segmentations as well as visual analysis and interpretations of wall motion. Several clinical studies have shown that visual assessments are inaccurate and subject-dependent [11]. Manual segmentation of the LV is prone to intra- and inter-observer variability, therefore, automatic assessment methods have become a major area of research [13].

Assessment of the LV includes three main steps:

1. **Global assessment of the LV:** This performed by estimating the cardiac Ejection Fraction (EF), which is the most important observations in diagnosing cardiovascular diseases because it is an important indicator of long-term prognosis for patients with coronary artery disease. Since the LV is the main pumping chamber of the heart, the EF is usually measured using information from the LV [20].

   In current clinical practice, the EF is often estimated from several images in a cardiac sequence using manual segmentation of the LV cavity, which is time consuming. Automatic LV segmentation can also be used to compute the EF, however, the automatic LV segmentation techniques are challenging and computationally expensive.

2. **Regional assessment of the LV:** This is scored following the American Heart Association (AHA) Standard. Heart failure is a prevalent disease that can be caused by various heart conditions, in particular, Ischemic Heart Disease (IHD) [6]. The decrease of blood supply produced by coronary artery stenosis impairs the contractile properties of specific myocardial areas. This causes a deviation from the normal regional wall motion and con-

tractility patterns of the myocardium, especially the LV. Early and accurate detection of LV regional wall motion abnormalities significantly helps in the diagnosis and follow-up of IHD [1].

In routine clinical use, cardiac function is estimated by visual assessment of the LV motion and, therefore, it is highly observer-dependent. Alternatively, computer-aided detection systems have been attempted in recent years in order to automatically analyze LV myocardial function quantitatively [20], and to classify cardiac function into normal or abnormal groups [51]. The regional myocardial function is commonly scored by following AHA standards [2], where the LV is divided into 17 segments.

3. **Classification of regional LV dysfunction:** Segmental classification of the LV is widely accepted as a predictor of cardiac disease [1]. Clinically, the regional myocardial function is also scored using AHA standards [2]. Representative 2D cardiac slices are selected to generate 17 standard LV regional segments. Each of the regional segments are assessed individually and characterized as: *normal, hypokinesia, akinesia or dyskinesia*. Distinguishing these conditions from each other is often challenging as manual delineation of regional segments or visual assessment is used in clinical routine which is highly subject dependent and non-reproducible [53, 5]. Functional images are subject to noise, therefore LV segmentation and regional assessment are acknowledged as difficult problems. The difficulties come from the subtle visual differences between normal- and abnormal-segment motions.

In this project, we propose novel methods to diagnose global and regional dysfunction of cardiac LV using MR images, to provide a framework that will assist the radiologists in the diagnosis of LV dysfunction in early stages.

1.5 Global Assessment of Cardiac Left Ventricular Function

During the cardiac cycle, the heart contracts (systole) and relaxes (diastole). When the heart contracts, it pushes the blood out of the ventricles and when it relaxes, the ventricles are refilled with blood. Ejection Fraction (EF) is a measure of how much blood pumps out of the LV with each heart beat.

Left ventricular Ejection Fraction (LVEF) is an important prognostic marker used to evaluate cardiac function globally [20]. Cardiac Magnetic Resonance (CMR) imaging provides accurate and reproducible methods to perform physiological studies such as EF estimation. EF is often estimated using multiple cine short -axis MR images that embrace the LV. Currently in clinical practice, EF is estimated from several images in a cardiac sequence using manual segmentation, i.e., manual delineation of the LV cavity. This is a time consuming process, which requires about 20 to 40 min per ventricle by a clinician and is prone to intra- and inter-observer variability. Automatic LV segmentation techniques for computing the EF has been the subject of significant research. In particular, commercial software packages such as MASS (Medis, Leiden, The Netherlands) [17] and Argus (Siemens Medical Systems, Germany) [46] are today available for automatic ventricle delineation. Although processing time has been greatly reduced, the provided contour detection still needs improvement compared to equal manual contour delineation. Existing LV segmentation algorithms can be divided into the following two main categories based on prior art [13].

1.5.1 Left Ventricle segmentation based on no or weak priors:

In general, LV segmentation approaches with no or weak priors are image-driven. Existing algorithms are based on thresholding [18, 29, 62, 45, 28, 35], dynamic programming [15, 64, 17], shortest path algorithms [23], pixel classification via Gaussian Mixture Models [48] or clustering [10], and deformable models which evolve and regularize a curve following the minimization of a functional [24, 63, 41, 3]. Based mainly on image information, these

approaches do not require intensive training. However, in order to compensate the lack of spatial information, they generally resort to user interventions or several pre- or post-processing steps to localize the LV. This section summarizes segmentation methods with weak or no prior, including image-based, pixel classification-based and deformable models.

Image-Based Methods

The majority of the image-based methods involve a two-steps process to individually segment the endo and epicardium [13]. The first step focuses on detecting the endocardial boundary using thresholding [18, 29, 62, 45, 28, 35] or dynamic programming [17, 19, 32]. The epicardial boundary is delineated during the second step, often based on the endocardium boundary using a spatial model. The model utilizes information about myocardial thickness or mathematical morphology operators.

Pixel Classification

Pixel classification methods are often used when multiple images of the same organ are available, e.g., multiple MRI or multi-modality images. The image is divided into different regions or classes that have similar feature values. Segmentation can be performed using either supervised (with learning datasets) or unsupervised techniques (without training datasets). In [48], Pednekar *et al.* used Gaussian Mixture Model (GMM), to fit the image histogram, and clustering.

Deformable Models

Segmentation methods based on deformable models use active contours or snakes [27], and are based on deforming a curve iteratively to minimize an energy function. The energy function consists of two main components; a regularization term controlling the smoothness of the curve and a data term that includes information about object boundary. The curve evolution equation is obtained by the Euler-Lagrange descent minimization of energy function. For im-

plementation of curve evolution, the level-set framework is widely used in medical imaging because of its flexibility regarding topological changes. The level-set method facilitates segmentation of multiple objects. Deformable models have been used widely for LV segmentation [24, 63, 41, 3].

Almost all of the methods using weak priors or none at all require user intervention. In order to fully automate the process, incorporating strong spatial priors (e.g. relating to the the shape of the target region) has been researched for LV segmentation. Section 1.5.2. discusses some of the existing methods within this direction.

1.5.2 Left Ventricle segmentation based on strong priors

Automatic LV segmentation is generally based on strong spatial priors such as statistical shape models or atlases. This is especially true if the shape of the target region does not change significantly from one subject to another, which is a reasonable assumption for the LV. Such strong priors can relax the need for user intervention, but at the expense of manually building a large training set. Methods falling within this category are based on shape-driven deformable models [47, 36, 39, 40], Active Shape Models (ASM) [66, 65], and atlas based models [37, 68].

Shape-driven Deformable Models

Shape-driven deformable models evolve an active curve/surface according to the minimization of an energy functional, comprising a set of template shapes learned *a priori*. The evolution equation is computed by minimization of the functional, which contains a statistical shape constraint. The principle is to modify the energy functional by adding a new term that embeds a shape constraint, such as a distance to a reference shape model, e.g., the mean signed distance map as used by Paragios et al. to build a reference shape [47, 36]. A Probability Density Function (PDF) or probabilistic map can be estimated by using manual LV segmentations, and can be used in the evolution equation [39].

13

Active Shape Models

The Active Shape Model (ASM) consists of two steps: (1) building a statistical shape model following a Principal Component Analysis (PCA) of a set of aligned training shapes, and (2) finding a segmentation in the current image by fitting the solution to the learned model and estimating rotation, translation and scaling parameters [66, 65, 4]. Active Appearance Models (AAM) are an extension of ASM by modeling gray levels [13] that include both shape and texture variability in the training set.

Atlas Based models

In atlas based methods, an image is segmented by mapping its coordinate space to that of an atlas, often following a registration process. This technique has been used for heart segmentation [37, 67, 11]; the principle is to register the labeled atlas onto the image to be segmented, and then apply the obtained transformation to the atlas, thereby obtaining the final result. The result can then be propagated over time throughout the cardiac cycle following the same principle.

1.5.3 The Proposed Method

In this project, we propose estimating the EF without segmentation in real-time directly from image statistics using machine learning techniques. From a simple user input in only one image, we build a statistic based on the Bhattacharyya coefficient [14] of similarity between image distributions for all the images in a subject dataset . We demonstrate that these statistics are non-linearly related to the LV cavity areas and, therefore, can be used to estimate the EF via an Artificial Neural Network (ANN) directly. The proposed method consists of four main steps:

1. Image acquisition

2. Building Image Statistics

3. Applying Artificial Neural Networks

4. Estimating Ejection Fraction

1.6 Regional Assessment of Cardiac Left Ventricular Function

Accurate detection of segmental (regional) LV abnormalities in MRI is accepted as a predictor of cardiac diseases, the leading cause of death worldwide [6]. In clinical practice, segmental cardiac function (Fig. 1.2) is considered an essential diagnosis and follow-up component [1]. It is often assessed *visually* following the AHA standard [2], which prescribes selecting representative 2D cardiac slices used to generate 17 standardized LV segments. Currently radiologists visually assess the 17 segments together. These practices, along with being subject to high inter-observer variability [5, 53], and are subjective and non-reproducible. For instance, the clinical study in [5] showed that the mean kappa measure of detecting regional wall motion abnormalities by three different radiologists could be as low as 0.43, the difficulties coming from the subtle visual differences between normal- and abnormal-segment motions. Automatic diagnosis of LV regional dysfunction has attracted significant research [15, 11, 21, 4, 14, 10]. Regardless of promising performances of the applied techniques, the results can still be improved in terms of accuracy. For instance, the recent publication in [21] reports an accuracy of 63.70% (base), 67.41% (middle), and 66.67% (apex) when visual wall motion scoring is used as reference.

1.6.1 Prior art

Echocardiography Based Methods

Most of the pioneering studies of wall motion abnormality detection targeted echocardiography [3, 9, 12], using concepts from shape statistics [3, 9] and Hidden Markov Models (HMM) [12], among others. In [3], model-based shape analysis is used to automatically classify wall motion abnormalities in echocardiograms. The shape model is obtained using Principle Component Analysis (PCA), which quantifies the components of the variability within a large data set.
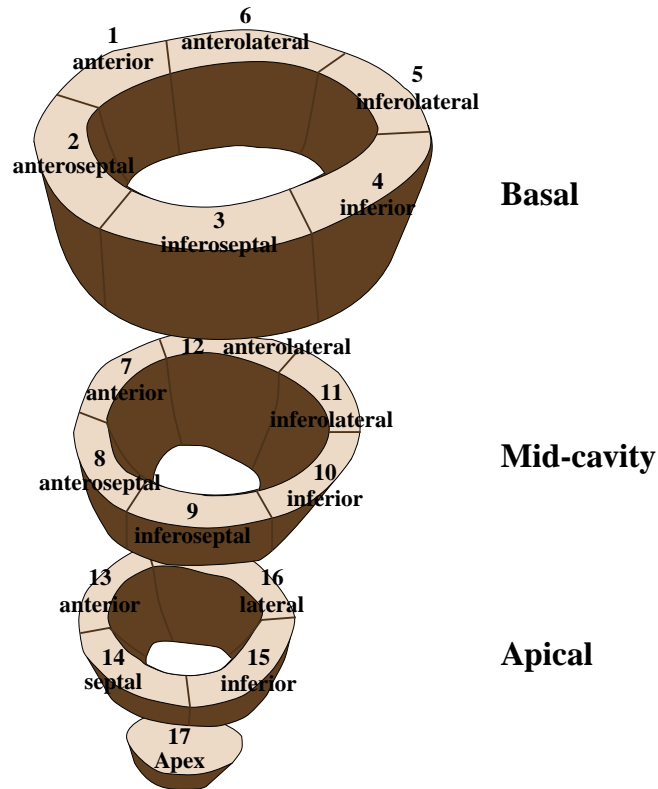
Figure 1.2: AHA standard for LV regional segments.

In this particular example, they used PCA to find the average endocardial shape and large eigenvectors representing the main modes of variations. Any shape in the testing dataset can be represented by a combination of average shapes and a specific linear combination of these eigenvectors. The eigenvectors correspond to regional wall motion abnormality. Multivariate linear regression was then applied to differentiate normality and abnormality of the regional segments.

In [9], the authors built sparse shape models with localized variations from four- and two-chamber echocardiographic sequences using principal component analysis and orthomax rotations. Then, the ensuing shape parameters were used to assess local wall motion.

In [12], Mansor et.al. investigated a HMM as a tool for regional stress cardiography wall motion abnormality detection. HMM are especially known for their application in temporal pattern recognition [22] because of their ability to successfully learn the time-varying characteristics of signals. HMM were used so that the cardiac data inherits the time-varying and

sequential properties. First, the myocardial contour was semi-automatically delineated using Quamus software. Next, each contour was divided into six parts, and several features were extracted to evaluate the wall motion. The data was then separated into two groups of normal and abnormal subjects. Two HMMs were then developed for each segment. Finally, the trained HMM was used to evaluate regional wall motion for the new dataset.

Magnetic Resonance Imaging Based Methods

More recently, MRI-based wall motion abnormality detection has been studied [15, 11, 21, 4, 14, 10]. In [14], Punithakumar et al. characterized myocardial-segment motions via a nonlinear dynamic model, and used the Shannon's differential entropies of various segment features (e.g., areas and radial distances) as inputs of a naive Bayes classifier. They investigated the problem with a global measure based on the Shannon's Differential Entropy (SDE) of distributions of normalized radial distances, radial velocities and segment areas. As discussed in [14], SDE measures global distribution information, and is more discriminative in classifying distributions compared to the methods that rely on elementary measures or a fixed set of moments.

In [21, 19], Suinesiaputra et al. built normokinetic myocardial shape models using short-axis MR images acquired from healthy volunteers. They proposed using an Independent Component Analysis (ICA) classifier that detects and localizes abnormally contracting segments, via a characterization of local shape variations.

Lekadir et al. [10] focused on statistical modeling based on spatio-temporal inter-landmark relationships.

In [11], Lu et al. proposed a pattern recognition technique built upon intra-segment correlation, using a normalization scheme which maps each LV slice to polar coordinates with fixed size, intensity level, and position.

The study in [4] proposed a differentiable-manifold analysis, following differential geometry concepts to define a parameterization of the LV domain, which is considered as a deforming

manifold.

The authors of [15] investigated a tensor-based Linear Discriminant Analysis (LDA) classification that conserves the spatio-temporal structure of the myocardial function. Radial and circumferential strain as well as tissue-rotation angle were used as features to train and test a classifier via manual segmentations of the myocardium.

Most of the existing methods require delineations of the endo- and/or epi-cardial boundaries in all frames of a cardiac sequence, using either a manual time-consuming process [4, 21, 11, 15] or an automatic/semi-automatic segmentation (delineation) algorithm [14]. As discussed in section 1.5. segmentation algorithms are either sensitive to user inputs and/or are computationally expensive and may result in high estimation errors [13]. Furthermore, the segmentation results often depends on the choice of parameters and training dataset. These difficulties inherent to segmentation algorithms prevent their clinical adoption for segmental motion abnormality detection. Moreover, some of the existing algorithms, e.g., those based on shape analysis techniques [21], require such delineations in the training phase, which increases the amount of manual input and training complexity.

1.6.2 The Proposed Method

In this thesis, we propose a regional myocardial abnormality detection framework based on image statistics. The proposed framework requires minimal user interaction, with the clinician only needing to specify initial delineation and anatomical landmarks on the first frame. Approximations of regional myocardial segments in subsequent frames were systematically obtained by superimposing the initial delineation on the rest of the frames. The proposed method exploits the Bhattacharyya coefficient to measure the similarity between the image distribution within each segment approximation and the distribution of the corresponding user-provided segment. Linear Discriminant Analysis (LDA) is applied to find the optimal direction along which the projected features are the most descriptive. Then a Linear Support Vector Machine (LSVM) classifier is employed for each of the regional myocardial segments to automatically

detect abnormally contracting regions of the myocardium. Based on a clinical dataset of 58 subjects, the evaluation demonstrates that the proposed method can be used as a promising diagnostic support tool to assist clinicians. The proposed method consists of four main steps:

1. Image acquisition

2. Building Image Statistics

3. Applying Linear Discriminant Analysis

4. Detecting Abnormality of Regional Segments

1.7 Multi-Class Segmental Cardiac Dysfunction Classification of Cardiac Left Ventricular Function

In routine clinical procedures, segmental cardiac function is considered an essential diagnosis and follow-up component [1]. It is commonly scored following the AHA standard [2] which prescribes dividing the LV into 16 regional segments, each assessed individually and characterized as:

- normal

- hypokinesia: reduced LV contraction

- akinesia: absence of contraction

- dyskinesia : bulging out in systole

Current radiologic practices rely on visual assessment, which is subject to a high inter-observer variability, while being subjective and non-reproducible [53, 5]. Furthermore, visual assessment requires either manual delineation of the segments in all the frames of a subject dataset, which is prohibitively time-consuming, or automatic delineation, which is a challenging computational problem [13].

1.7.1 Prior Art

Automating LV abnormality scoring has been the subject of numerous recent studies as discussed in section 1.6 [19, 4, 14, 2, 21, 15, 12]. Earlier studies of wall motion abnormality detection used various approaches including differentiable manifolds [4], independent component analysis classification [21], information-theoretic techniques [14], tensor-based classification [12], and image statistics based classification [2].

Unfortunately, to the best of our knowledge, all existing algorithms address a *binary* classification problem, where each cardiac segment is characterized as normal or abnormal. Fur-

thermore, most of the existing methods require LV segmentation in all frames of a cardiac sequence. As noted earlier, this is either done manually which is time consuming or automatically with its associated drawbacks [4, 21, 15]).

1.7.2 The Proposed Method

We propose a method to solve this problem using image statistics from MR images. The proposed method requires minimal user-interaction with the clinicians only needing to delineate the inner and outer boundary and two anatomical landmarks of the LV in one single frame of cine MRI sequence. The obtained outer boundary is then systematically superimposed to all other corresponding frames with no changes. The amount of blood inside the regional LV cavity is modeled by Bhattacharyya statistics between distribution estimated inside the LV cavity of first frame and regional segments in the rest of the frames. The muscle inside the regional LV is modeled using the same idea from Bhattacharyya statistics between distributions estimated inside the LV myocardium of the first frame and regional segments in the rest of the frames. A Support Vector Machine (SVM), is then used to find the correlation between the estimated image statistics and different regional abnormalities of the LV. The results show that the image statistics can be used to differentiate among various LV abnormalities. The algorithm shows comprehensive results on $174 * 20$ short axis segments, obtained from 58 subjects. The method diagnoses the condition of LV regional segments with 74.14% accuracy. The proposed method consists of four main steps:

1. Image acquisition

2. Building Image Statistics

3. Applying Support Vector Machine

4. Classifying LV Regional Segment Dysfunction

1.8   Thesis Objectives

The main objective of this work is to provide a platform to assist radiologists in diagnosis of LV abnormalities. We developed a new automated tool to mimic the different steps of the diagnostic procedures, to automatically assess cardiac function. This platform has the potential to be further developed into a product for diagnosis of cardiac dysfunction, providing radiologists with an accurate and fast system that can be integrated with MRI scanners.

Specific research objectives are listed below:

- Develop a software system for the diagnosis of LV dysfunction that would be compatible with MRI scanners.

- Provide clinicians with a fast and accurate diagnostic tool that assesses the LV function globally with a minimal user input.

- Presenting MRI features that could be used to directly assess cardiac functions in terms of global dysfunction without the need for segmentation.

- Develop a tool to estimate the regional cardiac function automatically with a minimum user-intervention.

- Speed up the procedure of automatically assessing segmental LV by removing the need for segmentation while exceeding the accuracy of current systems.

- Classify LV segmental dysfunction to diagnose abnormality.

1.9 Thesis Outline

1.9.1 Chapter 2: Global Assessment of Cardiac Left Ventricle Function Using Estimation of Ejection Fraction

This chapter describes how we design a diagnostic tool for global assessment of cardiac function using estimation of EF. In clinical routine, EF is often estimated by either manual or automatic segmentation of the LV in number of short axis CMR Images. In general, the segmentation algorithms discussed in section 1.5 require careful user interventions and/or intensive manual training, along with a heavy computational load. Furthermore, the ensuing segmentation results depend significantly on the choice of a set of parameters and training data, causing high errors in the EF estimation. These difficulties inherent to segmentation algorithms limit the automatic estimation of the EF in routine clinical use.

While existing techniques are labour intensive, we believe that there are other characteristics of the images that can be computed with less effort, but that nevertheless correlate with the EF. One such technique that we describe in chapter two is based on machine learning technique, which removes the need for image segmentation. We build an image statistic for every image in a subject dataset using a simple user input in a single image. We show that there is a non-linear relation between these statistics and the LV cavity areas (cf. Figs. 2.7 -2.12). Therefore the EF can directly be estimated using the statistics in *real-time* via an Artificial Neural Network (ANN). We Perform a comprehensive evaluation on 20 subject datasets and demonstrate that the estimated EFs are very well correlated with those obtained from manual segmentations.

1.9.2 Chapter 3: Regional Assessment of Cardiac Left Ventricle Function

Regional assessment of cardiac LV function is based on the segmentation of the LV in either the entire cardiac cycle or several frames. Indeed, there are other image characteristics that can be estimated with minimum user interaction. These characteristics correlate with segmental cardiac dysfunction. One such technique that we describe in chapter three is based on image features and machine learning, which removes the need for delineating the endo- and epicardial boundaries in all the images of a cardiac sequence. Starting from a minimum user input in only one frame in a subject dataset, we build, for all the regional segments and all subsequent frames, a set of statistical MRI features based on a measure of similarity between distributions. We demonstrate that, over a cardiac cycle, the statistical features are related to the proportion of blood within each segment. Therefore, they can characterize segmental contraction without the need for delineating the LV boundaries in all the frames. We first find the optimal direction along which the proposed image features are most descriptive via Linear Discriminate Analysis (LDA). Then, using these results as inputs to a Linear Support Vector Machine (LSVM) classifier, we obtain an abnormality assessment (normal/abnormal) of each of the standard cardiac segments in real-time. We report a comprehensive experimental evaluation of the proposed algorithm over 928 cardiac segments obtained from 58 subjects. Compared against ground-truth evaluations by experienced radiologists, the proposed algorithm yielded a competitive performance, with an overall classification accuracy of 86.08% and a kappa measure of 0.73.

1.9.3 Chapter 4: Multi-Class Segmental Cardiac Dysfunction Classification

The purpose of this chapter is to investigate the more general and challenging *multi-class* problem, where each regional segment is classified into one of four classes: (1) normal; (2) hypokinetic; (3) akinetic; and (4) dyskinetic. We obtain a simple user input from a single frame for

the given subject. Using this input we build for all the regional segments and all subsequent frames a set of statistical MRI features based on a measure of similarity between distributions. Over a cardiac cycle, these statistical features are related to the proportion of blood and myocardium within each segment, and can therefore characterize segmental cavity/myocardium contraction without the need for delineating the LV boundaries in all the frames. Finally, using these features as inputs to a multi-class Support Vector Machine (SVM) classifier, we obtain a 4-class assessment of each segment. We report a comprehensive experimental evaluation of the proposed algorithm over 928 cardiac segments obtained from 58 subjects. Compared to ground-truth labels assessed by an experienced radiologist, the proposed algorithm yielded an overall 4-class accuracy of 74.14%.

1.9.4 Chapter 5: Summary, Contribution and Future Directions

This chapter summarizes the contribution of this project, and discusses the limitations were faced at different stages. Suggestions and future directions are included to extend this project to be improved and applied as a clinical diagnostic tool to help clinicians.

References

[1] H. Abdel-Aty, O. Simonetti, and M. G. Friedrich, "T2-weighted cardiovascular magnetic resonance imaging," *Journal of Magnetic Resonance Imaging*, vol. 26, no. 3, pp. 452–459, 2007.

[2] M. Afshin, I. Ben.Ayed, K. Punithakumar, M. W. K. Law, A. Islam, A. Goela, I. G. Ross, T. M. Peters, and S. Li, "Assessment of regional myocardial function via statistical features in MR images," in *Medical Image Computing and Computer-Assisted Intervention; MICCAI*, 2011, pp. 107–114.

[3] B. R. Annuar, C. K. Liew, S. P. Chin, T. K. Ong, M. T. Seyfarth, W. L. Chan, Y. Y. Fong, C. K. Ang, N. Lin, H. B. Liew, and K. H. Sim, "Assessment of global and regional left ventricular function using 64-slice multislice computed tomography and 2d echocardiography: A comparison with cardiac magnetic resonance," *European Journal of Radiology*, vol. 65, no. 1, pp. 112 – 119, 2008.

[4] I. Ben Ayed, K. Punithakumar, A. Islam, J. Chong, and S. Li, "Left ventricle segmentation via graph cut distribution matching," in *Medical Image Computing and Computer-Assisted Intervention; MICCAI*, vol. 5762, 2009, pp. 901–909.

[5] I. Ben Ayed, I. Ross, and S. Li, "Embedding overlap priors in variational left ventricle tracking," *IEEE Transaction on Medical Imaging*, vol. 28, no. 12, pp. 1902–1913, 2009.

[6] G. S. Bleumink, A. M. Knetsch, M. C. Sturkenboom, S. M. Straus, A. Hofman, J. W. Deckers, J. C. Witteman, and B. H. Stricker, "Quantifying the heart failure epidemic: Preva-

lence, incidence rate, lifetime risk and prognosis of heart failure - the rotterdam study," *European Heart Journal*, vol. 25, pp. 1614–1619, 2004.

[7] J. G. Bosch, F. Nijland, S. C. Mitchell, B. P. Lelieveldt, O. Kamp, J. H. Reiber, and M. Sonka, "Computer-aided diagnosis via model-based shape analysis: Automated classification of wall motion abnormalities in echocardiograms," *Academic Radiology*, vol. 12, no. 3, pp. 358 – 367, 2005.

[8] G. Buckberg, "Left ventricular form and function: Scientific priorities and strategic planning for development of new views of disease," *Circulation*, vol. 110, pp. e333–e336, 2004.

[9] M. D. Cerqueira, N. J. Weissman, V. Dilsizian, A. K. Jacobs, S. Kaul, W. K. Laskey, D. J. Pennell, J. A. Rumberger, T. Ryan, and M. S. Verani, "Standardized myocardial segmentation and nomenclature for tomographic imaging of the heart," *Journal of the American Heart Association*, vol. 105, pp. 539–542, 2002.

[10] C. A. Cocosco, W. J. Niessen, T. Netsch, E. P. A. Vonken, G. Lund, A. Stork, and M. A. Viergever, "Automatic image-driven segmentation of the ventricles in cardiac cine MRI," *Journal of Magnetic Resonance Imaging: JMRI*, vol. 28, no. 2, pp. 366–374, 2008.

[11] L. D. Collins, A. P. Zijdenbos, W. F. C. Baare, and A. C. Evans, "ANIMAL+INSECT: Improved Cortical Structure Segmentation," *International Conference on Information Processing in Medical Imaging (IPMI)*, vol. 1, pp. 210–223, 1999.

[12] D. Comaniciu, V. Ramesh, and P. Meer, "Kernel-based object tracking," *IEEE Transactions on Pattern Analysis and Machine Intelligence*, vol. 25, no. 5, pp. 564–577, 2003.

[13] T. Cootes, G. Edwards, and C. Taylor, "Active appearance models," *Proceedings of the European Conference on Computer Vision*, vol. 2, pp. 484–498, 1998.

[14] T. F. Cootes, C. J. Taylor, D. H. Cooper, and J. Graham, "Active shape models, their training and application," *Computer Vision and Image Understanding*, vol. 61, no. 1, pp. 38–59, 1995.

[15] J. Cousty, L. Najman, M. Couprie, S. C. Guinaudeau, T. Goissen, and J. Garot, "Segmentation of 4D cardiac MRI: automated method based on spatio-temporal watershed cuts," *Image and Vision Computing*, vol. 28, no. 8, pp. 1229–1243, 2010.

[16] J. Garcia-Barnes, D. Gil, L. Badiella, A. Hernàndez-Sabaté, F. Carreras, S. Pujadas, and E. Martí, "A normalized framework for the design of feature spaces assessing the left ventricular function," *IEEE Transaction on Medical Imaging*, vol. 29, no. 3, pp. 733–745, 2010.

[17] R. van der Geest, E. Jansen, V. Buller, and J. Reiber, "Automated detection of left ventricular epi- and endocardial contours in short-axis MR images," *Computers in Cardiology*, vol. 1, pp. 33–36, 1994.

[18] A. Goshtasby and D. Turner, "Segmentation of cardiac cine MR images for extraction of right and left ventricular chambers," *IEEE Transactions on Medical Imaging*, vol. 14, no. 1, pp. 56 – 64, 1995.

[19] A. Gupta, L. von Kurowski, A. Singh, D. Geiger, C.-C. Liang, M.-Y. Chiu, L. Adler, M. Haacke, and D. Wilson, "Cardiac MR image segmentation using deformable models," *IEEE Conference on Computers in Cardiology*, vol. 1, pp. 747–750, 1993.

[20] H. C. Han, R. P. Martin, G. Lerakis, and S. Lerakis, "Prediction of the left ventricular ejection fraction improvement using echocardiography and mechanical modeling," *Journal of the American Society of Echocardiography*, vol. 18, no. 7, pp. 718–721, 2005.

[21] R. Hoffmann, S. von Bardeleben, J. D. Kasprzak, A. C. Borges, F. ten Cate, C. Firschke, S. Lafitte, N. Al-Saadi, S. Kuntz-Hehner, G. Horstick, C. Greis, M. Engelhardt, J. L.

Vanoverschelde, and H. Becher, "Analysis of regional left ventricular function by cin-eventriculography, cardiac magnetic resonance imaging, and unenhanced and contrast-enhanced echocardiography: A multicenter comparison of methods," *Journal of Amercican College of Cardiology*, vol. 47, no. 1, pp. 121–128, 2006.

[22] N. P. Hughes, L. Tarassenko, and S. J. Roberts, "Markov models for automated ECG interval analysis," in *Advances in Neural Information Processing System*, vol. 16, 2004, pp. 611–618.

[23] M. Jolly, "Fully automatic left ventricle segmentation in cardiac cine MR images using registration and minimum surfaces," *MICCAI Workshop on Cardiac MR Left Ventricle Segmentation Challenge*, vol. 1, pp. 1–8, 2009.

[24] M. P. Jolly, "Automatic segmentation of the left ventricle in cardiac MR and CT images," *International Journal of Computer Vision*, vol. 70, no. 2, pp. 151–163, 2006.

[25] T. D. Karamitsos, J. M. Francis, S. Myerson, J. B. Selvanayagam, and S. Neubauer, "The role of cardiovascular magnetic resonance imaging in heart failure," *Journal of the American College of Cardiology*, vol. 54, no. 15, pp. 1407–1424, 2009.

[26] T. D. Karamitsos, L. E. Hudsmith, J. B. Selvanayagam, S. Neubauer, and J. M. Francis, "Operator induced variability in left ventricular measurements with cardiovascular magnetic resonance is improved after training," *Journal of Cardiovascular Magnetic Resonance*, vol. 9, pp. 777–783, 2007.

[27] M. Kass, A. Witkin, and D. Terzopoulos, "Snakes: Active contour models," *International Journal of Computer Vision*, vol. 1, no. 4, pp. 321–331, 1988.

[28] A. Katouzian, A. Prakash, and E. Konofagou, "A new automated technique for left- and right-ventricular segmentation in magnetic resonance imaging," *Engineering in Medicine and Biology Society*, vol. 1, pp. 3074–3077, 2006.

[29] S. Kaushikkar, D. Li, E. Haale, and V. Davila-Roman, "Adaptive blood pool segmentation in three-dimensions: application to MR cardiac evaluation." *Journal of magnetic resonance imaging : JMRI*, vol. 6, no. 4, pp. 690–697, 1996.

[30] P. J. Kilner, P. D. Gatehouse, and D. N. Firmin, "Flow measurement by magnetic resonance: a unique asset worth optimising," *Journal of Cardiovascular Magnetic Resonance*, vol. 9, pp. 723–728, 2007.

[31] T. Kuznetsova, L. Herbots, Y. Jin, K. Stolarz-Skrzypek, and J. A. Staessen, "Systolic and diastolic left ventricular dysfunction: from risk factors to overt heart failure," *Expert Review of Cardiovascular Theroapy*, vol. 8, no. 2, pp. 251–258, 2010.

[32] A. Lalande, L. Legrand, P. Walker, F. Guy, Y. Cottin, S. Roy, and F. Brunotte, "Automatic detection of left ventricular contours from cardiac cine magnetic resonance imaging using fuzzy logic," *Investigacion Radiology*, vol. 34, no. 3, pp. 211–217, 1999.

[33] K. Lekadir, N. Keenan, D. Pennell, and G. Yang, "An inter-landmark approach to 4-D shape extraction and interpretation: Application to myocardial motion assessment in MRI," *IEEE Transactions on Medical Imaging*, vol. 30, no. 1, pp. 52 –68, 2011.

[34] K. Y. Leung and J. G. Bosch, "Localized shape variations for classifying wall motion in echocardiograms," in *Medical Image Computing and Computer-Assisted Intervention; MICCAI*, vol. 4791, 2007, pp. 52–59.

[35] X. Lin, B. Cowan, and A. Young, "Automated detection of left ventricle in 4d MR images: Experience from a large study," in *Medical Image Computing and Computer-Assisted Intervention; MICCAI*, vol. 4190, 2006, pp. 728–735.

[36] X. e. Lin, "Model based graph cut method for segmentation of the left ventricle," *Engineering in Medicine and Biology Society*, vol. 3, pp. 3059–3062, 2006.

[37] M. Lorenzo-Valdés, G. I. Sanchez-Ortiz, A. G. Elkington, R. H. Mohiaddin, and D. Rueckert, "Segmentation of 4D cardiac MR images using a probabilistic atlas and the EM algorithm," *Medical Image Analysis*, vol. 8, no. 3, pp. 255–265, 2004.

[38] Y. Lu, P. Radau, K. Connelly, A. Dick, and G. Wright, "Pattern recognition of abnormal left ventricle wall motion in cardiac MR," in *Medical Image Computing and Computer-Assisted Intervention; MICCAI*, vol. 5762, 2009, pp. 750–758.

[39] M. Lynch and et al., "Automatic segmentation of the left ventricle cavity and myocardium in MRI data," *Computers in Biology and Medicine*, vol. 36, pp. 389–407, 2006.

[40] M. Lynch, O. Ghita, and P. Whelan, "Left ventricle myocardium segmentation using a coupled level-set with a priori knowledge," *Computerized Medical Imaging and Graphics*, vol. 30, pp. 255–262, 2006.

[41] M. Lynch, O. Ghita, and P. F. Whelan, "Segmentation of the left ventricle of the heart in 3-D+t MRI data using an optimized nonrigid temporal model," *IEEE Transactions on Medical Imaging*, vol. 27, no. 2, pp. 195–203, 2008.

[42] H. Mahrholdt, A. Wagner, T. A. Holly, M. D. Elliott, R. O. Bonow, R. J. Kim, and R. M. Judd, "Reproducibility of chronic infarct size measurement by contrast-enhanced magnetic resonance imaging," *Circulation*, vol. 106, pp. 2322–2327, 2002.

[43] S. Mansor and J. Noble, "Local wall motion classification of stress echocardiography using a hidden Markov model approach," *International Symposium on Biomedical Imaging (ISBI) : From Nano to Macro*, vol. 1, pp. 1295–1298, 2008.

[44] O. Michailovich, R. Yogesh, and A. Tannenbaum, "Image segmentation using active contours driven by the bhattacharyya gradient flow," *IEEE Transaction on Image Processing*, vol. 16, no. 11, pp. 2787–2801, 2007.

[45] E. Nachtomy, R. Cooperstein, M. Vaturi, E. Bosak, Z. Vered, and S. Akselrod, "Automatic assessment of cardiac function from short-axis MRI: procedure and clinical evaluation," *Magnetic Resonance Imaging*, vol. 16, no. 4, pp. 365 – 376, 1998.

[46] T. O'Donnell, G. Funka-Lea, H. Tek, M.-P. Jolly, M. Rasch, and R. Setser, "Comprehensive cardiovascular image analysis using MR and CT at siemens corporate research," *International Journal of Computer Vision*, vol. 70, no. 2, pp. 165–178, 2006.

[47] N. Paragios, "A level set approach for shape-driven segmentation and tracking of the left ventricle," *IEEE Transactions on Medical Imaging*, vol. 22, no. 6, pp. 773–776, Jun 2003.

[48] A. Pednekar, U. Kurkure, R. Muthupillai, S. Flamm, and I. A. Kakadiaris, "Automated left ventricular segmentation in cardiac MRI," *IEEE Transactions on Bio-Medical Engineering*, vol. 53, no. 7, pp. 1425–1428, 2006.

[49] C. Petitjean and J.-N. Dacher, "A review of segmentation methods in short axis cardiac MR images," *Medical Image Analysis*, vol. 15, no. 2, pp. 169–184, 2011.

[50] K. Punithakumar, I. Ben Ayed, A. Islam, I. Ross, and S. Li, "Regional heart motion abnormality detection via information measures and unscented kalman filtering," in *Medical Image Computing and Computer-Assisted Intervention; MICCAI*, vol. 6361, 2010, pp. 409–417.

[51] K. Punithakumar, S. Li, I. B. Ayed, I. Ross, A. Islam, and J. Chong, "Heart motion abnormality detection via an information measure and Bayesian filtering," in *Medical Image Computing and Computer-Assisted Intervention; MICCAI*, vol. 5762, 2009, pp. 373–380.

[52] Z. Qian, Q. Liu, D. N. Metaxas, and L. Axel, "Identifying regional cardiac abnormalities from myocardial strains using spatio-temporal tensor analysis," in *MICCAI2008*, vol. 5241, 2008, pp. 789–797.

[53] A. B. Redheuil, N. Kachenoura, R. Laporte, A. Azarine, X. Lyon, O. Jolivet, F. Frouin, and E. Mousseaux, "Interobserver variability in assessing segmental function can be reduced by combining visual analysis of CMR cine sequences with corresponding parametric images of myocardial contraction," *Journal of Cardiovascular Magnetic Resonance*, vol. 9, no. 6, pp. 863–872, 2007.

[54] V. L. Roger and et.al, "Heart disease and stroke statistics," *American Heart Association*, vol. 125, pp. e2–e220, 2012.

[55] A. Sarwar, M. D. Shapiro, S. Abbara, and R. C. Cury, "Cardiac magnetic resonance imaging for the evaluation of ventricular function," *Seminars in Roentgenology*, vol. 43, pp. 183–192, 2008.

[56] J. Selvanayagam, S. Westaby, K. Channon, J. Francis, J. Eichhfer, S. Saito, and S. Neubauer, "Images in cardiovascular medicine. surgical left ventricular restoration: an extreme case." *Circulation*, vol. 107, p. e71, 2003.

[57] F. G. Shellock and J. V. Crues, "MR procedures: biologic effects, safety, and patient care," *Radiology*, vol. 232, pp. 635–652, 2004.

[58] A. Suinesiaputra, A. Frangi, T. Kaandorp, H. Lamb, J. Bax, J. Reiber, and B. Lelieveldt, "Automated detection of regional wall motion abnormalities based on a statistical model applied to multislice short-axis cardiac MR images," *IEEE Transactions on Medical Imaging*, vol. 28, no. 4, pp. 595–607, 2009.

[59] A. Suinesiaputra, A. F. Frangi, T. A. Kaandorp, H. J. Lamb, J. J. Bax, J. H. Reiber, and B. P. Lelieveldt, "Automated regional wall motion abnormality detection by combining rest and stress cardiac MRI: Correlation with contrast-enhanced MRI," *Journal of Magnetic Resonance Imaging*, vol. 34, no. 2, pp. 270–278, 2011.

[60] H. Sundar, C. Davatzikos, and G. Biros, "Biomechanically-constrained 4D estimation of myocardial motion," in *Medical Image Computing and Computer-Assisted Intervention; MICCAI*, vol. 5762, 2009, pp. 257–265.

[61] T. F. Walsh and W. G. Hundley, "Assessment of ventricular function with cardiovascular magnetic resonance," *Magnetic Resonance Imaging Clinics of North America*, vol. 15, no. 4, pp. 487 – 504, 2007.

[62] J. J. Weng, A. Singh, and M. Y. Chiu, "Learning-based ventricle detection from cardiac MR and CT images," *IEEE Transaction on medical imaging*, vol. 16, no. 4, pp. 378–391, 1997.

[63] P. Yan, A. Sinusas, and J. S. Duncan, "Boundary element method-based regularization for recovering of LV deformation," *Medical Image Analysis*, vol. 11, no. 6, pp. 540–554, 2007.

[64] J. Yeh, J. Fu, C. Wu, H. Lin, and J. Chai, "Myocardial border detection by branch-and-bound dynamic programming in magnetic resonance images," *Computer Methods and Programs in Biomedicine*, vol. 79, no. 1, pp. 19–29, 2005.

[65] S. Zambal, J. Hladuvka, and K. Bhler, "Improving segmentation of the left ventricle using a two-component statistical model," in *Medical Image Computing and Computer-Assisted Intervention; MICCAI*, vol. 9, 2006, pp. 151–158.

[66] H. Zhang, A. Wahle, R. K. Johnson, T. D. Scholz, and M. Sonka, "4-D cardiac MR image analysis: left and right ventricular morphology and function," *IEEE Transactions on Medical Imaging*, vol. 29, no. 2, pp. 350–364, 2010.

[67] X. Zhuang, D. J. Hawkes, W. R. Crum, R. Boubertakh, S. Uribe, D. Atkinson, P. Batchelor, T. Schaeffter, R. Razavi, and D. L. G. Hill, "Robust registration between cardiac MRI images and atlas for segmentation propagation," in *Proceedings of SPIE*, 2008.

[68] X. Zhuang, K. S. Rhode, S. R. Arridge, R. Razavi, D. L. G. Hill, D. J. Hawkes, and S. Ourselin, "An atlas-based segmentation propagation framework using locally affine registration - application to automatic whole heart segmentation," in *Medical Image Computing and Computer-Assisted Intervention; MICCAI*, vol. 11, 2008, pp. 425–433.

Chapter 2

Global Assessment of Cardiac Left Ventricle Function Using Estimation of Ejection Fraction

2.1 Estimation of the Cardiac Ejection Fraction From Magnetic Resonance Image Statistics

The cardiac ejection fraction (EF) depends on the volume variation of the left ventricle (LV) cavity during a cardiac cycle, and is an essential measure in the diagnosis of cardiovascular diseases .

In routine clinical use, EF is often estimated from the manual segmentation of several images in a cardiac sequence, which is a time consuming procedure. As discussed in section. 1.5,

---

[1]This chapter is based on three papers:
1) Afshin, M., Ben Ayed, I., Punithakumar, P., Islam, A., Goela, A., Ross, I., Peters, T., Li, S., "Global Assessment of Cardiac Function using Image Statistics in MRI", Medical Image Computing and Computer Assisted Interventions (MICCAI 2012), Vol 7511, pp. 535-545 (2012).
2) Afshin, M., Ben Ayed, I., Islam, A., Goela, A., Ross, I., Peters, T., Li, S, "Estimation Of The Ejection Fraction From Image Statistics", IEEE International Symposium on Biomedical Imaging (ISBI), pp. 824-827 (2012).
3) Afshin, M., Ben Ayed, I., Islam, A., Goela, A., Ross, I., Peters, T., Li, Sh., " Estimation of the Cardiac Ejection Fraction From Magnetic Resonance Image Statistics", under second revision in IEEE Transaction on Biomedical Engineering.

in recent years automatic LV segmentation techniques are used to compute the EF. Existing LV segmentation algorithms are based on traditional techniques, such as thresholding, region-growing, edge detection and clustering [7, 10, 8], and energy minimization techniques such as graph cuts [2, 13], active contours/level-sets [6, 3], as well as active appearance and shape models [1]. A recent comprehensive review of cardiac image segmentation can be found in [13]. Segmentation algorithms generally require a careful user initialization, intensive training, and a heavy computational load. The segmentation results depend significantly on the choice of a set of *ad hoc* parameters and training data, which may yield high errors in the computation of the EF. These difficulties inherent to segmentation algorithms prevent the automatic segmentation methods from being used in routine clinical practice. As most of the existing techniques require intensive user interaction, we believe that there are other image characteristics that are computationally less expensive but correlate strongly with the EF.

In this chapter, we propose a technique to estimate the EF directly from image statistics via machine learning in MRI. From a simple user input in one single image, we build a statistic based on the Bhattacharyya coefficient [14] of similarity between image distributions for all the images in a subject dataset (200 images). We demonstrate that these statistics are non-linearly but monotonically related to the LV cavity areas and, therefore, can be used to estimate the EF via an Artificial Neural Network (ANN) directly. A comprehensive evaluation over 20 subjects demonstrates that the estimated EFs correlated very well with those obtained from independent manual segmentations. Furthermore, comparisons with estimating EF with recent segmentation algorithms show that the proposed method can yield a very competitive performance.

2.2 Estimating Left Ventricle Volumes from Image Statistics

2.2.1 Building Image Statistics

Let $\mathcal{I}$ be a cardiac MRI sequence containing J frames[1], each comprising I slices[2], $\mathcal{I}_{i,j}$: $\Omega \subset \mathfrak{R}^2 \to \mathfrak{R}^+$ with $(i,j) \in [1\ldots I] \times [1\ldots J]$. To introduce how we build an image statistic related to the LV cavity area for each image $\mathcal{I}_{i,j}$, $(i,j) \in [1\ldots I] \times [1\ldots J]$, let us consider the following definitions.

- Let **I** be a reference image which we use for a simple user input (refer to the middle image in Fig. 2.1 b). For instance, in the experiments of this study, we used image $\mathcal{I}_{7,1}$ in each subject dataset.

- Let $\Gamma_{in}, \Gamma_{out} : [0,1] \to \Omega$ denote two simple planar closed curves (e.g. squares) superimposed by the user on the reference image **I** (refer to the middle image in Fig. 2.1 b), one placed within the cavity (the blue curve in Fig. 2.1 b) and the other enclosing the cavity (the red curve) which are identical for each patient.

Let us now superimpose systematically (without additional user effort) Γ_{out} onto each of the images in the subject dataset, as shown in Fig. 2.1, Fig. 2.2 and Fig. 2.3. Then, we compute for each image a statistic based on the Bhattacharyya coefficient of similarity between image distributions (refer to Fig. 2.5, Fig. 2.4, and Fig. 2.6), and demonstrate that *the obtained statistics are related to the areas of the LV*.

Let $\mathbf{R}_\Gamma \subset \Omega$ be the region enclosed within Γ, $\Gamma \in \{\Gamma_{in}, \Gamma_{out}\}$, and $P_{\mathbf{R}_\Gamma, I}$ the kernel density estimate of the distribution of an image $I \in \mathcal{I}_{i,j}$, $(i,j) \in [1\ldots I] \times [1\ldots J]$, within region $\mathbf{R}_\Gamma$:

$$P_{\mathbf{R}_\Gamma, I}(z) = \frac{\int_{\mathbf{R}_\Gamma} K(z-I)dx}{a_{\mathbf{R}_\Gamma}} \tag{2.1}$$

---

[1]The number of frames J is typically equal to 20 or 25.
[2]The number of slices I is typically equal to 10.

(a)   (b)
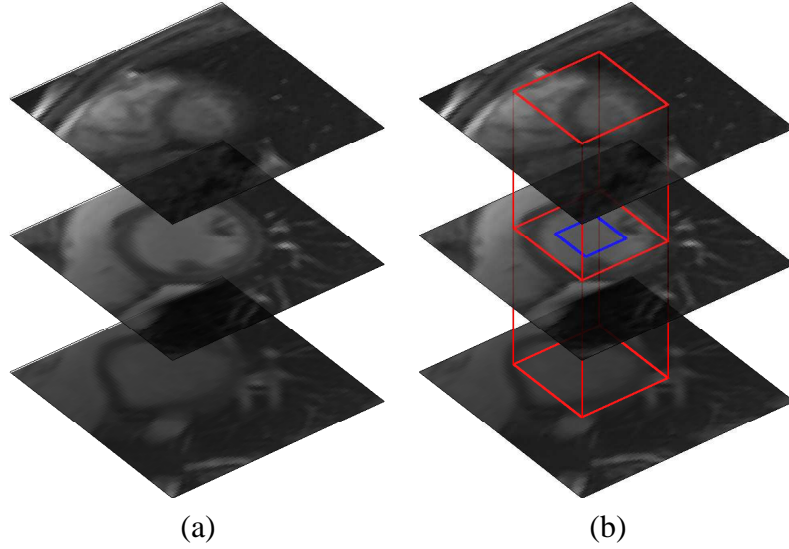
Figure 2.1: User input: (a) frame 1 (slices 1,7, and 10); (b) Γ_{in} (the blue curve within the cavity) and Γ_{out} (the red curve enclosing the cavity) are given by the user in the reference image (the middle image). Γ_{in} is used solely in the reference image to compute $P_{\mathbf{R}_{\Gamma_{in}},\mathbf{I}}$, whereas Γ_{out} is superimposed systematically (without additional user effort) to all the other images (refer to Figs. 2.2 and 2.3) to compute $P_{\mathbf{R}_{\Gamma_{out}},\mathcal{I}_{i,j}}$.

(a)   (b)
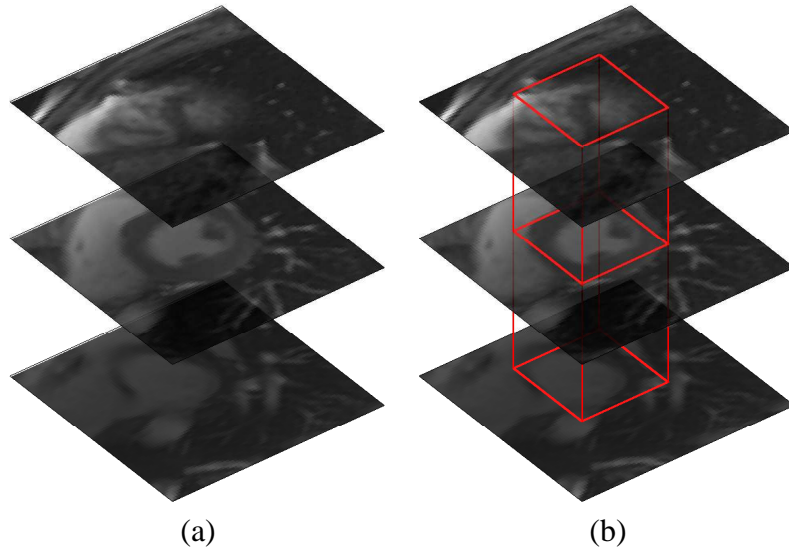
Figure 2.2: Superimposing red curve in End-systole: frame 7 (slices 1,7, and 10): Γ_{out} is superimposed systematically (without additional user effort) to all the slices in the 7th frame.

Where $a_{\mathbf{R}_{\Gamma}}$ is the area inside region $\mathbf{R}_{\Gamma}$

$$a_{\mathbf{R}_{\Gamma}} = \int_{\mathbf{R}_{\Gamma}} dx \qquad (2.2)$$

40
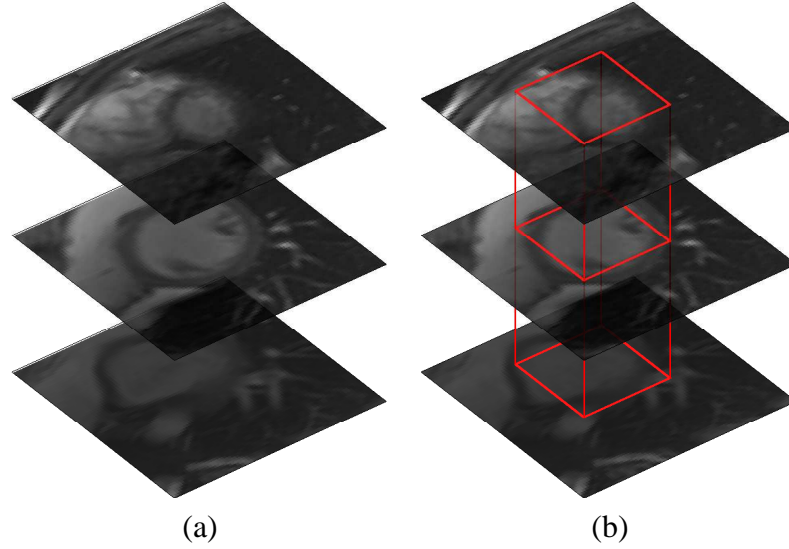
Figure 2.3: Superimposing red curve in End-diastole: frame 20 (slices 1,7, and 10): Γ_{out} is superimposed systematically (without additional user effort) to all the slices in the 20th frame.

K is the Gaussian kernel [14]:

$$K(y) = \frac{1}{\sqrt{2\pi\sigma^2}} exp^{-\frac{y^2}{2\sigma^2}} \tag{2.3}$$

We consider the distribution of the image within the region enclosed by the blue curve in the reference image ($P_{\mathbf{R}_{\Gamma_{in}},\mathbf{I}}$) as an approximation of the distribution within the cavity, and the distribution of the region enclosed by the red curve in each image $\mathcal{I}_{i,j}$ ($P_{\mathbf{R}_{\Gamma_{out}},\mathcal{I}_{i,j}}$) as an approximation of the distribution of the entire left ventricle. Now consider the following measure of similarity between these two distributions in each image $\mathcal{I}_{i,j}$, $(i,j) \in [1\ldots I] \times [1\ldots J]$:

$$\beta^{i,j} = \mathbf{B}(P_{\mathbf{R}_{\Gamma_{in}},\mathbf{I}}, P_{\mathbf{R}_{\Gamma_{out}},\mathcal{I}_{i,j}}), \tag{2.4}$$

where the Bhattacharyya coefficient $\mathbf{B}(f,g)$ measures the amount of overlap (similarity) between two distributions f and g:

$$\mathbf{B}(f,g) = \int_{\Re^+} \sqrt{fg}\, dz \tag{2.5}$$

There are different choices for estimating the similarity measurement between two distributions e.g.Bhattacharyya coefficient, Kullback-Leibler, Hellinger distance and Mahalanobis distance. Among others, Bhattacharyya coefficient has been chosen as the range of the Bhattacharyya coefficient is [0; 1], with 0 indicating no overlap between the distributions and 1 being perfect match. The fixed [0; 1] range of the Bhattacharyya coefficient affords a conveniently practical appraisal of the similarity.

More importantly, we expect that measure $\beta^{i,j}$ is related to the cavity area in the corresponding image $\mathcal{I}_{i,j}$. This is demonstrated experimentally by the typical example in Figs. 2.4-2.6, the corresponding variations of the cavity areas in Figs. 2.7, 2.9, 2.11, and the Bhattacharyya statistics in Figs. 2.8, 2.10, 2.12. *Note the strong similarity between the variations of the cavity areas (Figs. 2.7, 2.9, 2.11) and those of the Bhattacharyya statistics (Figs. 2.8, 2.10, 2.12).* Such similarity is reasonable since the more the distributions of the cavity and the LV overlap, the higher the cavity area.
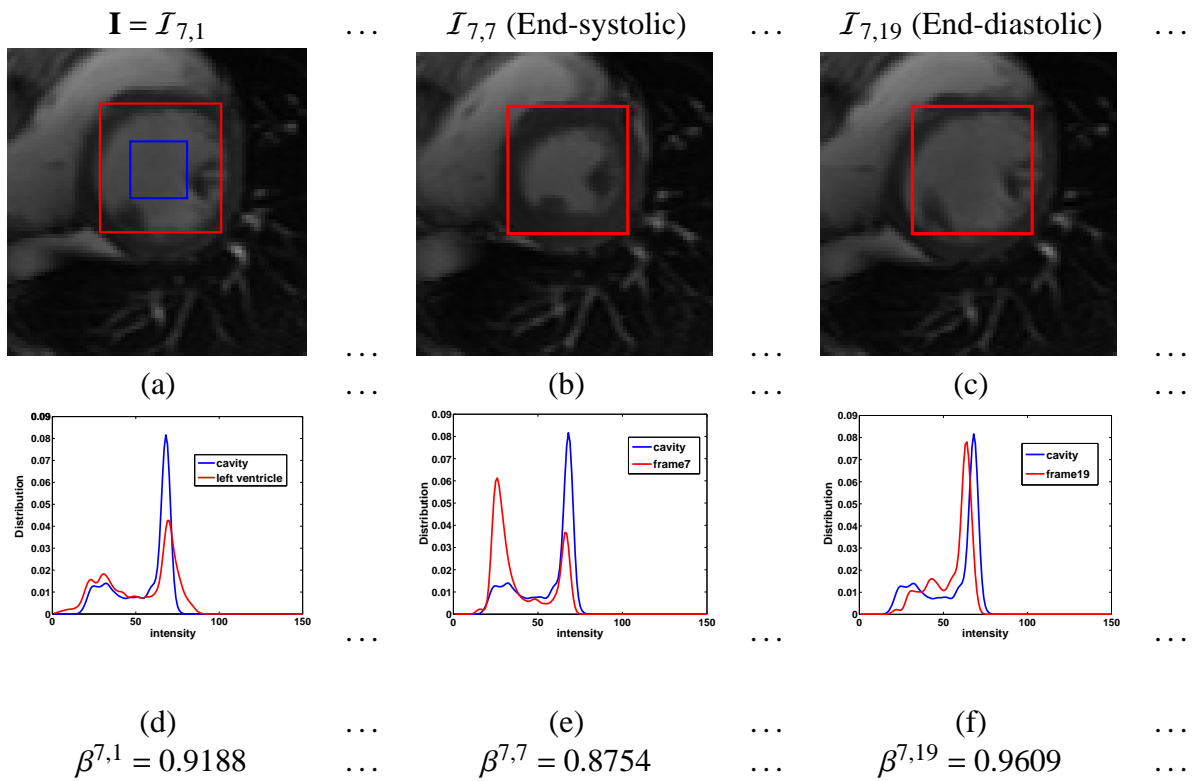
Figure 2.4: Computing image statistics for the frames of slice 7 (middle slice): (a) reference image (red curve: Γ_{out}, blue curve: Γ_{in}); (b): frame 7 (end-systolic) and (c) frame 19 (end-diastolic); (d), (e), and (f) the corresponding intensity distributions and Bhattacharyya measures (β^{ij}). *We observe that the variations of β^{ij} are similar to the variations of the LV cavity areas. For instance at the end of systole (the middle column), the smallest cavity area coincides with the lowest Bhattacharyya measure.*

$\mathcal{I}_{1,1}$ ... $\mathcal{I}_{1,7}$ ... $\mathcal{I}_{1,19}$

(a) ... (b) ... (c)

(d) ... (e) ... (f)

$\beta^{1,1} = 0.8443$ ... $\beta^{1,7} = 0.7998$ ... $\beta^{1,19} = 0.8100$
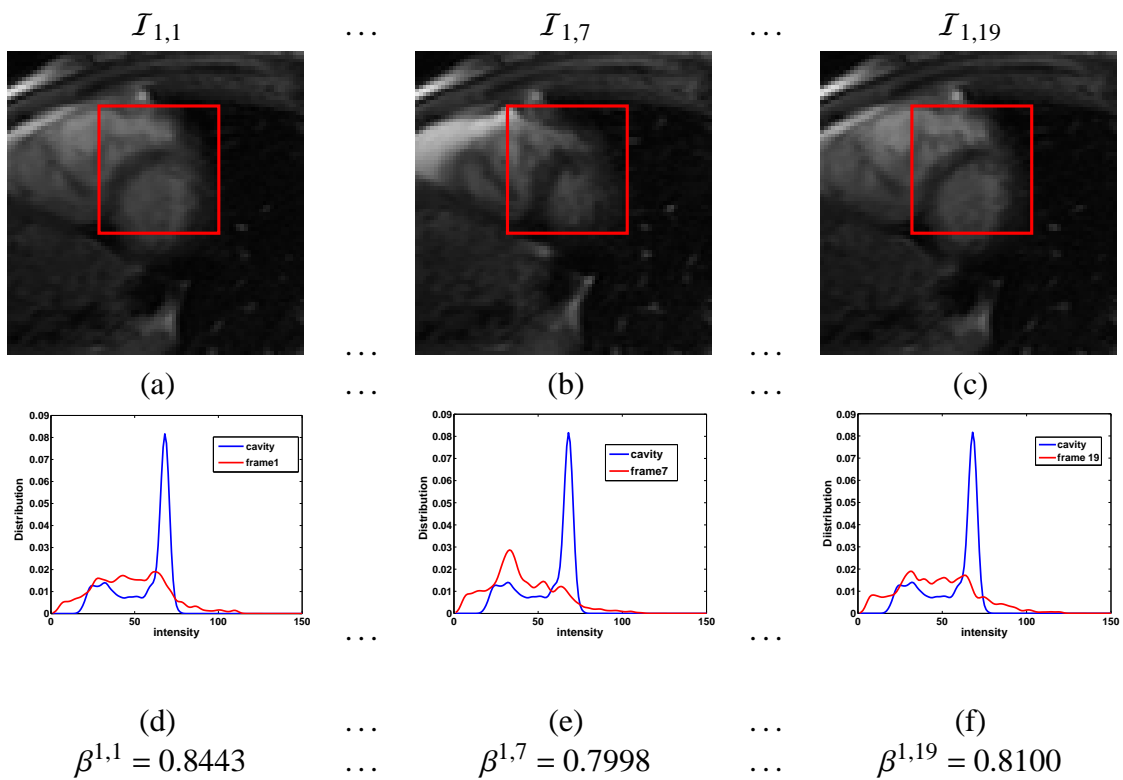
Figure 2.5: Computing image statistics for the frames of slice 1 (apical slice): (a) frame 1 (the red curve, Γ_{out}, is superimposed systematically to all the images without additional user effort); (b): frame 7 and (c) frame 19; (d), (e), and (f) the corresponding intensity distributions and Bhattacharyya measures (β^{ij}). *Again, we observe that the variations of β^{ij} are similar to the variations of the LV cavity areas.*

$\mathcal{I}_{10,1}$ ... $\mathcal{I}_{10,7}$ ... $\mathcal{I}_{10,19}$

(a)   ...   (b)   ...   (c)

(d)   ...   (e)   ...   (f)

$\beta^{10,1} = 0.4339$ ... $\beta^{10,7} = 0.4588$ ... $\beta^{10,19} = 0.4168$
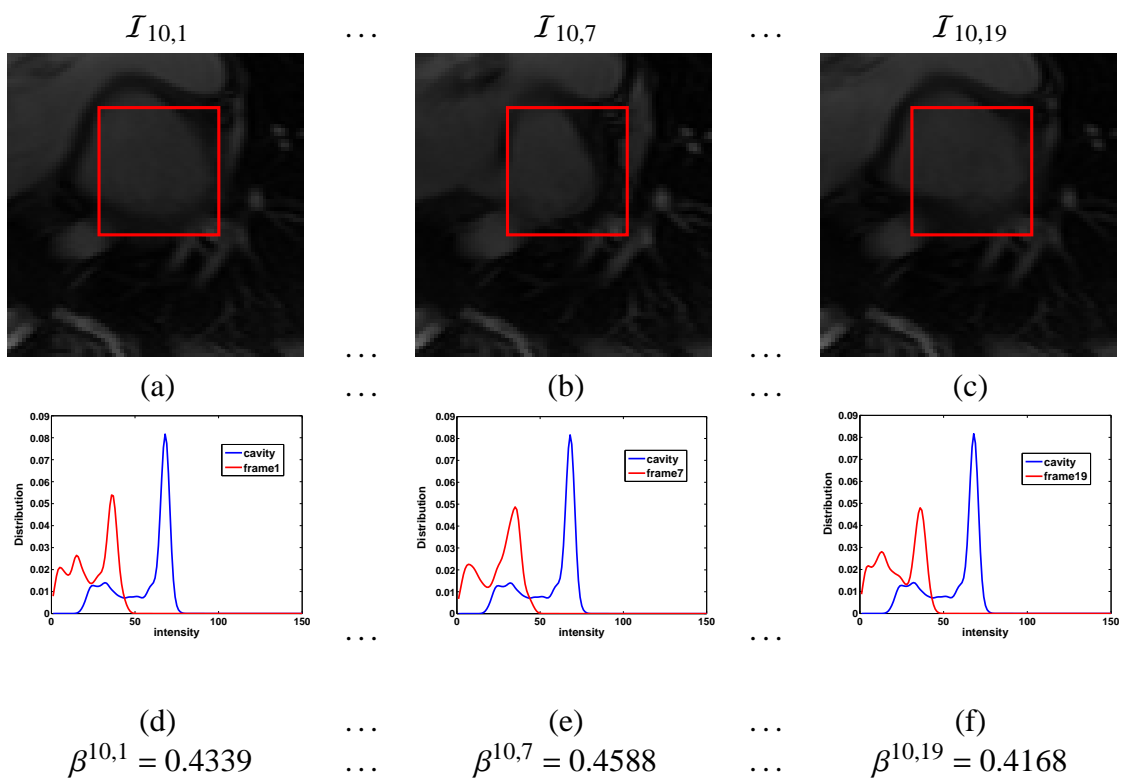
Figure 2.6: Computing image statistics for all the images of slice 10 (basal slice): (a) frame 1; (b) frame 7 and (c) frame 19; (d), (e), and (f) the corresponding intensity distributions and Bhattacharyya measures (β^{ij}).

2.2.2 Training Phase: A Statistical Bhattacharyya Coefficient Model

To compute the area inside the LV cavity for each single 2D image in the cardiac MR sequence, we map each image $\mathcal{I}_{i,j}$ to a Bhattacharyya statistic $\beta^{i,j}$. Let $\mathbf{P}_m$ be a 200-dimensional row matrix containing the Bhattacharyya statistics for a training subject $m \in M$ (M is the number of training subjects):

$$
\begin{aligned}
\mathbf{P}_m &= [\mathbf{P}_m{}^1, ..., \mathbf{P}_m{}^j, ..., \mathbf{P}_m{}^{10}] \quad with \\
\mathbf{P}_m{}^j &= \left[\begin{array}{ccccc} \beta^{1,j} & ... & \beta^{i,j} & ... & \beta^{20,j} \end{array} \right] \\
m &\in \{1, ..., M\}.
\end{aligned}
\tag{2.6}
$$

Thus, the Bhattacharyya statistics from M training subjects can be viewed as a cloud of M points in a 200-dimensional space. Following a principal component PCA analysis [4], one can assume that these points lie within a lower-dimensional space. This amounts to mapping each $\mathbf{P}_m, m = 1 \ldots M$, to a lower-dimensional point $\mathbf{r}_m$ as follows:

$$
\mathbf{P}_m = \mathbf{P}_{mean} + \mathbf{Q}\mathbf{r}_m = \mathbf{P}_{mean} + \sum_{i=1}^{t} r_m^i Q_i,
\tag{2.7}
$$

where $\mathbf{P}_{mean}$, $\mathbf{Q} = (Q_1 \ Q_2 \ ...Q_t)$, $\mathbf{r}_m = (r_m^1 \ r_m^2, ..., r_m^t)^T$ and t are defined as follows:

- $\mathbf{P}_{mean}$ is the mean of Bhattacharyya row matrices:

$$
\mathbf{P}_{mean} = \frac{1}{M} \sum_{m=1}^{M} \mathbf{P}_m
\tag{2.8}
$$

- $\mathbf{Q} = (Q_1 \ Q_2 \ ...Q_t)$ is the matrix of the first t unit eigenvectors of the following 200×200 covariance matrix $\mathbf{S_P}$ (how to fix t will be discussed later):

$$
\mathbf{S_P} = \frac{1}{M} \sum_{m=1}^{M} d\mathbf{P}_m \ d\mathbf{P}_m{}^T,
\tag{2.9}
$$

46

where $d\mathbf{P}_m = \mathbf{P}_m - \mathbf{P}_{mean}$ is a vector measuring the deviation of each patient's Bhattacharyya matrix from the mean.

- Vector $\mathbf{r}_m = (r_m^1\, r_m^2, ..., r_m^t)^T$ contains scalars weighting the contribution of each of the t eigenvectors in (2.7). $\mathbf{r}_m$ is obtained by the closed-form solution of the following least-square-error minimization:

$$\mathbf{r}_m = \underset{\mathbf{r}}{\operatorname{argmin}} \|\mathbf{Q}\mathbf{r} - (\mathbf{P}_m - \mathbf{P}_{mean})\|^2 \tag{2.10}$$

This yields:

$$\mathbf{r}_m = \mathbf{Q}^+(\mathbf{P}_m - \mathbf{P}_{mean}) \tag{2.11}$$

where $\mathbf{Q}^+$ is the pseudo inverse matrix of $\mathbf{Q}$.

- *How to choose t*: The eigenvectors of $\mathbf{S_P}$ are the orthogonal components that span the 200-dimensional training space and their corresponding eigenvalues $\lambda_i, i = 1 \ldots 200$, measure how significant these components are. The larger the eigenvalue, the more significant the corresponding eigenvector. To obtain the t most significant eigenvectors, we need to find a $t < 200$. A common method for calculating t is to choose the smallest number of eigenvectors, so that the ratio of the sum of the corresponding t eigenvalues to the sum of all eigenvalues,

$$\frac{\sum_{i=1}^{t} \lambda_i}{\sum_{i=1}^{200} \lambda_i}, \tag{2.12}$$

is sufficiently close to one [4]. This means that the sum of the variances along the t most significant eigenvectors corresponds to a sufficiently large proportion of the total variance of all the data. In this study, we obtain t by satisfying the following condition:

$$\frac{\sum_{i=1}^{t} \lambda_i}{\sum_{i=1}^{200} \lambda_i} \geq 0.95. \tag{2.13}$$

The choice of t and its effect on the results will be further discussed in the experiments.

2.2.3 Training Phase: Statistical Area Model

Now assume the LV cavity areas in each cardiac MR sequence of the training set are computed using manual segmentation obtained by an expert. Let us express the areas of each training subject as a point in a 200-dimensional space:

$$
\begin{aligned}
\mathbf{T}_m &= [\mathbf{T}_m{}^1, ..., \mathbf{T}_m{}^j, ..., \mathbf{T}_m{}^{10}] \quad with \\
\mathbf{T}_m{}^j &= \left[\begin{array}{ccccc} a^{1,j} & ... & a^{i,j} & ... & a^{20,j} \end{array} \right] \\
m &\in \{1, ..., M\}.
\end{aligned} \tag{2.14}
$$

Following a PCA analysis similar to that used for the Bhattacharyya statistics, we map each point $\mathbf{T}_m, m = 1 \dots M$, to a lower-dimensional point $\mathbf{b}_m$ as follows:

$$
\mathbf{T}_m = \mathbf{T}_{mean} + \mathbf{C}\mathbf{b}_m, \tag{2.15}
$$

where $\mathbf{T}_{mean}$ is the mean of area row matrices:

$$
\mathbf{T}_{mean} = \frac{1}{M} \sum_{m=1}^{M} \mathbf{T}_m, \tag{2.16}
$$

$\mathbf{C} = (C_1 \; C_2 \; ...C_t)$ is the matrix of the first t unit eigenvectors C_i of the following 200×200 covariance matrix (the value of t is similar to the one obtained for the Bhattacharyya statistics):

$$
\mathbf{S_T} = \frac{1}{M} \sum_{m=1}^{M} d\mathbf{T}_m \; d\mathbf{T}_m{}^T, \tag{2.17}
$$

with $d\mathbf{T}_m = \mathbf{T}_m - \mathbf{T}_{mean}$ is a vector measuring the deviation of each matrix of areas from the mean, and $\mathbf{b}_m = (b_m^1 \; b_m^2, ..., b_m^t)^T$ a weighting vector given by:

$$
\mathbf{b}_m = \mathbf{C}^+(\mathbf{T}_m - \mathbf{T}_{mean}), \tag{2.18}
$$

with $\mathbf{C}^+$ denoting the pseudo inverse of $\mathbf{C}$.

2.2.4   Procedure

The proposed technique involves two stages, one corresponding to training and the other to testing. The principle steps of each stage are as follows:

Training Stage:

This stage consists of the following steps.

- Following a PCA analysis over the Bhattacharyya statistics from M training subjects, we compute $\mathbf{r}_m$ according to equation (2.11) for each training subject $m \in [1 \ldots M]$.

- Using manual segmentations of the M training subjects and following a PCA analysis of the ensuing LV cavity areas, we compute $\mathbf{b}_m$ according to equation (2.18) for each subject $m \in [1 \ldots M]$.

- Using an Artificial Neural Network (ANN) [12] and vectors $\mathbf{r}_m$ and $\mathbf{b}_m$ ($m \in [1 \ldots M]$) as training data for the ANN, we learn a non-linear relationship between the Bhattacharyya statistics and the LV cavity areas. This amounts to finding a fitting function $\mathbf{F}$ that verifies:

$$\mathbf{b}_m = \mathbf{F}(\mathbf{r}_m) \quad \forall m \in [1 \ldots M] \tag{2.19}$$

Further details on the estimation of the fitting function will be given in the next section.

Testing Stage:

The purpose of this stage is to estimate the LV cavity area for a new testing subject not included in the training set. This stage consists of the following steps.

- Let $\mathbf{P}_{new}$ a single row matrix containing the Bhattacharyya statistics for the new subject:

$$
\begin{aligned}
\mathbf{P}_{new} &= [\mathbf{P}_{new}{}^{1}, ..., \mathbf{P}_{new}{}^{j}, ..., \mathbf{P}_{new}{}^{10}] \quad \textit{with} \\
\mathbf{P}_{new}{}^{j} &= \left[\begin{array}{ccccc} \beta_{new}^{1,j} & \ldots & \beta_{new}^{i,j} & \ldots & \beta_{new}^{20,j} \end{array} \right]
\end{aligned} \tag{2.20}
$$

with $\beta_{new}^{i,j}$ denoting the Bhattacharyya statistic corresponding to image $\mathcal{I}_{i,j}$ of the new subject. From $\mathbf{P}_{new}$, we compute the following vector:

$$\mathbf{r}_{new} = \mathbf{Q}^+(\mathbf{P}_{new} - \mathbf{P}_{mean}) \tag{2.21}$$

- From $\mathbf{r}_{new}$, we infer the following vector using fitting function $\mathbf{F}$ (further details on estimating $\mathbf{F}$ will be described in section 2.2.5):

$$\mathbf{b}_{new} = \mathbf{F}(\mathbf{r}_{new}) \tag{2.22}$$

- Finally, the matrix of estimated LV cavity areas for the new subject is obtained from $\mathbf{r}_{new}$ as follows:

$$\mathbf{T}_{new} = \mathbf{T}_{mean} + \mathbf{C}\mathbf{b}_{new}, \tag{2.23}$$

where

$$
\begin{aligned}
\mathbf{T}_{new} &= [\mathbf{T}_{new}{}^1, ..., \mathbf{T}_{new}{}^j, ..., \mathbf{T}_{new}{}^{10}] \quad with \\
\mathbf{T}_{new}{}^j &= \left[\begin{array}{ccccc} a_{new}^{1,j} & \dots & a_{new}^{i,j} & \dots & a_{new}^{20,j} \end{array} \right]
\end{aligned} \tag{2.24}
$$

and $a_{new}^{i,j}$ denotes the computed area of the cavity corresponding to image $\mathcal{I}_{i,j}$ of the new subject.

2.2.5 Fitting Function Approaches

The key point in the proposed technique is finding a relationship between the compact representation of image features ($\mathbf{r}_m$) and the compact representation of LV cavity areas ($\mathbf{b}_m$). While various technique exist for such data fitting, we used Artificial Neural Network (ANN).

Artificial Neural Network Estimation of Left Ventricle Cavity Areas

We constructed an ANN to determine the nonlinear relationship between the Bhattacharyya coefficients (refer to Figs. 2.8, 2.10, 2.12) and the corresponding LV cavity areas (refer to Fig. 2.7, 2.9, 2.11). Following a back propagation ANN, a powerful machine learning technique [5], our feed-forward network consists of five layers, three hidden, one input, and one output (refer to Fig.2.13 for an illustration).
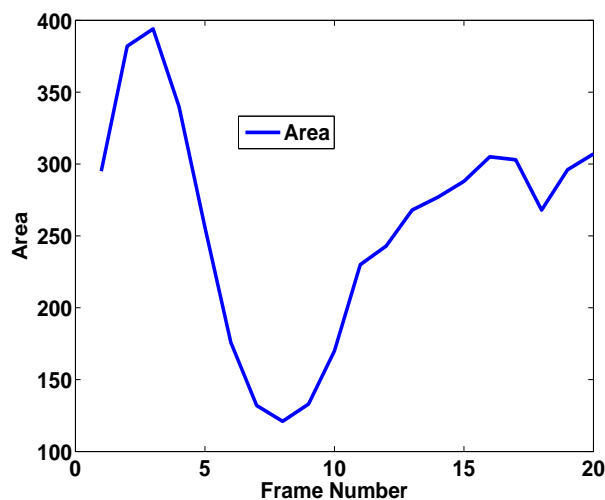
Figure 2.7: A sample example which shows the variations of the LV cavity areas of apical slice obtained from manual segmentations.

Our network estimates the non-linear mapping $\mathbf{F}$, which we used in equation (2.19). We assume $\mathbf{F}$ is a nonlinear transfer function consisting of two hyperbolic tangent functions and a linear function, a common choice in the neural network literature [5]. As illustrated in Fig. 2.13, the resulting network consists of five layers, one input and one output containing 5 neurons each, both based on the linear function ($f(x) = x$), as well as three hidden layers
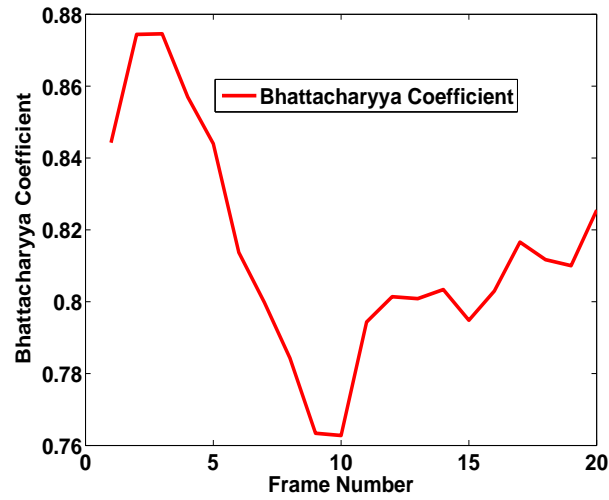
Figure 2.8: A sample example which shows the variations of the Bhattacharyya image statistics of apical slice. We observe that these statistics are non-linearly related to the manually obtained LV cavity areas depicted in Fig. 2.7.
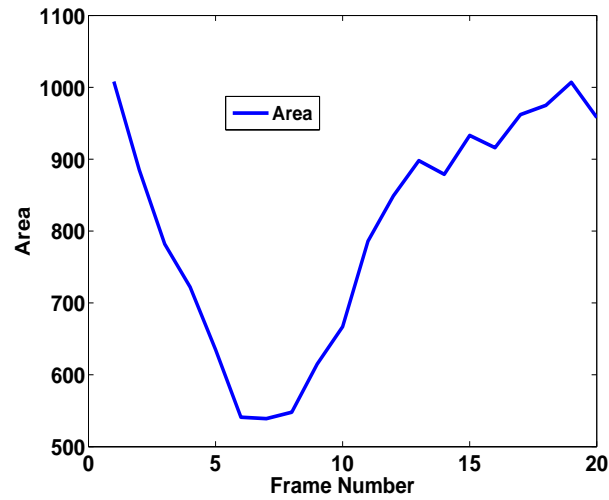
Figure 2.9: A sample example which shows the variations of the LV cavity areas of a midcavity slice obtained from manual segmentations.

containing 50, 25 and 50 neurons and based on the hyperbolic tangent, hyperbolic tangent and linear functions respectively [5].

Let **INPUT** and **OUTPUT** denote the training input and output of the neural network respectively:

$$\mathbf{INPUT} = [(\mathbf{r}_1)^{-1}, ..., (\mathbf{r}_m)^{-1}, ..., (\mathbf{r}_M)^{-1}] \tag{2.25}$$

53
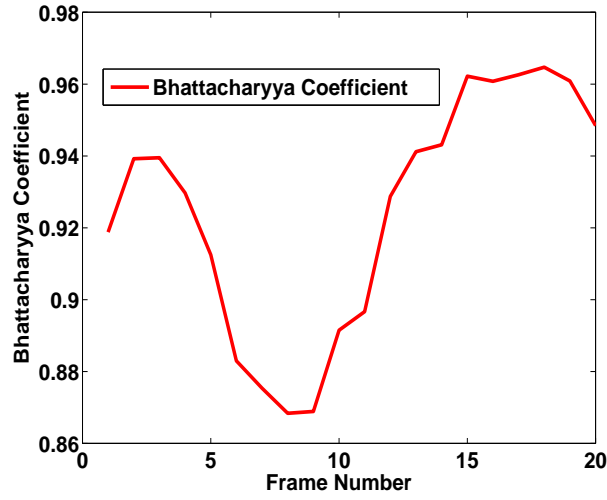
Figure 2.10: A sample example which shows the variations of the Bhattacharyya image statistics of a midcavity slice. We observe that these statistics are non-linearly related to the manually obtained LV cavity areas depicted in Fig. 2.9.
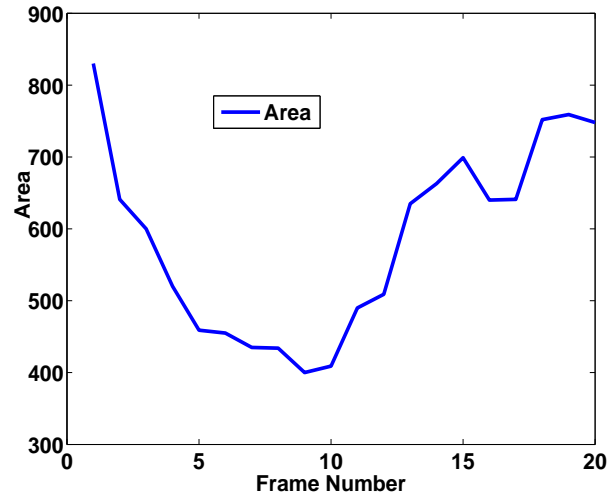
Figure 2.11: A sample example which shows the variations of the LV cavity areas of basal slice obtained from manual segmentations.

$$\mathbf{OUTPUT} = [(\mathbf{b}_1)^{-1}, ..., (\mathbf{b}_m)^{-1}, ..., (\mathbf{b}_M)^{-1}] \tag{2.26}$$

To validate this procedure we employ a leave-one-out approach, where the test dataset was excluded from the training data. For the current testing subject dataset, transferred subject area statistics ($\mathbf{b}_{new}$) were estimated from equation (2.22) using the learned non-linear mapping $\mathbf{F}$
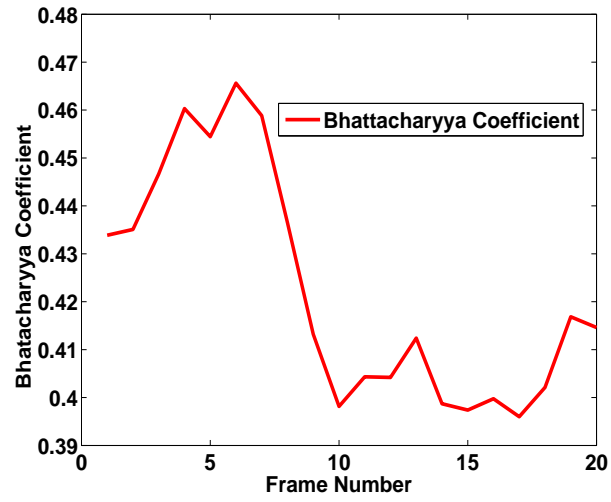
Figure 2.12: A sample example which shows the variations of the Bhattacharyya image statistics of basal slice. We observe that these statistics are non-linearly related to the manually obtained LV cavity areas depicted in Fig. 2.11.

(refer to the illustration in Fig. 2.15). The matrix T_{new}, representing the areas of the LV cavities, was estimated from equation (2.23).
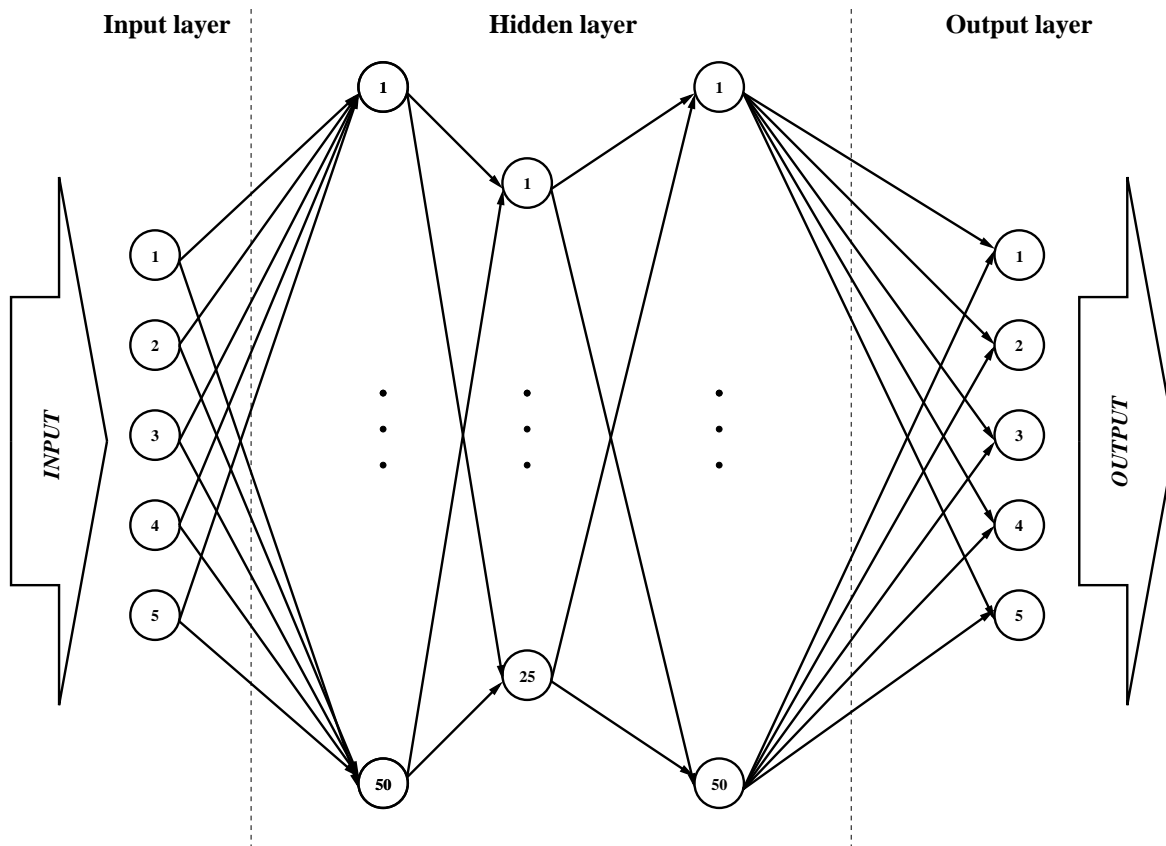
Figure 2.13: The ANN consists of one input layer, three hidden layers, and one output layer.

Training Phase

$\mathbf{P}_m, m = 1 \ldots M$

$\mathbf{T}_m, m = 1 \ldots M$

PCA

INPUT

OUTPUT

ANN

Trained ANN
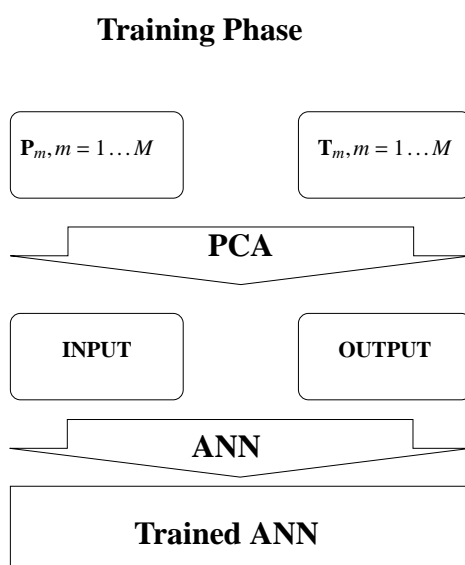
Figure 2.14: The training phase.

Testing Phase

```
┌─────────────────────────────────┐
│              P_m                │
└─────────────────────────────────┘
        │ PCA │
┌─────────────────────────────────┐
│             r_new               │
└─────────────────────────────────┘
      │ Trained ANN │
┌─────────────────────────────────┐
│             b_new               │
└─────────────────────────────────┘
     │ INVERSE  PCA │
┌─────────────────────────────────┐
│             T_new               │
└─────────────────────────────────┘
```
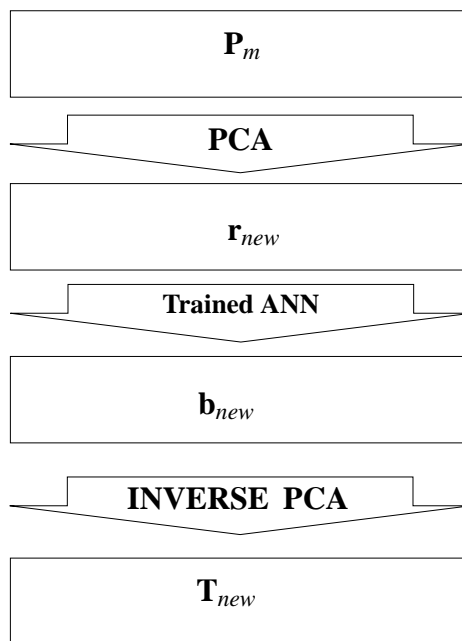
Figure 2.15: The testing phase: the estimated Bhattacharyya statistics are fed to the network and the corresponding LV cavity areas are predicted.
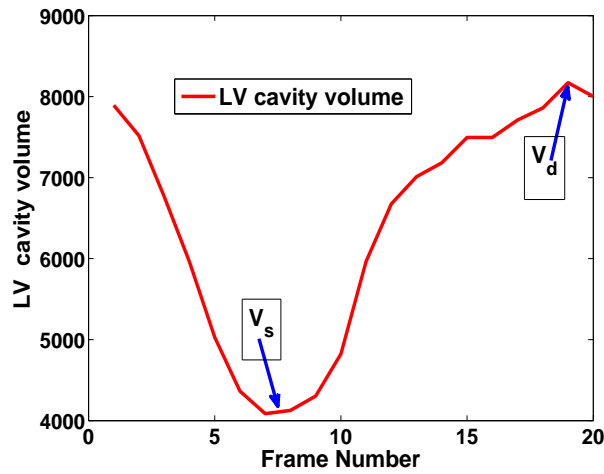
Figure 2.16: Variation of the volume of the LV cavity in each heart beat.

2.3 Estimating the Cardiac Ejection Fraction From Image Statistics

Let V_s and V_d denote the smallest (end-systolic) and largest (end-diastolic) volumes of the LV in a cardiac cycle, respectively (Fig. 2.16). The cardiac ejection fraction, EF, is given by:

$$EF = \frac{V_d - V_s}{V_d} \tag{2.27}$$

The difference in the numerator in equation (2.27) measures the blood volume pumped by the left ventricle. We computed V_s and V_d by integrating the computed LV cavity areas in the sagittal direction.

2.4   Experimental Evaluations and Comparisons

2.4.1   Image Acquisition

A set of 2D short-axis cine Magnetic Resonance (MR) images of 20 subjects was acquired through the cardiac cycle on a 1.5T scanner with fast-imaging employing steady-state acquisition (FIESTA) image sequence mode. The acquisition parameters were as follows: TR=2.98 ms, TE=1.2 ms, flip angle=30 degree, and slice thickness=10 mm. Each subject's dataset consisted of 20 frames, each comprising 10 slices.

2.4.2   Experimental Results

We used the proposed method to automatically compute the LV cavity areas, thereby estimating the LV cavity volumes and ejection fractions of 20 subjects. Each subject's dataset contains 20 frames, each comprising 10 slices. We proceeded to a leave-one-out validation approach, where the training used to compute the LV cavity areas of each subject is based on the other 19 subjects ($M = 19$). Estimated areas were used to compute the LV cavity volumes of each subject. Then, the obtained volumes and ejection fractions were evaluated quantitatively by comparing them with those obtained from independent manual segmentation by an expert.

In Fig. 2.17, we plotted the computed LV cavity areas (all frames and slices) for all 20 patients versus those obtained from independent manual segmentations. We included the identity line, which indicates an excellent correlation between manually and automatically computed areas.

Fig. 2.18 depicts the computed LV cavity volumes for all 20 patients versus those obtained from the independent manual segmentations, as well as the identity line, which indicates an excellent correlation between manually and automatically computed volumes.

We used several statistics to evaluate the conformity between the manually and automatically computed Areas and Volumes (the results are listed in Table. 2.1). First we estimated the correlation coefficient, R, which measures the correlation between e and f; e is a vector
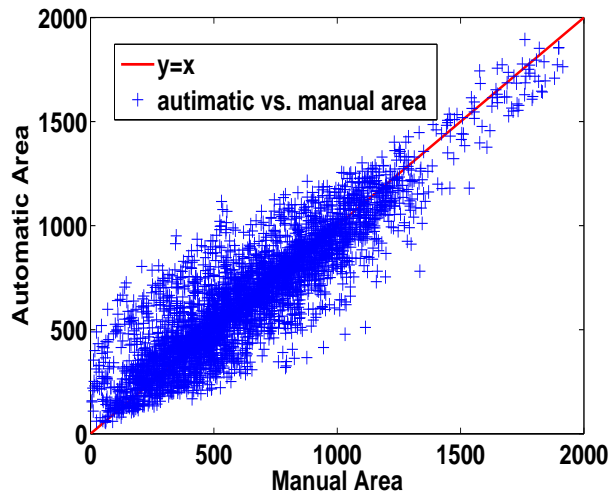
Figure 2.17: Automatic versus manual cavity areas.
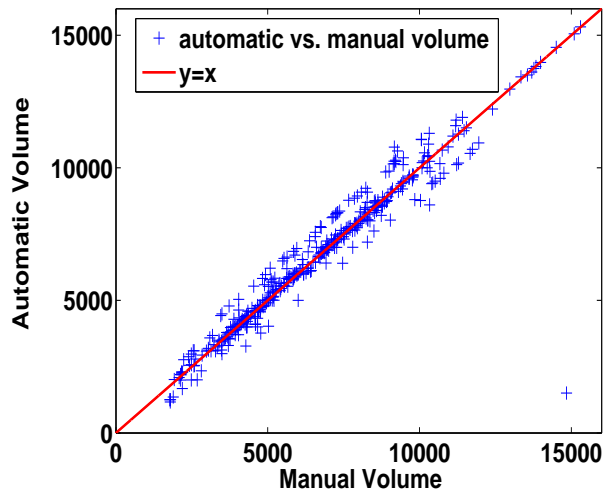
Figure 2.18: Automatic versus manual cavity volumes.

containing the manual estimations of areas (or volumes) and f is the corresponding automatic estimation. The range of R is $[0,1]$, where 1 indicates a perfect fit between the vectors. The proposed method yielded correlation coefficients of 0.8930 and 0.91258 for the LV cavity areas and volumes, respectively, indicating a high conformity between manual and automatic estimations.

We used a two-tailed t-test to estimate the conformity between e and f, which yielded a non-significant $P-value$s of 0.22834 and 0.1943, indicating that automatic estimations of areas and volumes are not significantly different from those obtained from manual segmentation.

	$R(e, f)$	$P-value(t-test)$
Area	0.8930	0.2834
Volume	0.91258	0.1943

Table 2.1: Statistical measures of the conformity between automatically and manually computed areas and volumes.

In the next step, the estimated cavity volumes were used to estimate the EFs for all 20 subjects. Let EF_A be a vector containing the 20 automatically estimated EFs, and EF_M be a vector of the same size containing the EFs obtained form manual segmentations. Fig. 2.19 depicts EF_A and EF_M, and confirms that the EFs computed with the proposed method are very close to those obtained from independent manual segmentations.

We evaluated the conformity between the manually and automatically computed EFs (the results are listed in Table. 2.2). First we evaluated the correlation coefficient, $R(EF_A, EF_M)$. The proposed method yielded a correlation coefficient of 0.9635, which indicates a high conformity between manual and automatic ejection fractions.

We used a two-tailed t-test to estimate the conformity between manually and automatically estimated ejection fraction, which yielded a non-significant $P-value$ of 0.1778.
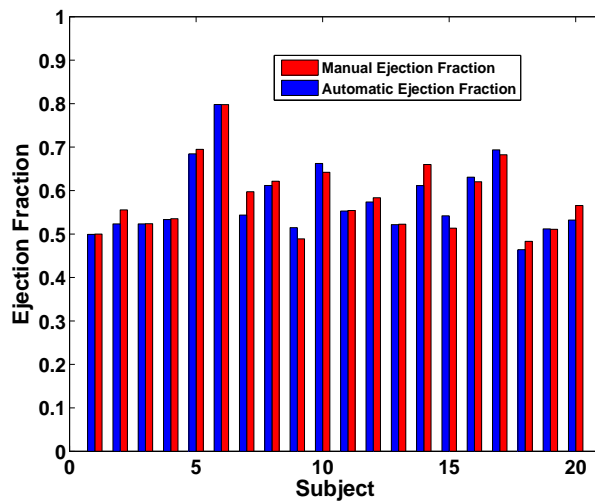
Figure 2.19: Automatic and manual EFs in 20 subjects.

We then evaluated the error quantitatively and comparatively by computing the norm of the

$R(EF_A, EF_M)$	$P-value(t-test)$
0.9635	0.1778

Table 2.2: Statistical measures of the conformity between automatically and manually computed EFs.

method	$mean(Diff_{EF})$	$std(Diff_{EF})$	$CPU(s)$
The proposed method	0.0160	0.0163	0.2087
graph-cut segmentation	0.0965	0.0922	9.62
level-set segmentation	0.1095	0.1253	494.45

Table 2.3: Errors (std and mean) and computation time (in seconds) with the proposed method and with graph-cut and level-set estimation of the EF based on the recent segmentation algorithms in [2, 3].

difference between EF_A and EF_M:

$$Diff_{EF} = \|EF_A - EF_M\| \tag{2.28}$$

Furthermore, the proposed method was compared with computing the EF obtained based on the graph-cut and level-set segmentation algorithms in [2, 3]. Table. 2.3 reports the mean and standard deviation of the error as well as the computation time for the proposed method and the segmentation algorithms in [2, 3], demonstrating that EFs obtained with the proposed method are more accurate and computationally less expensive than those obtained with graph-cut and level-set segmentation [2, 3]. The proposed method estimated the EF in real-time taking 0.209 s per subject using a non-optimized MATLAB code on a 2.2 GHz machine.

Fig. 2.20 depicts the errors (20 subjects) obtained with the proposed method (red curve), the graph-cut segmentation (blue curve), and the level-set segmentation (green curve). The results are based on non-optimized 2D segmentation techniques and we assume that error has been integrated in the estimation of the EF . The proposed method yielded a much lower curve and, therefore, a significant improvement in accuracy.
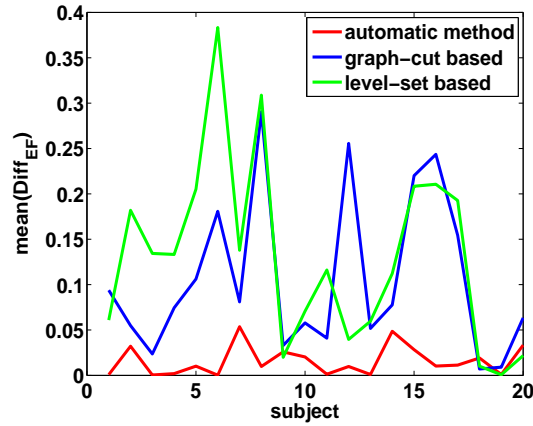
Figure 2.20: Errors (20 subjects) obtained with the proposed automatic method (red curve), the graph-cut segmentation (blue curve), and the level-set segmentation (green curve). The proposed method yielded a much lower curve and, therefore, a significant improvement in accuracy.

2.4.3 Effect of the choice of the number of the most significant eigenvectors (t) on the results

In this study, we computed the number of the most significant eigenvectors (t) by satisfying condition (2.13). In our experiments, this condition yielded $t = 5$. To further evaluate the effect of t on the results and confirm the relevance of condition (2.13), we ran the algorithm over 29 uniformly-spaced values of t in the interval [2; 30]. Fig. 2.21 depicts the mean error as a function of t. We observe that starting from $t = 5$, the mean error does not change significantly. This means that the five most important eigenvectors carry the information we need, and confirms the relevance of condition (2.13).

2.4.4 Effect of the choice of the number of neurons on the results

The proposed ANN consists of three hidden layers. The examine the effect of the choice of the number of neurons on the results, we proceeded to three different sets of comprehensive experiments, each corresponding to varying the number of neurons in one hidden layer and fixing the number of neurons in the two other layers.

In the first set of experiments, we ran the algorithm over 11 uniformly-spaced values of

63
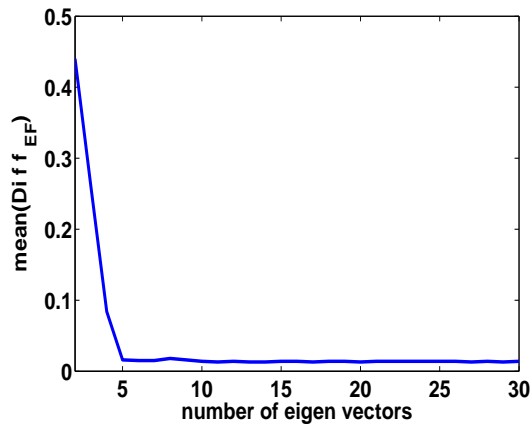
Figure 2.21: Mean error as a function of the number of most significant eigenvectors.

the number of neurons in the first layer. The values are in the interval $[5; 60]$. For this set of experiments, the number of neurons was fixed equal to 25 in the second layer and to 50 in the third layer. Fig. 2.22 depicts the mean error as a function of the number of neurons in the first layer, showing that a choice of value of this number equal to 50 or 40 yields the best performance.

Fig. 2.23 illustrates the second set of experiments, depicting the mean error as a function of the number of neurons in the second hidden layer, which we varied over 6 uniformly-spaced values in the interval $[5; 30]$. We fixed the number of neurons in the first and last layers equal to 50. This set of experiments showed that choosing the number of neurons in the second layer equal to 25 led to the best performance.

The same procedure was followed for the last hidden layer. We fixed the number of neurons in the first and second layers equal to 50 and 25, respectively. Then, the number of neurons in the third layer was varied over 11 uniformly-spaced values in the interval $[5; 60]$. Fig. 2.24 demonstrates that the best performance is reached by choosing the number of neurons in the last layer equal to 50.
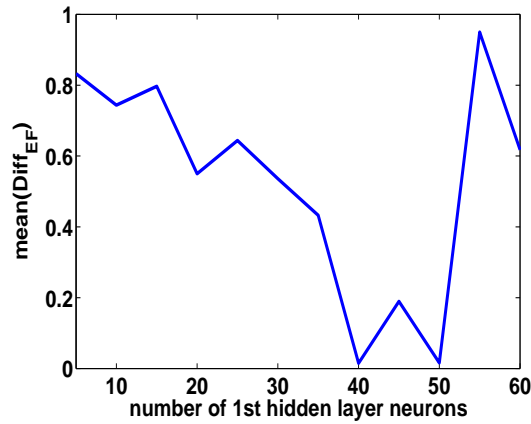
Figure 2.22: Mean error as a function of the number of neurons in the first hidden layer.
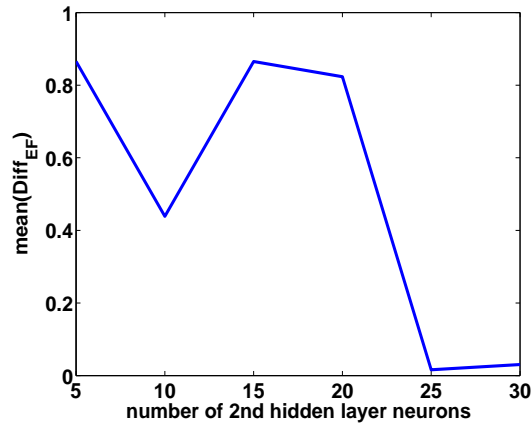
Figure 2.23: Mean error as a function of the number of neurons in the second hidden layer.

2.4.5 Effect of the user-provided input on the results

The proposed method relies on an approximate user-provided localization of the LV cavity (refer to the red curves in Fig. 2.4). Our method assumes the user provides an initial box close to the LV in a single 2D image. Such localization plays a essential role in estimating the image features. We evaluated the robustness of the proposed method with respect to variations in the user-provided input. Fig. 2.25 depicts the mean error obtained with the proposed method as a function of the size of the region (the box) enclosed within the user-provided red curve. We started with an initial box which has approximately the same area as the LV cavity. Then, we evaluated the algorithm by rescaling the box from 1 to 5 times of the initial size. Fig. 2.25 depicts the mean error as a function of the size of the region of interest. The bigger the size of
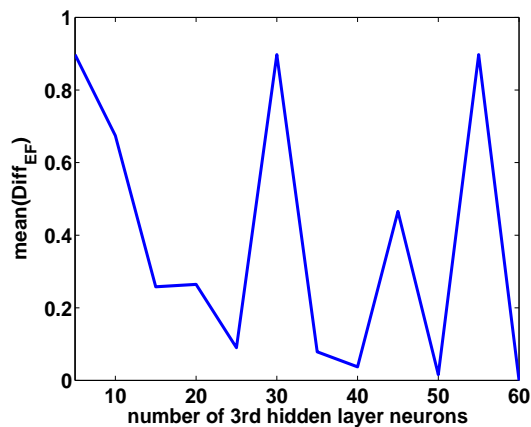
Figure 2.24: Mean error as a function of the number of neurons in the third hidden layer.

the box, the higher the error.
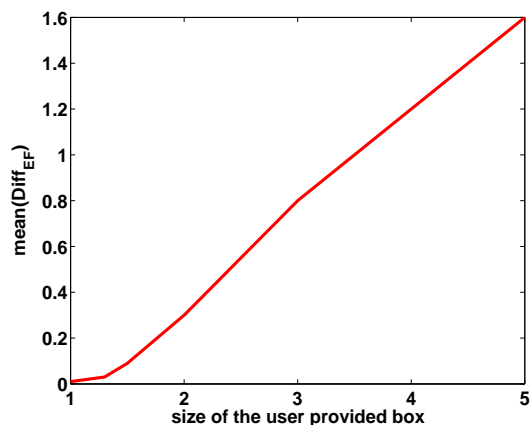
Figure 2.25: Mean error as a function of the size of the user-provided region of interest.

2.4.6 Typical examples

Figs. 2.26 - 2.28 show automatically and manually computed areas for apical, basal and mid-cavity slices of a single object as a function of the frame number.

Figs 2.29-2.31 depict automatically and manually computed volumes for three subjects as a function of frame number. Fig. 2.29 shows the best estimation in the 20 subjects, which corresponds to the lowest error, i.e., the lowest absolute difference between manually and automatically computed volumes. Fig. 2.30 corresponds to the medium error (the medium estimation
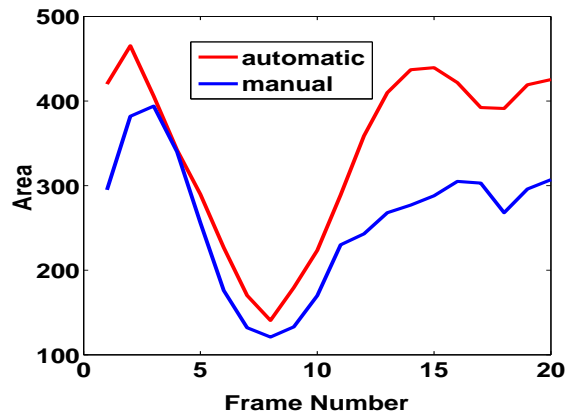
Figure 2.26: Automatic versus manual cavity areas for an apical slice of a single subject.
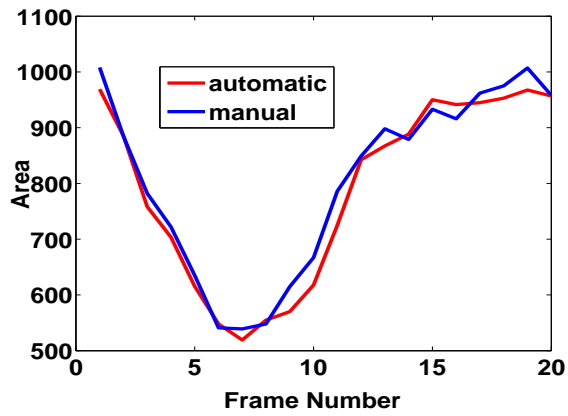
Figure 2.27: Automatic versus manual cavity areas for a mid-cavity slice of a single subject.

in the 20 subjects), and Fig. 2.31 to the highest error (the worst estimation in the 20 subjects).
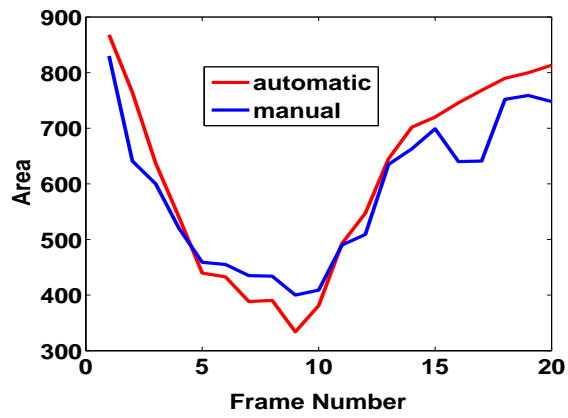
Figure 2.28: Automatic versus manual cavity areas for a basal slice of a single subject.
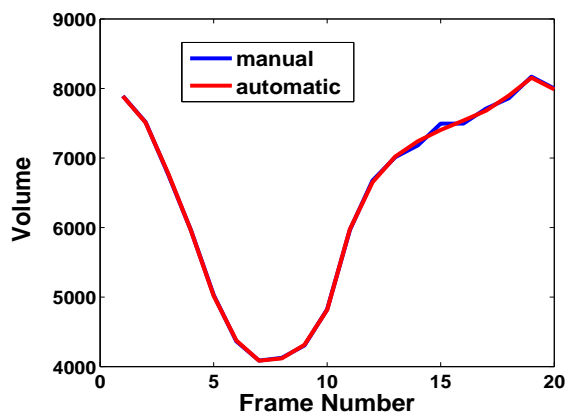
Figure 2.29: Automatic versus manual cavity volumes: the best case in the 20 subjects.
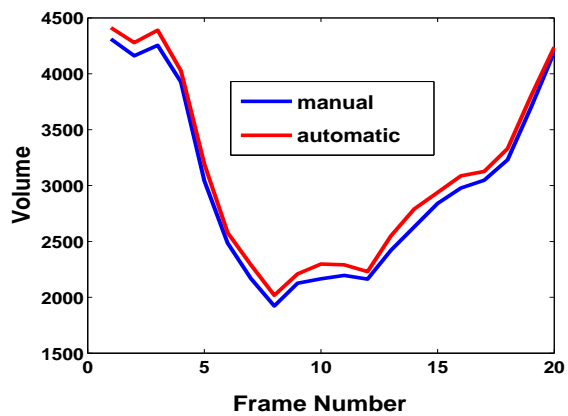
Figure 2.30: Automatic versus manual cavity volumes: the median case in the 20 subjects.
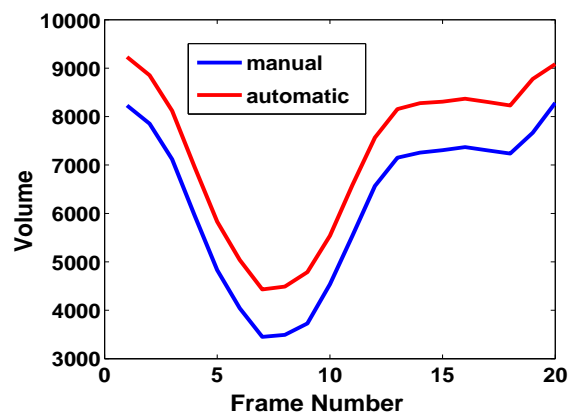
Figure 2.31: Automatic versus manual cavity volumes: the worst case in the 20 subjects.

2.5 Conclusion

This study investigated a real-time method for computing the cardiac *EF* directly (without segmentation) from image statistics via machine learning. These image statistics were based on the Bhattacharyya coefficients of similarity between image distributions, which were shown to be non-linearly related to the LV cavity areas. An ANN was used to find the relation between the image statistics and the corresponding LV cavity areas in each subject dataset. A comprehensive experimental evaluation over 20 subjects demonstrated an excellent conformity of the automatically estimated *EF*s to those computed from manual segmentations. Furthermore, comparison with graph-cut and level-set estimation of the *EF* based on recent segmentation algorithms confirmed that the proposed method can yield a competitive performance while reducing significantly the computational load.

Further future work includes application of the proposed method to the estimation of other cardiac functions such as muscle thickening and to the detection of cardiac abnormalities. Also, it is worth noting that the proposed method is based on the consistency of the image distributions within the cavity across different frames. Therefore, it can readily extend to other modalities where such consistency is verified as is the case for CT, for instance. It would be interesting to assess the applicability of the method to modalities other than MRI.

References

[1] A. Andreopoulos and J. K. Tsotsos, "Efficient and generalizable statistical models of shape and appearance for analysis of cardiac MRI," *Medical Image Analysis*, vol. 12, no. 3, pp. 335–357, 2008.

[2] I. Ben Ayed, K. Punithakumar, A. Islam, J. Chong, and S. Li, "Left ventricle segmentation via graph cut distribution matching," in *Medical Image Computing and Computer-Assisted Intervention; MICCAI*, vol. 5762, 2009, pp. 901–909.

[3] I. Ben Ayed, I. Ross, and S. Li, "Embedding overlap priors in variational left ventricle tracking," *IEEE Transaction on Medical Imaging*, vol. 28, no. 12, pp. 1902–1913, 2009.

[4] T. F. Cootes, C. J. Taylor, D. H. Cooper, and J. Graham, "Active shape models, their training and application," *Computer Vision and Image Understanding*, vol. 61, no. 1, pp. 38–59, 1995.

[5] L. V. Fausett, *Fundamentals of neural networks: architectures, algorithms, and applications*, L. Fausett, Ed. Prentice-Hall Inc., 1994.

[6] M. Fradkin, C. Ciofolo, B. Mory, G. Hautvast, and M. Breeuwer, "Comprehensive segmentation of cine cardiac MR images," in *Medical Image Computing and Computer-Assisted Intervention; MICCAI*, vol. 5241, 2008, pp. 178–185.

[7] H. Y. Lee, N. Codella, M. Cham, J. Weinsaft, and Y. Wang, "Automatic left ventricle segmentation using iterative thresholding and an active contour model with adaptation on

short-axis cardiac MRI," *IEEE Transactions on Biomedical Engineering*, vol. 57, no. 4, pp. 905–913, 2010.

[8] M. Lynch, O. Ghita, and P. Whelan, "Automatic segmentation of the left ventricle cavity and myocardium in MRI data," *Computers in Biology and Medicine*, vol. 36, no. 4, pp. 389–407, 2006.

[9] O. Michailovich, R. Yogesh, and A. Tannenbaum, "Image segmentation using active contours driven by the bhattacharyya gradient flow," *IEEE Transaction on Image Processing*, vol. 16, no. 11, pp. 2787–2801, 2007.

[10] A. Pednekar, R. Muthupillai, V. V. Lenge, I. A. Kakadiaris, and S. D. Flamm, "Automatic identification of the left ventricle in cardiac cine-MR images: Dual-contrast cluster analysis and scout-geometry approaches," *Journal of Magnetic Resonance Imaging*, vol. 23, no. 5, pp. 641–651, 2006.

[11] C. Petitjean and J.-N. Dacher, "A review of segmentation methods in short axis cardiac MR images," *Medical Image Analysis*, vol. 15, no. 2, pp. 169–184, 2011.

[12] N. Toda, K.-I. Funahashi, and S. Usui, "Polynomial functions can be realized by finite size multilayer feedforward neural networks," in *IEEE International Joint Conference on Neural Networks*, vol. 1, 1991, pp. 343–348.

[13] J. Zhu-Jacquot and R. Zabih, "Segmentation of the left ventricle in cardiac MR images using graph cuts with parametric shape priors," in *IEEE International Conference on Acoustics, Speech and Signal Processing; ICASSP*, 2008, pp. 521–524.

Chapter 3

Regional Assessment of Cardiac Left Ventricle Function

3.1 Regional Assessment of Cardiac Left Ventricular Myocardial Function via MRI Statistical Features

Early and accurate detection of segmental (regional) Left Ventricle (LV) abnormalities in Magnetic Resonance Imaging (MRI) is important for diagnosing cardiac disease as discussed in chapter 1. In routine clinical use, cardiac function is estimated by visual assessment of the LV function, therefore it is observer-dependent and non-repeatable. Alternatively, an automatic, fast and accurate diagnosis method of the LV function is desired. Computer-aided detection systems have been attempted in recent years in order to automatically analyze the LV myocardial function quantitatively [20], and to classify cardiac function into normal or abnormal

---

[1]This chapter is based on three papers:
1) Afshin, M., Ben Ayed, I., Punithakumar, P., Law, Max W. K., Islam, A., Ross, I., Peters, T., Li, S., "Assessment of Regional Myocardial Function via Statistical Features in MR Images", Medical Image Computing and Computer Assisted Interventions (MICCAI), Vol 6893, pp.107-114 (2011).
2) Afshin, M., Neshat, H.R., Islam, A., Goela, A., Ross, I., Li, S., "Regional Assessment of Cardiac Left Ventricle from MRI with Minimum User Interaction", Radiological Society of North America (accepted in RSNA 2012).
3) Afshin, M., Ben Ayed, I., Punithakumar, P., Islam, A., Goela, A., Ross, I., Peters, T., Li, S., " Regional Assessment of Cardiac Left Ventricular Myocardial Function via MRI Statistical Features", under revision in IEEE Transaction on Medical Imaging.

[51]. In clinical practice, the regional myocardial function is commonly scored by following AHA standards [2], where the LV is divided into 17 segments. Therefore, regional LV abnormality analysis is desirable for clinical purposes. As discussed in section 1.6, the existing regional heart function analysis methods are based on information theoretic measures and an unscented Kalman filter [14], shape models with localized variations [9] or using differentiable manifolds [4], an independent component analysis classifier [21], a pattern recognition method based on intra-segment correlation [11], a hidden Markov model for local wall motion classification based on stress echocardiography [15], and a tensor-based classification to conserve the spatio-temporal structure of the myocardium deformation [12]. Most of the existing methods require either extensive user interaction or computationally expensive segmentation algorithms. However, despite such an effort, the problem is still challenging, with a large room for improvements in regard to accuracy.

The purpose of this chapter is to investigate a real-time machine-learning approach which uses image features that can be easily computed, but that nevertheless correlate well with the segmental cardiac function. We build image features for all the regional segments in a dataset from a simple user input in only one frame. The MR image features are based on a measure of similarity between distributions . We determine that, these statistical features are correlated to the segmental blood pool, the portion of blood within each segment, and can therefore be used to describe segmental contraction without requiring the LV segmentation in all frames. We find the optimal direction along which the estimated image features are most descriptive using Linear Discriminate Analysis (LDA). Then, a Linear Support Vector Machine (LSVM) classifier is used to assess abnormality dysfunction of each of the LV regional segments in real-time. We demonstrate a comprehensive evaluation of the proposed method over cardiac segments obtained from 58 subjects. The proposed algorithm results in an overall accuracy of 86.08% compared to ground-truths obtained by expert radiologists.

3.2 Identifying 16 Segments in Only One Frame

This step requires a user-provided delineation of the endo- and epicardium boundaries in only a single frame, which we refer to as the *reference* frame. Following the AHA standard [2], we use such a simple user input to divide the heart into 16 standard segments. Then, we superimpose the obtained segments systematically (without additional user effort) to all the other frames.

Constructing the 16 segments follows standard AHA prescriptions [2], and is based on the following steps:

- Dividing the LV into equal thirds perpendicular to the long axis of the heart, thereby generating three circular LV sections: apical (Fig. 3.1 a), mid-cavity (Fig. 3.1 b), and basal (Fig. 3.1 c). As prescribed in [2], we use only three representative slices containing the myocardium in all $360°$;

- Dividing the basal part into six segments of $60°$ each, as shown in Fig. 3.2(c). We used the attachment of the right ventricular wall to the LV (septal wall) as anatomical landmark to identify the septum.

- Dividing the apical part into four segments of $90°$ each, as shown in Fig. 3.2(a).

- Dividing the mid-cavity part is into six segments of $60°$ each, as shown in Fig. 3.2(b).

(a): apical   (b): mid-cavity   (c): basal
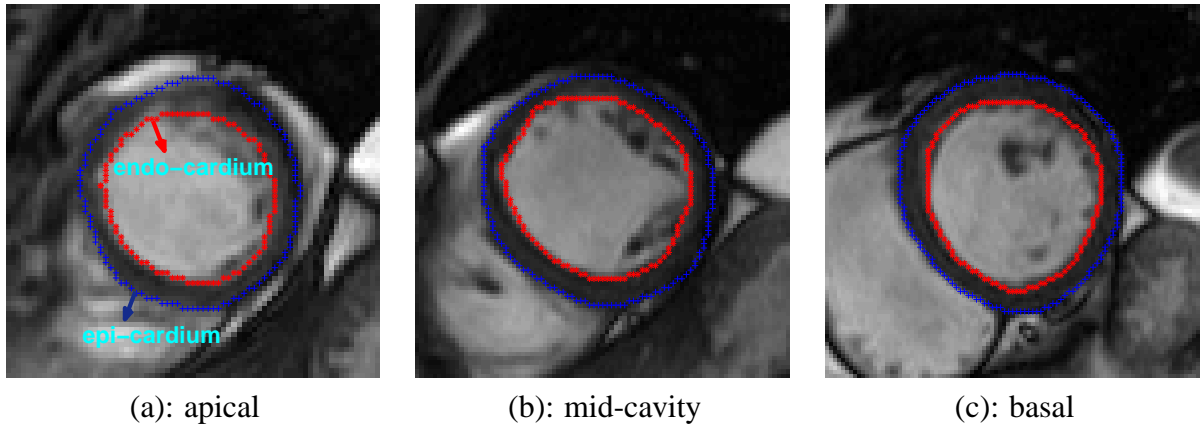
Figure 3.1: User-provided delineation in one single frame (reference image $\mathbf{I}_s$) for three representative slices: (a) apical, (b) mid-cavity and (c).

(a): apical   (b): mid-cavity   (c): basal
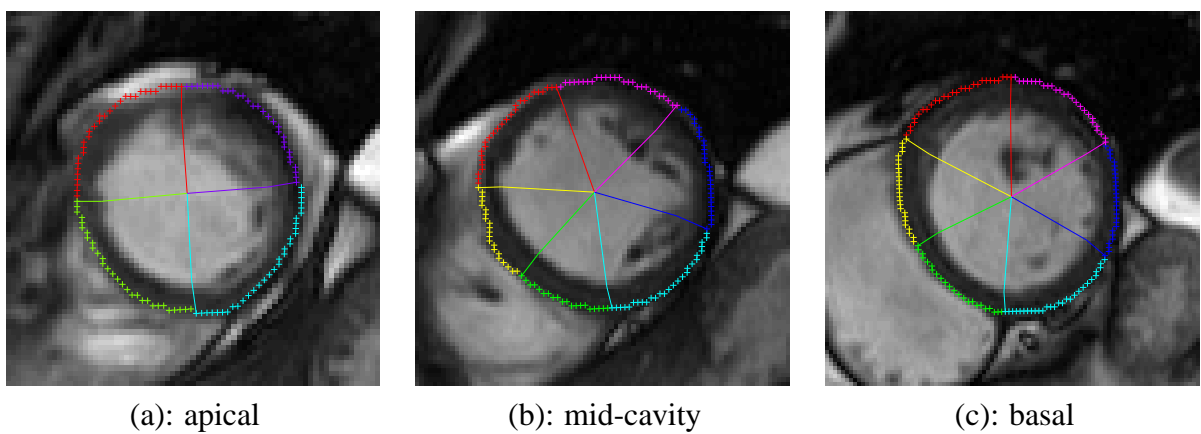
Figure 3.2: The regional segments superimposed on reference image $\mathbf{I}_s$.

3.3 Constructing Statistical Features from MRI Images:

We propose to use image statistics as input features to classify regional myocardial segments into normal and abnormal.

3.3.1 A synthetic Example:

Let us first describe the concept for the simple synthetic-motion example in Fig. 3.3, which depicts several frames, each containing two regions, a white disc (which we denote region x_i) and a black ring enclosing x_i (which we denote region y_i); i is an integer denoting the frame number ($i \geq 1$).

During a simulated cardiac cycle, region x_i is shrinking and expanding, mimicking the LV blood cavity during a cardiac cycle, whereas region $x_i \cup y_i$ remains constant ($x_i \cup y_i$ corresponds to the whole image domain $\forall i$). Let Q_i denotes the intensity within frame i:

$$Q_i(p) = 1 \quad \forall p \in x_i$$
$$Q_i(p) = 0 \quad \forall p \in y_i \tag{3.1}$$

Let $P(./x_i)$ and $P(./x_i \cup y_i)$ denote respectively the probability distributions of intensity within regions x_i and $x_i \cup y_i$:

$$P(Q_i = 1/x_i) = P(Q_1 = 1/x_1) = 1 \quad \forall i$$
$$P(Q_i = 0/x_i) = P(Q_1 = 1/x_1) = 0 \quad \forall i$$
$$P(Q_i = 1/x_i \cup y_i) = \frac{a_i}{A} \quad \forall i$$
$$P(Q_i = 0/x_i \cup y_i) = \frac{A - a_i}{A} \quad \forall i \tag{3.2}$$

where a_i denote the area of region x_i within time frame i, and A the area of the image domain.

Now let us consider the Bhattacharyya coefficient introduced in the previous chapter that measures the amount of overlap (similarity) between two distributions f and g:

$$\mathbf{B_Z}(f,g) = \sum_{z \in \mathbf{Z}} \sqrt{f(z)g(z)} \qquad (3.3)$$

where $\mathbf{Z}$ is the set of values over which the distributions are defined. For this synthetic example, $\mathbf{Z} = \{0,1\}$. Note that the range of the Bhattacharyya coefficient is $[0,1]$, with 0 indicating no overlap between the distributions and 1 indicating a perfect match.

Let us assume that we have a segmentation (delineation) of region x in only the first frame, i.e., only x_1 is known (for $i \geq 2$, x_i is not segmented). For each $i \geq 2$, we can show that the following image statistic is directly related to the area of region x_i:

$$\mathbf{B}_{\{0,1\}}(P(./x_1), P(./x_i \cup y_i)) = \sqrt{0 \times P(0/x_i \cup y_i) + 1 \times P(1/x_i \cup y_i)} = \sqrt{\frac{a_i}{A}} \qquad (3.4)$$

Notice that computation of the image statistic in the right-hand side of (3.4) does not need a segmentation of x_i for $i \geq 2$; it depends only on x_1 and the whole image in the subsequent time steps. Nonetheless, it is related to the areas of regions x_i and, therefore, contains information about the dynamics of these regions. This makes sense because the more overlap between the distribution of region x_i and the whole image, the larger the proportion of pixels within region x_i.

We will use this concept to build cardiac-segment statistics that correlate well with regional LV function, while removing the need for comprehensive segmentations of all the images in a cardiac sequence.

Figure 3.3: A simple synthetic example which demonstrates how some segmentation-free image statistics correlate with the dynamics of a moving region. The larger circle is a fixed region while the size of the smaller circle varies. The smaller circle illustrates the cavity motion.

3.3.2 Building Segmental Image Statistics for Cardiac MRI Images:

Let $\mathcal{I}$ be a cardiac MRI sequence containing J frames[1], each comprising S slices[2] $\mathcal{I}_{s,j}$: $\Omega \subset \mathfrak{R}^2 \to \mathfrak{R}^+$ with $(s, j) \in [1\ldots S] \times [1\ldots J]$. For each frame, we have I regional segments[3] $\mathcal{K}_{i,j}$, with $(i, j) \in [1\ldots I] \times [1\ldots J]$.

Let us first consider the following basic definitions and notations:

- **I** is the reference frame, which consists of three 2D images, $\mathbf{I}_s, s = 1, \ldots, 3$, each associated with a different slice level (apical, basal, and mid-cavity). The reference frame corresponds to the end-diastolic phase.

- Let $\Gamma_{in}^s, \Gamma_{out}^s : [0, 1] \to \Omega$ denote respectively the endo and epi-cardial boundaries in $\mathbf{I}_s$ (refer to Fig. 3.4.a).

- Let $\Gamma^i : [0, 1] \to \Omega$ denote the boundary of regional segment i in the reference frame (refer to Fig. 3.5 for an illustration).

Now, for each i, let us superimpose systematically (i.e., without additional user effort) segment boundary $\Gamma^i : [0, 1] \to \Omega$ onto the rest of the frames as shown in Fig. 3.4, and compute the corresponding image statistics (Figs. 3.6, 4.2, 3.8).

---

[1]J is typically equal to 20 or 25.
[2]S is equal to 3; we used 3 representative slices following the AHA standard [2].
[3]The number of regional segments (I) per subject is equal to 16.
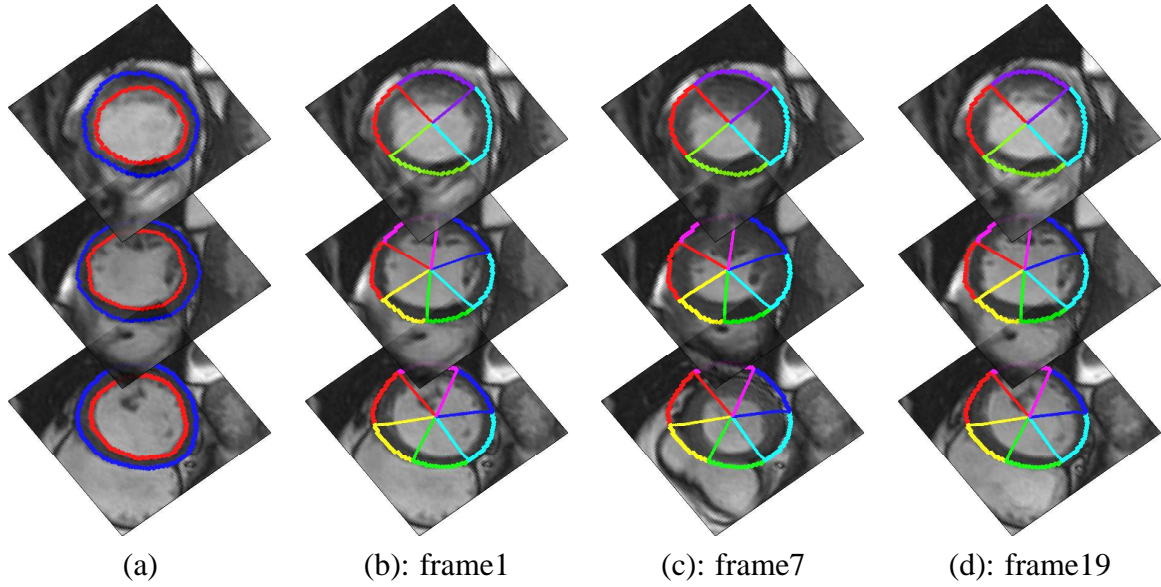
Figure 3.4: (a): Manual segmentation of the reference (end-diastolic) frame. (b): Regional segments of the reference frame. (c-d): regional segments of the reference frame superimposed systematically (without additional user effort) onto the rest of the frames.

To formally introduce the expression of the image statistic for each regional segment at each time step, let us consider the following general definitions:

- Let $\mathbf{R}_\Gamma \subset \Omega$ denote the region enclosed within curve Γ, $\Gamma \in \{\Gamma_{in}^s, \Gamma_{out}^s, \Gamma^i\}$

- Let $P_{\mathbf{R},A}$ denote the kernel density estimate of the distribution of an image A within region $\mathbf{R}$:

$$P_{\mathbf{R},A}(z) = \frac{\int_{\mathbf{R}} K(z - A(x))dx}{a_{\mathbf{R}}} \quad \forall A \in \{\mathcal{I}_{s,j}\}, (s,j) \in [1\ldots S] \times [1\ldots J] \qquad (3.5)$$

where $a_{\mathbf{R}}$ is the area of region $\mathbf{R}$

$$a_{\mathbf{R}} = \int_{\mathcal{R}^+} dx \qquad (3.6)$$

and K is the Gaussian kernel [1]:

$$K(y) = \frac{1}{\sqrt{2\pi\sigma^2}} exp^{-\frac{y^2}{2\sigma^2}}. \qquad (3.7)$$

80

Γ_{out}^s Γ_{in}^s Γ^i

(a) (b) (c)
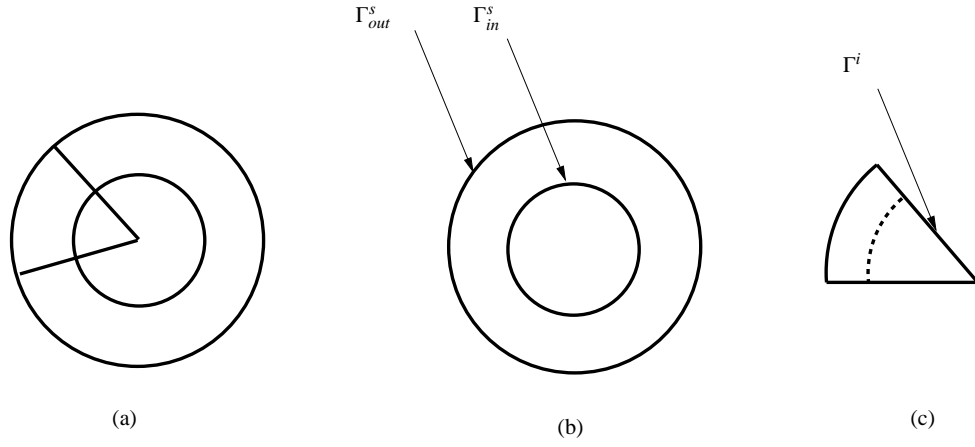
Figure 3.5: (a) Reference image $\mathbf{I}_s$; (b) Endo and epi-cardial boundaries in $\mathbf{I}_s$; (c) boundary of regional segment i in the reference frame.

$\mathcal{K}_{13,1}$ ... $\mathcal{K}_{13,7}$ ... $\mathcal{K}_{13,19}$ ...

(a) ... (b) ... (c) ...

(d) ... (e) ... (f) ...

$\beta^{13,1} = 0.89875$ ... $\beta^{13,7} = 0.87174$ ... $\beta^{13,11} = 0.80551$ ...
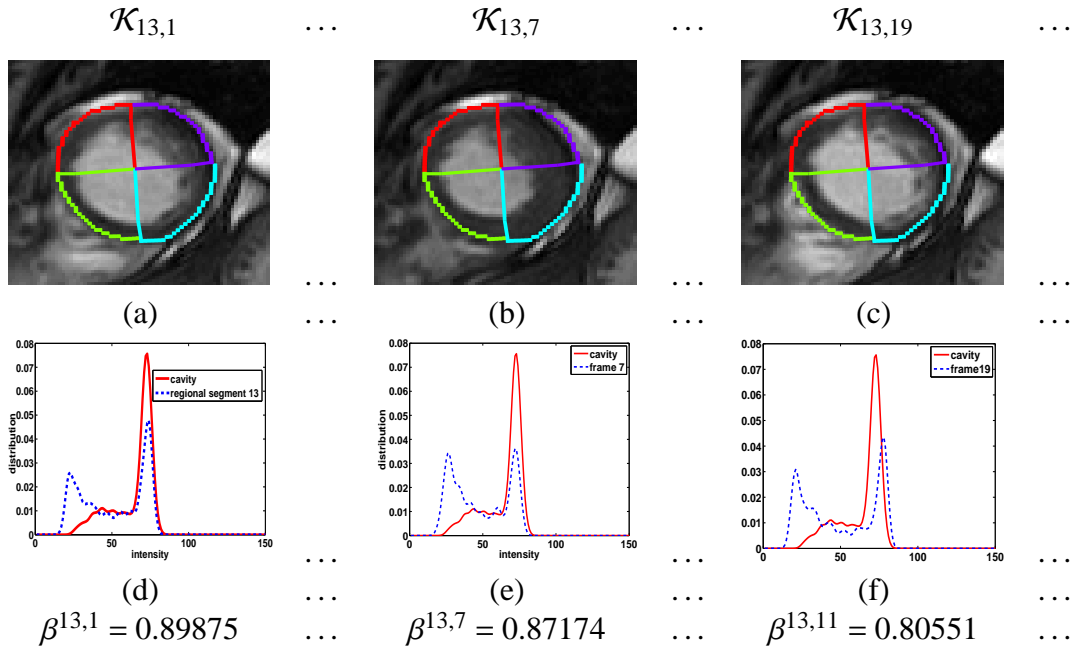
Figure 3.6: (a-c): Regional myocardial segments of an apical slice superimposed on subsequent frames. (d-f): The corresponding image statistics.

We assume the following:

- The reference-image distribution within the region inside Γ_{in} ($P_{\mathbf{R}_{\Gamma_{in}},\mathbf{I}_s}$) approximates the cavity distribution;

- The distribution of each image $\mathcal{I}_{s,j}$ within Γ^i approximates the image distribution within

81

$\mathcal{K}_{7,1}$ $\ldots$ $\mathcal{K}_{7,7}$ $\ldots$ $\mathcal{K}_{7,19}$ $\ldots$

(a) $\ldots$ (b) $\ldots$ (c) $\ldots$

(d) $\ldots$ (e) $\ldots$ (f) $\ldots$

$\beta^{7,1} = 0.91593$ $\ldots$ $\beta^{7,7} = 0.76843$ $\ldots$ $\beta^{7,19} = 0.80551$ $\ldots$
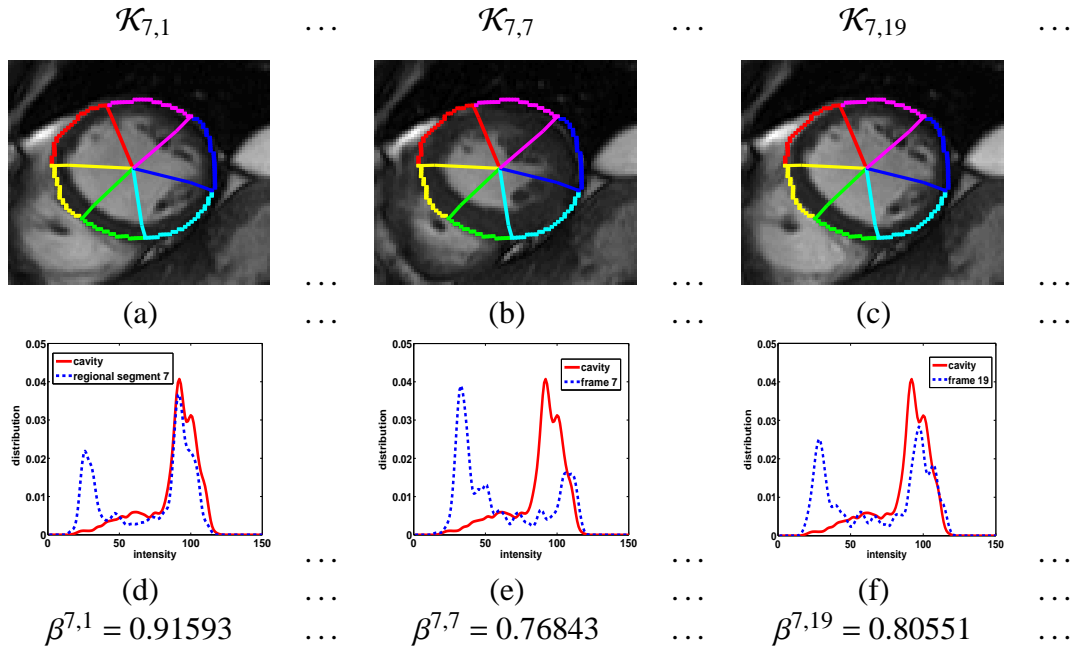
Figure 3.7: (a-c): Regional myocardial segments of a mid-cavity slice superimposed on subsequent frames. (d-f): The corresponding image statistics.

$\mathcal{K}_{1,1}$ $\ldots$ $\mathcal{K}_{1,7}$ $\ldots$ $\mathcal{K}_{1,19}$ $\ldots$

(a) $\ldots$ (b) $\ldots$ (c) $\ldots$

(d) $\ldots$ (e) $\ldots$ (f) $\ldots$

$\beta^{1,1} = 0.91593$ $\ldots$ $\beta^{1,7} = 0.76843$ $\ldots$ $\beta^{1,19} = 0.80551$ $\ldots$
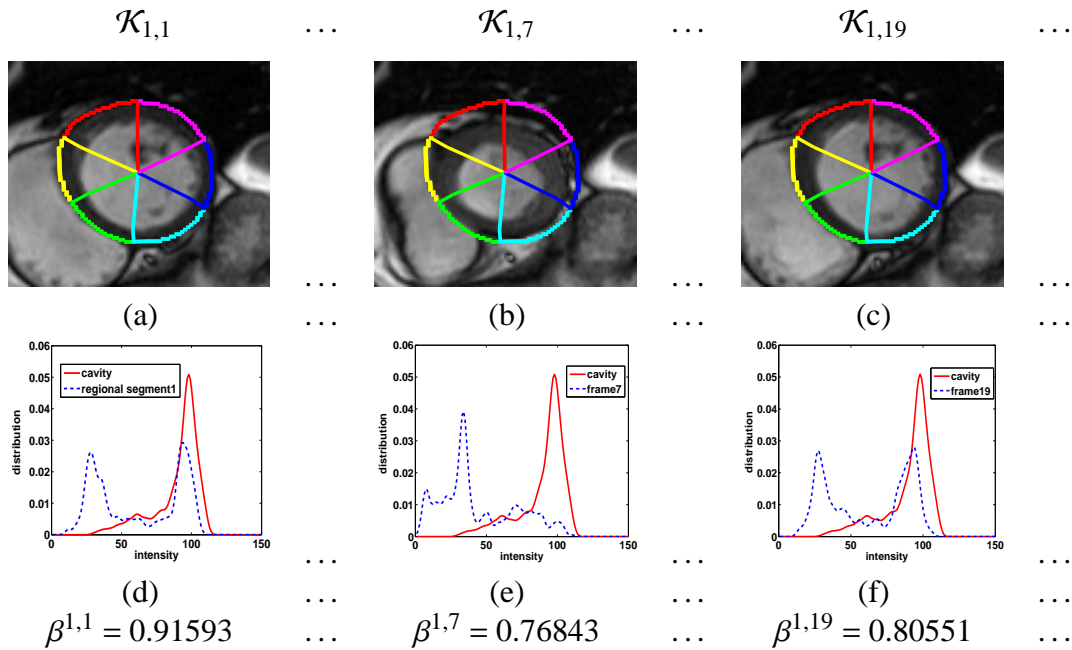
Figure 3.8: (a-c): Regional myocardial segments of a basal slice superimposed on subsequent frames. (d-f): The corresponding image statistics.

regional segment $\mathcal{K}_{i,j}$, i.e.,

$$P_{\mathbf{R}_{\Gamma^i, \mathcal{I}_{s,j}}} \approx P_{\mathcal{K}_{i,j}, \mathcal{I}_{s,j}} \qquad (3.8)$$

As we shall see shortly, this approximation can be effectively used to compute, without the need for segmentation, an image statistic that correlates well with the amount of blood within segment $\mathcal{K}_{i,j}$.

Now, as a statistical feature for each regional segment $\mathcal{K}_{i,j}$, we consider the following Bhattacharyya similarity measure between distributions:

$$\beta^{i,j} = \mathbf{B}_{\mathfrak{R}^+}(P_{\mathbf{R}_{\Gamma_{in}}, \mathbf{I}_s}, P_{\mathbf{R}_{\Gamma^i, \mathcal{I}_{s,j}}}), \qquad (3.9)$$

In a way conceptually similar to the synthetic example we discussed earlier, we expect that feature $\beta^{i,j}$ is related to the proportion of blood within regional segment $\mathcal{K}_{i,j}$. We further demonstrate experimentally such a relationship by the typical examples in Figs. 3.6, 4.2, 3.8, which show that the more overlap (similarity) between the distributions of the cavity and regional segment $\mathcal{K}_{i,j}$, the larger the proportion of blood within the segment. Therefore, we anticipate that over a cardiac cycle, the set of features $\beta^{i,j}$, $j \in [1 \ldots J]$, can characterize segmental cavity contraction. Another way to see how features $\beta^{i,j}$ can describe segmental function is to consider the extreme case where the regional segment does not move. In such case, the proportions of blood is constant over a cardiac cycle, and so are the features.

Fig. 3.9 summarizes the procedure of estimating the statistical image-based features.
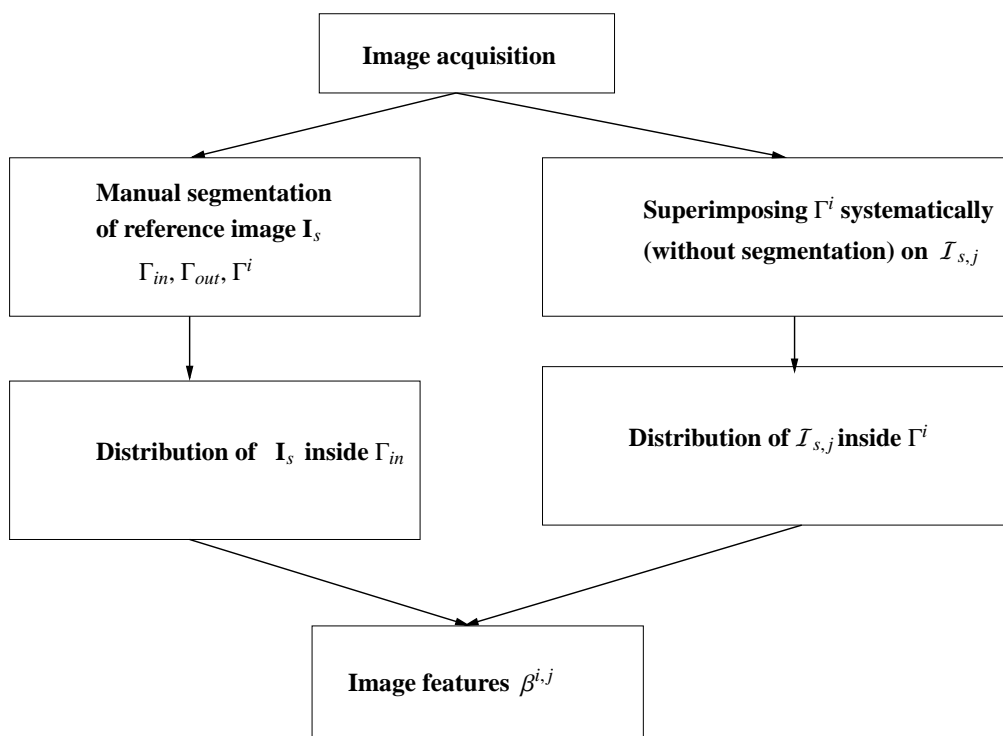
Figure 3.9: The procedure of estimating the statistical image-based features.

3.4 Dimensionality Reduction via Linear Discriminant Analysis

The Bhattacharyya statistics from M training subjects can be viewed as a cloud of M points in the J-dimensional Euclidian space. We proceeded to a Linear Discriminant Analysis (LDA) [23, 8, 22, 24] to reduce the dimensionality of the image features. Following LDA [23], one can assume that these points lie within a lower-dimensional space. Consider the following definitions and notations:

- Let feature vector $\vec{\beta}_m^i = [\beta^{i,1}, \ldots, \beta^{i,j}, \ldots, \beta^{i,J}]$ be a J-dimensional row matrix containing the Bhattacharrya statistics for a given training subject $m, m \in \{1, \ldots M\}$.

- Assume that each feature vector $(\vec{\beta}_m^i)$ belongs to one of two classes C_1 and C_2, where C_1 and C_2 represent respectively normality and abnormality condition of the corresponding regional segment.

- Let μ_e be the mean of feature vectors in class C_e, $e \in \{1, 2\}$:

$$\mu_e = \frac{1}{N_e} \sum_{\vec{\beta}_m^i \in C_e} \vec{\beta}_m^i, \tag{3.10}$$

where N_e is the number of the feature vectors in class C_e.

- Let μ be the mean of all feature vectors:

$$\mu = \frac{1}{M} \sum_{m=1}^{M} \vec{\beta}_m^i. \tag{3.11}$$

The between-class scatter matrix S_b [6] is defined as:

$$S_b = \frac{1}{N} \sum_{e=1}^{2} N_e \, (\mu_e - \mu) \, (\mu_e - \mu)^T, \tag{3.12}$$

and the within-class scatter matrix [6] S_w is defined as:

$$S_w = \frac{1}{N} \sum_{e=1}^{2} \sum_{\vec{\beta}_m^i \in C_e} (\vec{\beta}_m^i - \mu_e)(\vec{\beta}_m^i - \mu_e)^T, \tag{3.13}$$

where N is the number of the feature vectors in both classes.

In LDA [6], a projection vector G is chosen so as to maximize the following ratio:

$$G_{opt} = argmax_G \frac{G^T S_b G}{G^T S_w G} \tag{3.14}$$

Maximizing such a ratio seeks to reduce dimensionality while preserving as much of the class discriminatory information as possible. In the 2-class case, LDA finds a vector $G_{opt} \in \mathfrak{R}^{J \times 1}$ ($1 \leq J$) that maps original data $\vec{\beta}_m^i$ to a scalar $\vec{\beta_{mp}^i}$:

$$G_{opt} : \vec{\beta}_m^i \in \mathfrak{R}^J \rightarrow \vec{\beta_{mp}^i} \in \mathfrak{R}^1$$
$$\vec{\beta_{mp}^i} = G_{opt}^T \vec{\beta}_m^i \tag{3.15}$$

Equation (3.15) is equivalent to projecting the data onto a line that maximizes the class separability of the scalars.

In the next step, we use a Linear Support Vector Machine (LSVM) classifier to classify the projected features ensuing from a given testing subject into normal or abnormal. Fig. 3.10 summarizes the overall classification procedure.
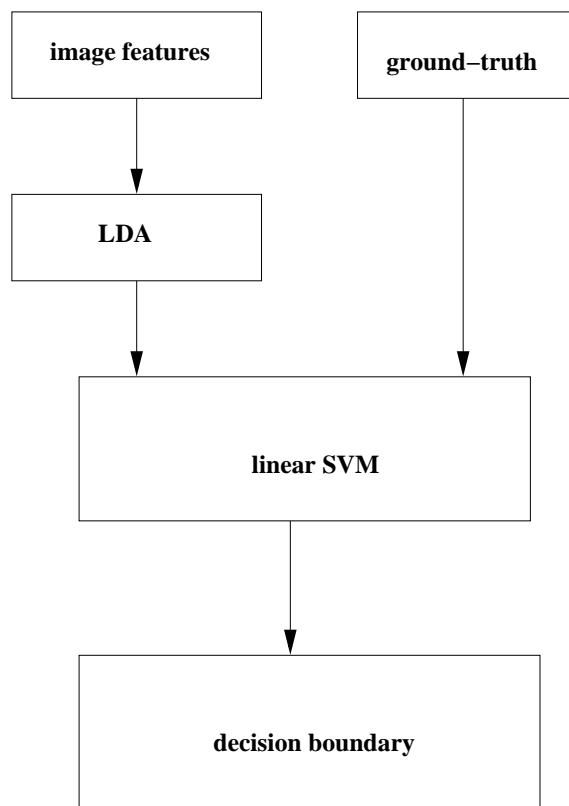
Figure 3.10: Overview of the training phase.

3.5 Linear Support Vector Machine Classification of Regional Segments

This step consists of classifying regional myocardial segments with a Linear Support Vector Machine (LSVM), given projected features $\vec{\beta}_{mp}^{i}$ (refer to Fig. 3.11). Let $(\vec{\beta}_{mp}^{i}, t_m)$, $m = 1, ..., M$, be an annotated training set, with t_m denoting the labels associated with $\vec{\beta}_{mp}^{i}$. Variable t_m has two possible values ($t_m \in \{-1, 1\}$), 1 corresponding to the abnormal-segment class and -1 to the normal-segment class. The two-class LSVM classifier evaluates the sign of a linear function the form [13, 10, 16, 15, 2]:

$$y(\mathbf{x}) = \mathbf{w}^T \phi(\mathbf{x}) + b, \tag{3.16}$$

where $\phi(\mathbf{x})$ denotes a fixed feature space, and b indicates a bias parameter. The sign of $y(\mathbf{x})$ indicates the class of input $\mathbf{x}$. We assume that the training features are linearly separable, i.e., there exists at least one choice of b that satisfies $y(\vec{\beta}_{mp}^{i}) \geq 0$ for features having $t_m = +1$ and $y(\vec{\beta}_{mp}^{i}) \leq 0$ for features having $t_m = -1$. SVM approaches this problem through the concept of the margin, which is defined to be the smallest distance between the decision boundary and any of the features (for an illustration, refer to Fig. 7.1 in [2]). To find the decision boundary, we need to maximize the margin, i.e., the perpendicular distance characterizing the feature-point that is closest to the decision boundary [2]. Thus, the maximum-margin solution is sought by solving (for further details, refer to [2], page 327):

$$argmax_{\mathbf{w},b} \left\{ \frac{1}{||\mathbf{w}||} min_m \left[t_m \left(\mathbf{w}^T \phi \left(\vec{\beta}_{mp}^{i} \right) + b \right) \right] \right\} \tag{3.17}$$

The direct solution to this optimization problem is quite challenging. However, one can resort to some assumptions and modifications so as to convert (3.17) into minimizing a quadratic function subject to a set of linear inequality constraints, which can be solved via a standard Lagrangian-multiplier method. Further details can be found in [2] (chapter 7).

We trained the LSVM classifier by providing the training-set features ($\vec{\beta}_{mp}^{i}$) and the cor-

responding ground-truth annotations t_m (Fig. 3.10 depicts an illustration). Then, the optimal

hyperplane is computed by solving (3.17), and is used as a decision boundary to classify new

(testing-subject) features into normal or abnormal segments.
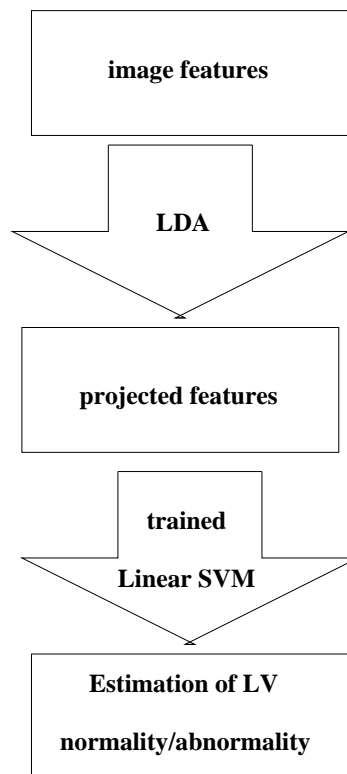
Figure 3.11: Overview of the testing phase.

3.6 Experiments

3.6.1 Data Acquisition:

The data contain 58×3 short-axis image datasets (i.e., apical, mid-cavity and basal), each consisting of 20 functional 2D images acquired from 21 normal and 37 abnormal hearts, using 1.5T MRI scanners with fast imaging employing steady state acquisition (FIESTA) mode. The details of the datasets are presented in Table. 3.1. The data consist of images from 41 male and 17 female subjects, and the average age of subjects is 52.3 ± 15.0 years. The temporal resolution (ΔT) is 45.1 ± 8.8 ms.

Table 3.1: Details of the datasets used in the evaluation of the proposed method.

Description	Value
Number of subjects	58
Scanner protocol	FIESTA
Patient ages	16 – 79 years
Short-axis image resolution	(256×256) or (512×512) pixels
Number of frames (K)	20
Temporal resolution (ΔT)	29 – 76 ms
Pixel spacing	($0.7 \times 0.7 \times 10.0$) – ($1.7 \times 1.7 \times 12.0$) mm
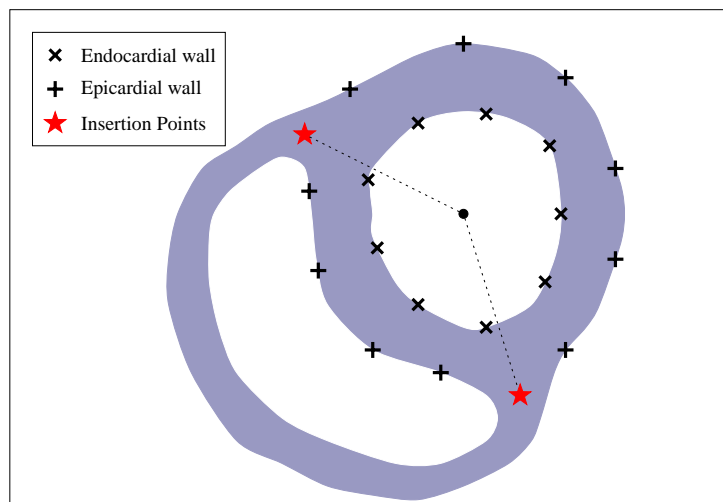
Figure 3.12: User input to specify initial segmentation and anatomical landmarks on the first frame.

For each subject, three slices were respectively chosen from apical, mid-cavity and basal frames, and *anatomical landmarks* were identified manually on the first frame[4] (see Fig. 4.3 for an illustration). A cubic spline interpolation was used to sample N points along each endo- and epi-cardial boundary. The higher the value of N, the better the estimation accuracy. However, the computational complexity of the algorithm increases with N. The apical, mid-cavity and basal slices were automatically partitioned, respectively, into 4, 6 and 6 segments following the standard in [2], which results in 16 segments per subject. The 17th segment, apex, was not analyzed.

The results of 928 myocardial segments (58 subjects $\times$ 16 segments) were compared with a single ground truth classification[5]. We classify a segment as abnormal if that segment is hypokinetic, akinetic or diskinetic. Among the 37 abnormal subjects, 12 were diagnosed with infarction, 10 with dilated cardiomyopathy and 15 with various heart diseases including resuscitated cardiac arrest, coronary artery occlusion, cardioembolic cerebrovascular accident and pseudo-aneurysm.

3.6.2 Linear Discriminant Analysis:

Figs. 3.13, 3.14 and 3.15 show the projected features $\vec{\beta_{mp}^i}$ obtained following the LDA transformation for apical, mid-cavity and basal segments. Fig. 3.13 demonstrates that the apical-segment transformation is more discriminative than those obtained for basal and mid-cavity segments, which can be explained by the fact that the image-distribution estimation within apical segments is not affected by the occurrences of papillary muscles in the blood pool.

---

[4]As suggested by [2], the attachment of the right ventricular wall to the LV is used to identify and separate the septum from the LV anterior and inferior free walls.

[5]Each myocardial segment was marked following a binary score, either normal or abnormal. The ground truth was built by three experienced radiologists, each of whom annotated a different portion of the data set. Among the 928 segments, 579 segments were marked as normal and 349 as abnormal.
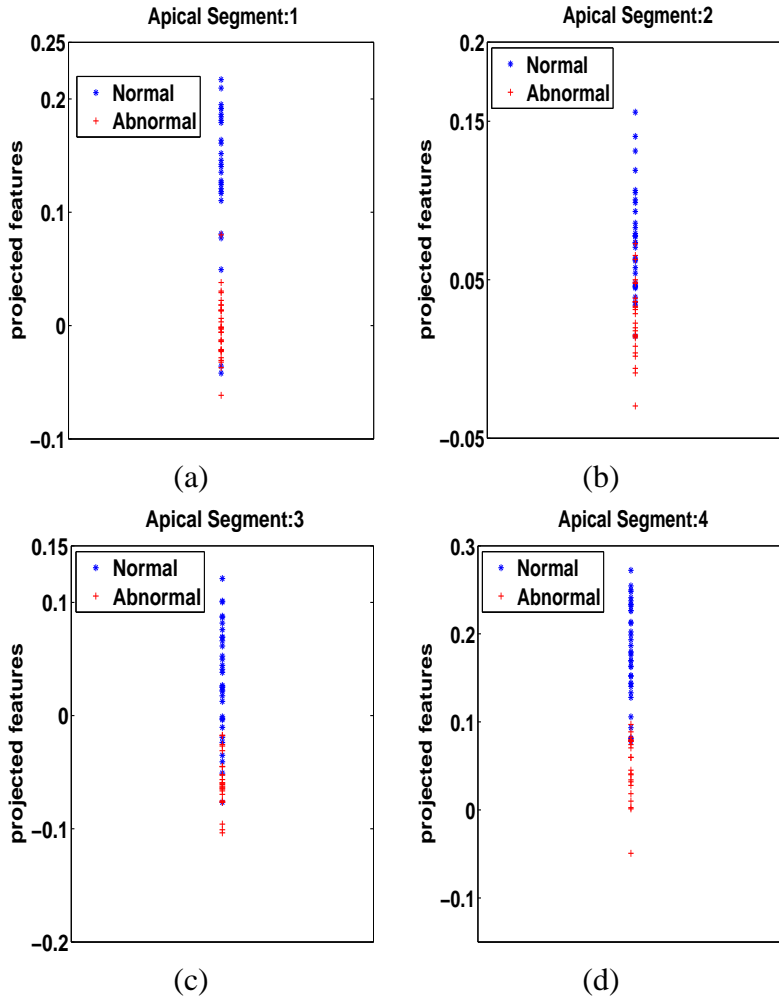
Figure 3.13: Projected apical features ($\vec{\beta_{mp}^i}$) obtained following the LDA transformation.

3.6.3 Linear SVM Classifier:

We used 16 LSVM classifiers, each assessing one of the 16 standard segments (normal/abnormal). Figs. 3.16, 3.17 and 3.18 show the decision boundaries that separate normal and abnormal classes. Fig. 3.16 depicts the projected features of four apical segments for each of the 58 subjects; the total number of apical segments is 232 (129 normal and 103 abnormal). Fig. 3.17 shows the projected features of a total number of 348 mid-cavity segments (209 normal and 139 abnormal); each of the 58 subjects has six mid-cavity segments. Fig 3.18 depicts the projected features of 348 basal segments (221 normal and 127 abnormal). The larger the distance between the support vectors of normal and abnormal classes, the more reliable the decision
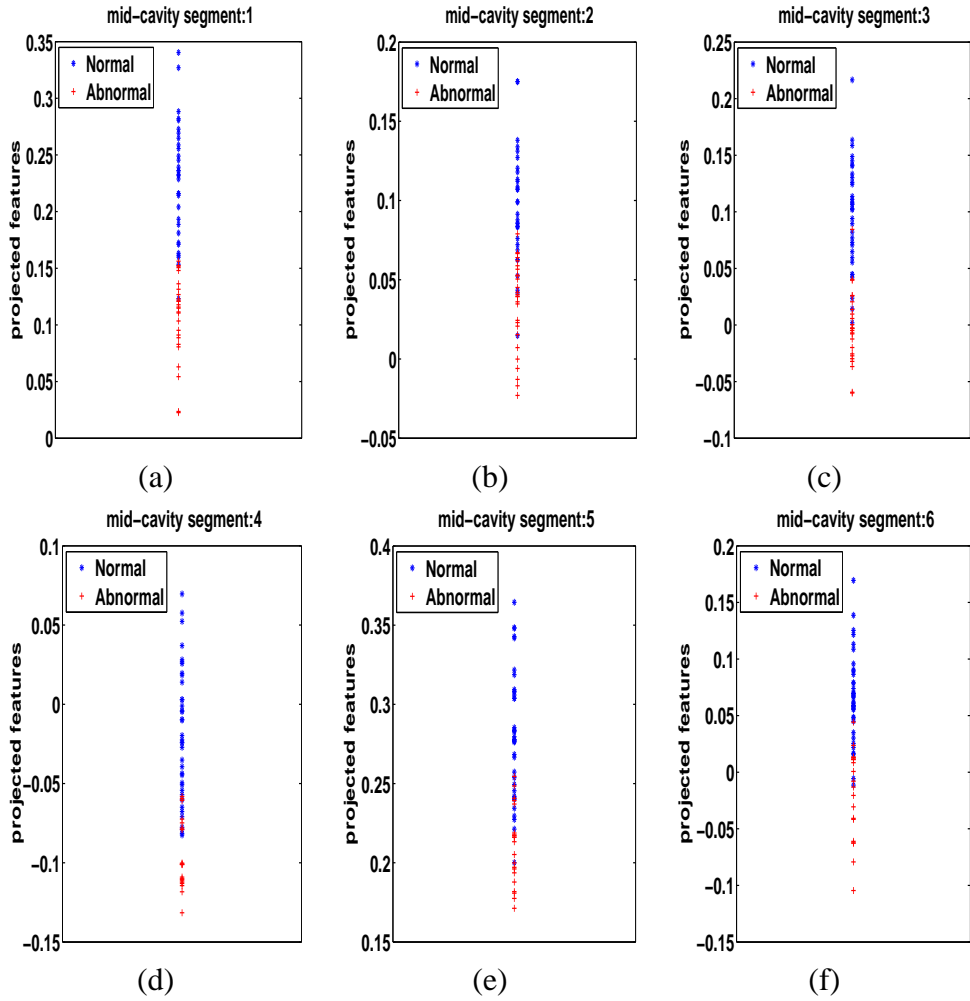
Figure 3.14: Projected mid-cavity features ($\vec{\beta_{mp}^{i}}$) obtained following the LDA transformation.

boundary. The decision boundary obtained for apical segments is more reliable than those obtained for mid-cavity and basal slices, which is expected, given the fact that the image features within the apical segments are not affected by the papillary muscles.

3.6.4 Classification Performance:

We used two criteria to measure the performance of each classifier: (1) the ROC (Receiver Operating Characteristic) curves with the corresponding AUCs (Area Under the Curve) and (2) the Bhattacharyya measure [3] to assess the discriminative power of the features. Furthermore, we assessed the classifier performance with a leave-one-third-of-the-subjects-out approach,
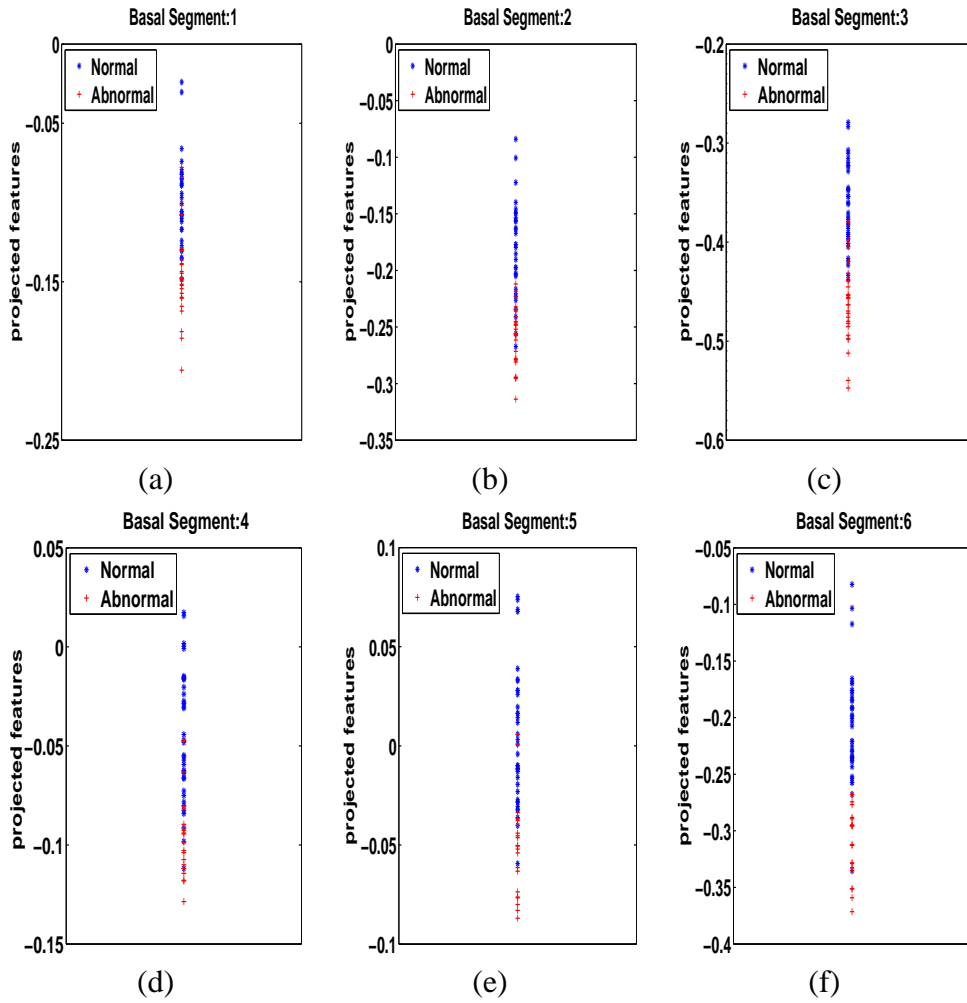
Figure 3.15: Projected basal features ($\vec{\beta_{mp}^i}$) obtained following the LDA transformation.

i.e., by training our algorithm using 2/3 of the dataset and testing on the remaining data.

ROC/AUC

The ROC curves depicted in Figs. 3.19, 3.20, 3.21 demonstrate the performances of the proposed method, with the best performance being obtained for apical segments. Table 3.2 reports the corresponding AUCs.
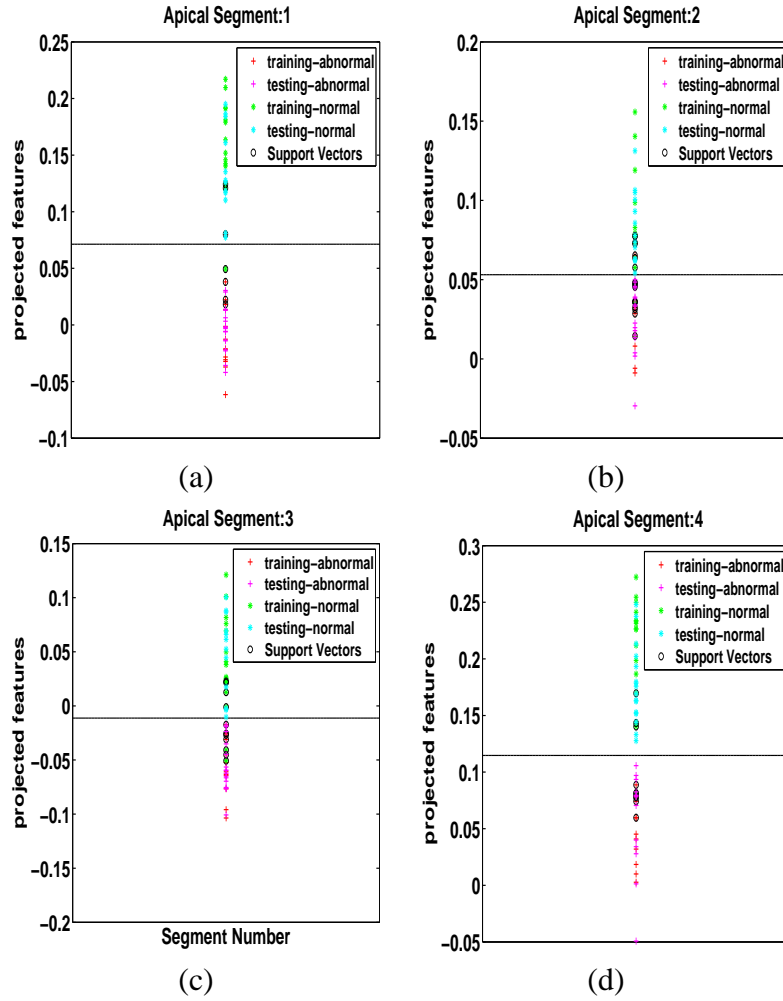
Figure 3.16: Decision boundaries and support vectors for the apical segments.

Bhattacharyya measure

We used the Bhattacharyya distance metric to evaluate the overlap between the distributions of features over normal and abnormal classes:

$$\mathcal{B} = \sqrt{1 - \sum \sqrt{f_N(y)f_A(y)}}, \tag{3.18}$$

where $f_N(y)$ and $f_A(y)$ are the distributions over normal and abnormal hearts, respectively. The higher $\mathcal{B}$, the more discriminative the classifier. The Bhattacharyya distances obtained in Table 3.2 are consistent with the ROC/AUC evaluations.
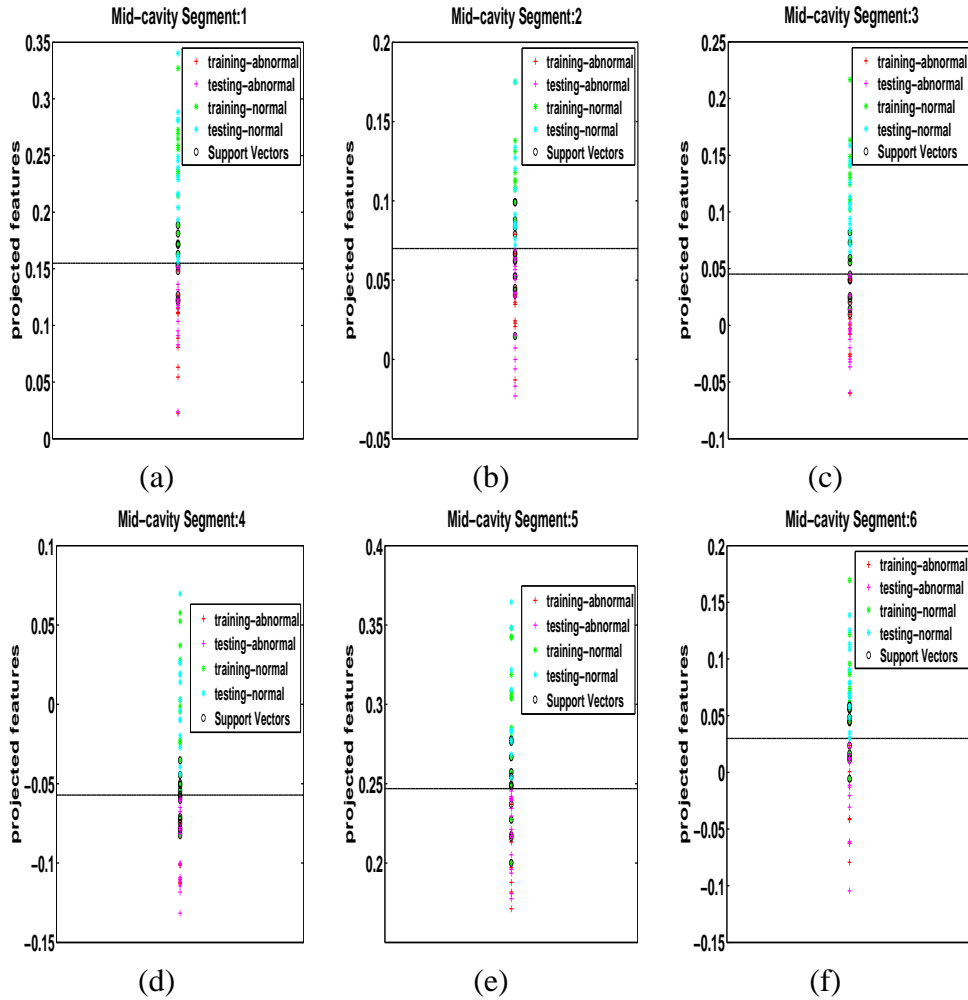
Figure 3.17: Decision boundaries and support vectors for the mid-cavity segments.

	AUC	Bhattacharyya distance metric ($\mathcal{B}$)
Apical	0.9571	0.7776
Mid-cavity	0.9368	0.6882
Basal	0.9152	0.6336

Table 3.2: The AUCs corresponding to Figs. 3.19, 3.20, 3.21 and the corresponding Bhattacharyya distance metrics ($\mathcal{B}$) of normal/abnormal distributions. The higher the values, the more discriminative the ability of the classifier.
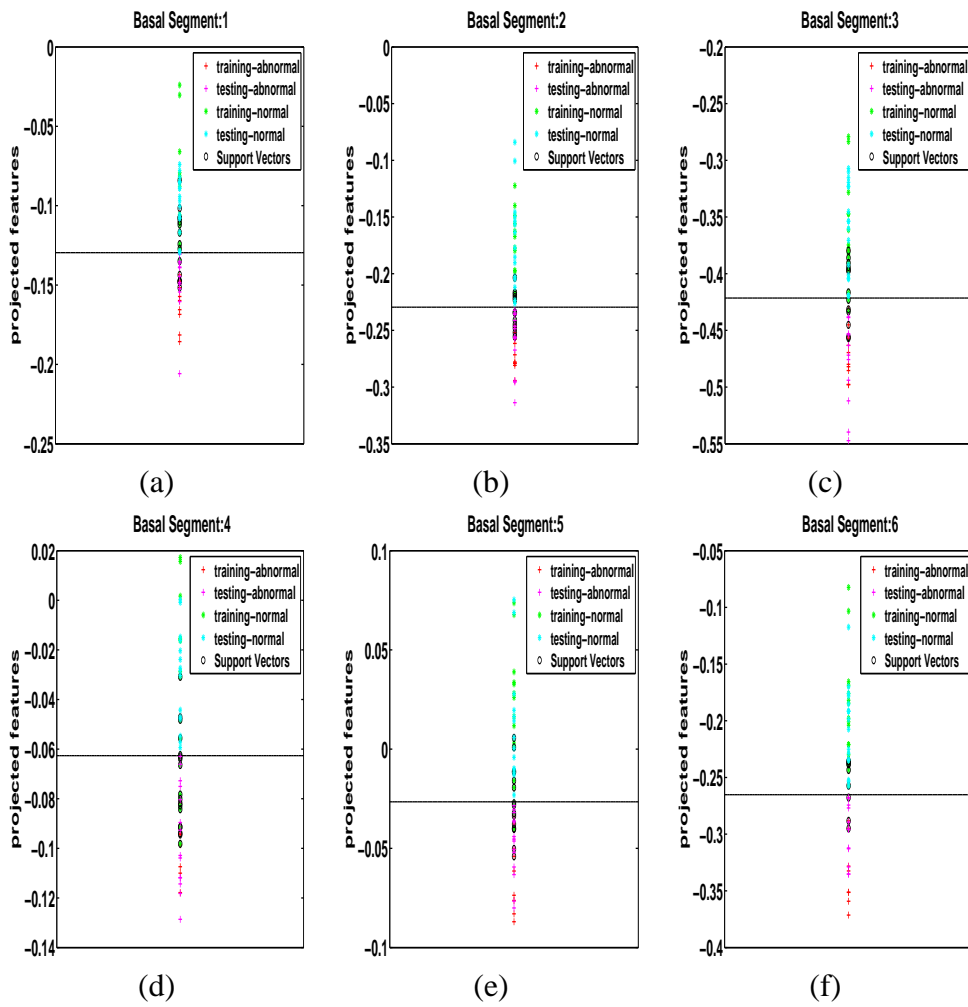
Figure 3.18: Decision boundaries and support vectors for the basal segments.
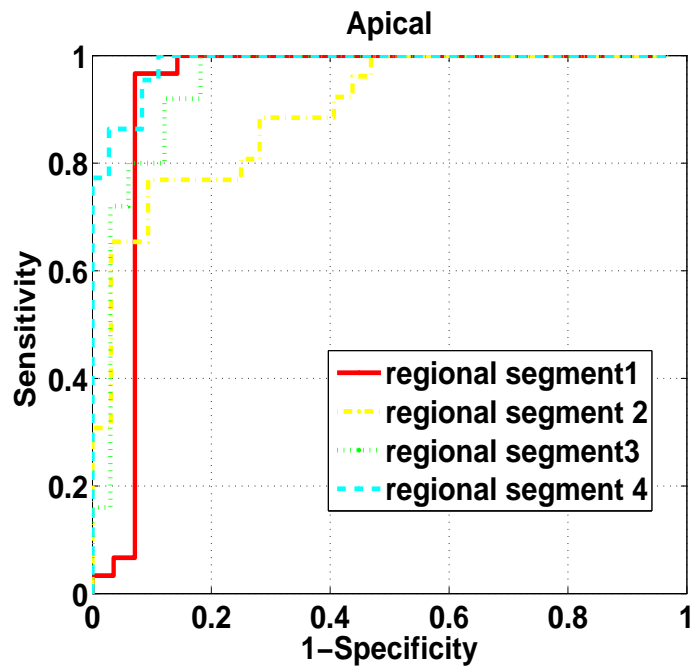
(a) Apical

Figure 3.19: ROCs for apical segments: The closer the curve to the left-hand top corner, the better the classification performance.
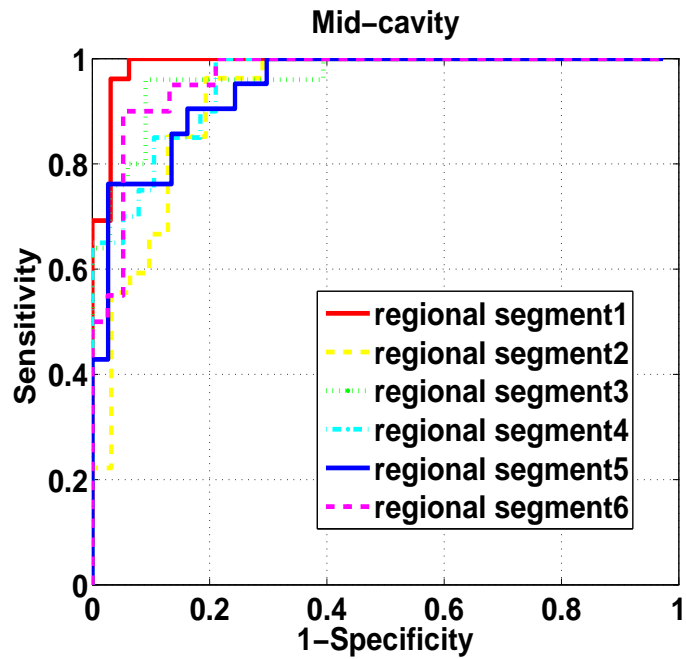
(b) Mid-cavity

Figure 3.20: ROCs for mid-cavity segments: The closer the curve to the left-hand top corner, the better the classification performance.
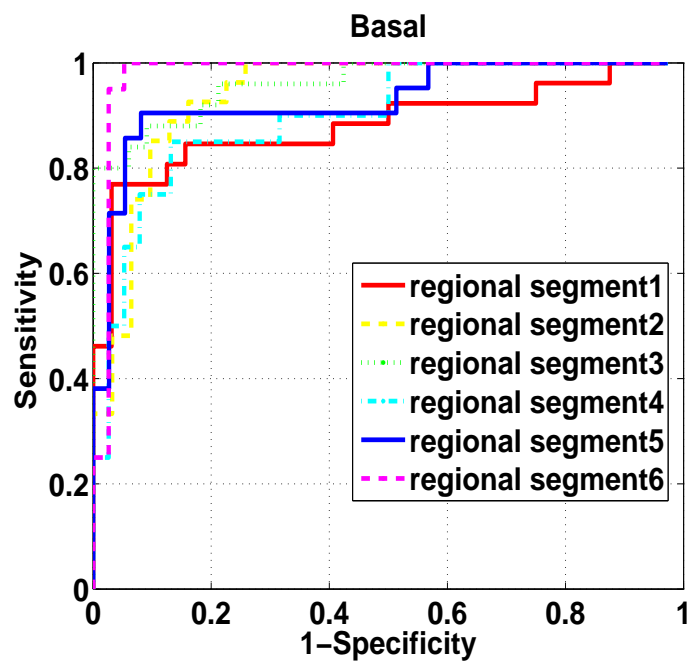
(c) Basal

Figure 3.21: ROCs for basal segments: The closer the curve to the left-hand top corner, the better the classification performance.

Classification Accuracy

We evaluated the classifier performance by computing the accuracy, specificity and sensitivity over all the datasets:

$$\text{accuracy} = \frac{T_P + T_N}{P + N}, \quad \text{specificity} = \frac{T_N}{N}, \quad \text{sensitivity} = \frac{T_P}{P} \qquad (3.19)$$

where T_P denote true positives (number of segments correctly classified as *"Abnormal"*), and T_N true negatives (number of segments correctly classified as *"Normal"*). The total number of *"Abnormal"* and *"Normal"* segments are P and N, respectively.

Table 3.3 reports an overall classification accuracy of 86.01%, with a sensitivity of 93.96% and a specificity of 81.82%. The highest performance was achieved for apical slices with 89.75% for accuracy, 94.10% for sensitivity, and 86.29% for specificity.

	Sensitivity (%)	Specificity (%)	Accuracy (%)
Apex	94.10	86.29	89.75
Mid-cavity	94.07	80.16	85.72
Base	93.72	78.45	84.02
Overall	93.96	81.82	86.09

Table 3.3: Classification accuracy using a leave-one-third-of-the-subjects-out approach. The proposed method achieved an overall classification accuracy of 86.09%.

	Visual assessment by radiologists		
	Abnormal detection	Normal detection	Total
The proposed method			
Abnormal detection	**348**	89	437
Normal detection	33	**458**	491
Total	381	547	928

Table 3.4: Comparisons between the proposed method and visual assessment scoring by experienced radiologists. The proposed method yielded a kappa measure of 0.73, a *substantial agreement* with radiologists' results.

Table 3.4 reports comparisons of the obtained results to visual scores by experienced radiologists. We computed the Kappa statistics [21] between the proposed method and radiologists'

findings as follows. The observed percentage agreement is:

$$p(a) = \frac{348 + 458}{928} = 0.87, \qquad (3.20)$$

while the overall probability of random agreement is:

$$p(e) = \frac{381}{928} \cdot \frac{437}{928} + \frac{547}{928} \cdot \frac{491}{928} = 0.51 \qquad (3.21)$$

Therefore, the Cohen's kappa is:

$$\kappa = \frac{p(a) - p(e)}{1 - p(e)} = 0.73, \qquad (3.22)$$

a value which indicates a substantial agreement [21] between the proposed method and visual scoring.

3.6.5 Comparison with other methods

Method	User-input/Reg	Accuracy	Time	Dataset	slice
Proposed method	mnl-first	0.86	real-time	58 subj cine MRI	A,B,M
Punithakumar *et.al.* [14]	mnl-first + Reg	0.87	62 sec	58 subj cine MRI	A,B,M
Suinesiaputra *et.al.* [19]	mnl-first + Reg	0.78	N/A	53 subj CE MRI	A,B,M
Garcia-Barnes *et.al.* [4]	mnl-first+Reg	0.85	N/A	28 subj Tagged MR	A,B,M
Suinesiaputra *et.al.* [21]	mnl-all	0.77	N/A	89 subj cine MRI	A,B,M
Lu *et.al.* [11]	mnl-all	0.86	N/A	17 subj cine MRI	B
Qian *et.al.* [15]	mnl-all	0.87	N/A	22 subj Tagged MR	A,B,M

Table 3.5: Comparisons of the proposed method with recent existing methods of regional myocardial abnormality detection. All the existing methods require either manual or automatic (registration-based) segmentations of several frames in a cardiac sequence.

Table. 3.5 compares the proposed method with several other recent methods with respect to the user-input/segmentation requirements, accuracy, processing time, size of the used data sets and types of the processed slices. In the second column, the acronym "manual-first" means that the corresponding method requires a manual segmentation of the first frame, and "manual-all" means that manual segmentations are required for all frames. Acronym "Reg" means that the

corresponding method requires an inter-frame registration process to find the LV boundaries in all the frames of a sequence. In the last column, A, B and M denote apical, basal and mid-cavity respectively. All the methods in Table. 3.5 analyze apical, basal and midcavity slices except the method proposed by Lu *et. al.* [11] which shows preliminary results only for basal slices.

User-inputs/Segmentations: The proposed method requires manual segmentation of a single frame as user input. On the contrary, Punithakumar *et. al.* [14] use a manual segmentation of the first frame, and propagate such a manual input via a registration algorithm to obtain the epicardial boundaries in all the remaining frames. Similarly, Suinesiaputra *et. al.* [19] use manual segmentations in end-diastolic and end-systolic frames followed by a registration algorithm to find the myocardium boundaries in the remaining frames. Garcia-Barnes *et. al.* [4] use manual segmentation of the first frame followed by a B-spline registration applied the the myocardium boundaries in all frames. Lu *et. al.* [11] show preliminary results for only basal slices; in this method, each of the epicardial boundaries is obtained from manual mouse clicks and spline interpolation. Similarly, the approaches in [21, 15] need manual segmentations of all the frames as user inputs.

Accuracy/speed: The meta-analysis of accuracy in table 3.5 shows that the proposed method can yield a competitive performance while reducing significantly the computational load and user efforts.

3.7 Conclusions

We proposed a real-time machine-learning and image-statistic based approach to automating the detection and localization of segmental (regional) myocardial abnormalities in MRI. Unlike the existing techniques, the proposed method did not require delineations of the endo- and/or epi-cardial boundaries in all the frames of a cardiac sequence. Starting from a minimum user input in only one frame in a subject image, for all the regional segments and all subsequent frames we built a set of statistical MRI features based on the Bhattacharyya measure of similarity between distributions. We demonstrated via synthetic and real examples that, over a cardiac cycle, such statistical features are related to the proportion of blood within each segment. Therefore, they can characterize segmental contraction with significantly less computation and user input. We sought the optimal direction along which the proposed image features are most descriptive via a Linear Discriminant Analysis. Then, using the LDA results as inputs to a Linear Support Vector Machine classifier, we obtained an abnormality assessment of each of the standard cardiac segments in real-time. We reported a comprehensive experimental evaluation of the proposed algorithm over 928 cardiac segments obtained from 58 subjects. Compared against ground-truth evaluations by experienced radiologists, the proposed algorithm yielded an overall classification accuracy of 86.09% and a kappa measure of 0.73. We further reported meta-analysis comparisons with several recent methods, which showed that the proposed method can yield a competitive performance while significantly reducing the computational load and user efforts.

References

[1] I. Ben Ayed, S. Li, and I. Ross, "A statistical overlap prior for variational image segmentation," *International Journal of Computer Vision*, vol. 85, no. 1, pp. 115–132, 2009.

[2] C. M. Bishop, *Pattern Recognition and Machine Learning*. Springer-Verlag, 2006.

[3] M. D. Cerqueira, N. J. Weissman, V. Dilsizian, A. K. Jacobs, S. Kaul, W. K. Laskey, D. J. Pennell, J. A. Rumberger, T. Ryan, and M. Verani, "Standardized myocardial segmentation and nomenclature for tomographic imaging of the heart: A statement for healthcare professionals from the cardiac imaging committee of the council on clinical cardiologyof the American Heart Association," *Circulation*, vol. 105, no. 4, pp. 539–542, 2002.

[4] D. Comaniciu, V. Ramesh, and P. Meer, "Kernel-based object tracking," *IEEE Trans. Pattern Analysis and Machine Intelligence*, vol. 25, no. 5, pp. 564–577, 2003.

[5] J. Garcia-Barnes, D. Gil, L. Badiella, A. Hernàndez-Sabaté, F. Carreras, S. Pujadas, and E. Martí, "A normalized framework for the design of feature spaces assessing the left ventricular function," *IEEE Transaction on Medical Imaging*, vol. 29, no. 3, pp. 733–745, 2010.

[6] H.-C. Kim, D. Kim, and S. Y. Bang, "Face recognition using LDA mixture model," *Pattern Recognition Letter*, vol. 24, pp. 2815–2821, 2003.

[7] K. Y. Leung and J. G. Bosch, "Localized shape variations for classifying wall motion in echocardiograms," in *Medical Image Computing and Computer-Assisted Intervention; MICCAI*, vol. 4791, 2007, pp. 52–59.

[8] G.-C. Lin, W.-J. Wang, C.-M. Wang, and S.-Y. Sun, "Automated classification of multispectral MR images using linear discriminant analysis," *Computerized Medical Imaging and Graphics*, vol. 34, pp. 251–268, 2010.

[9] Y.-H. Liu, H.-P. Huang, and C.-H. Weng, "Recognition of electromyographic signals using cascaded kernel learning machine," *IEEE-ASME Transactions on Mechatronics*, vol. 12, pp. 253–264, 2007.

[10] Y. Lu, P. Radau, K. Connelly, A. Dick, and G. Wright, "Pattern recognition of abnormal left ventricle wall motion in cardiac MR," in *Medical Image Computing and Computer-Assisted Intervention; MICCAI*, vol. 5762, 2009, pp. 750–758.

[11] S. Mansor and J. Noble, "Local wall motion classification of stress echocardiography using a hidden Markov model approach," *International Symposium on Biomedical Imaging (ISBI) : From Nano to Macro*, vol. 1, pp. 1295–1298, 2008.

[12] G. Mercier and M. Lennon, "Support vector machines for hyperspectral image classification with spectral-based kernels methods," *IEEE International Geoscience and Remote Sensing Symposium*, vol. 1, pp. 288–290, 2003.

[13] O. Michailovich, R. Yogesh, and A. Tannenbaum, "Image segmentation using active contours driven by the bhattacharyya gradient flow," *IEEE Transaction on Image Processing*, vol. 16, no. 11, pp. 2787–2801, 2007.

[14] K. Polat and S. Günes, "A novel approach to estimation of E. coli promoter gene sequences: Combining feature selection and least square support vector machine," *Applied Mathematics and Computation*, vol. 190, no. 2, pp. 1574–1582, 2007.

[15] K. Polat, S. Güneş, and A. Arslan, "A cascade learning system for classification of diabetes disease: Generalized discriminant analysis and least square support vector machine," *Expert System with Applications*, vol. 34, pp. 482–487, 2008.

[16] K. Punithakumar, I. Ben Ayed, A. Islam, I. Ross, and S. Li, "Regional heart motion abnormality detection via information measures and unscented kalman filtering," in *Medical Image Computing and Computer-Assisted Intervention; MICCAI*, vol. 6361, 2010, pp. 409–417.

[17] Z. Qian, Q. Liu, D. N. Metaxas, and L. Axel, "Identifying regional cardiac abnormalities from myocardial strainsusing spatio-temporal tensor analysis," in *Medical Image Computing and Computer-Assisted Intervention; MICCAI*, vol. 5241, 2008, pp. 789–797.

[18] A. Suinesiaputra, A. Frangi, T. Kaandorp, H. Lamb, J. Bax, J. Reiber, and B. Lelieveldt, "Automated detection of regional wall motion abnormalities based on a statistical model applied to multislice short-axis cardiac MR images," *IEEE Transactions on Medical Imaging*, vol. 28, no. 4, pp. 595–607, 2009.

[19] A. Suinesiaputra, A. F. Frangi, T. A. Kaandorp, H. J. Lamb, J. J. Bax, J. H. Reiber, and B. P. Lelieveldt, "Automated regional wall motion abnormality detection by combining rest and stress cardiac MRI: Correlation with contrast-enhanced MRI," *Journal of Magnetic Resonance Imaging*, vol. 34, no. 2, pp. 270–278, 2011.

[20] H. Sundar, C. Davatzikos, and G. Biros, "Biomechanically-constrained 4D estimation of myocardial motion," in *Medical Image Computing and Computer-Assisted Intervention; MICCAI*, vol. 5762, 2009, pp. 257–265.

[21] A. J. Viera and J. M. Garret, "Understanding interobserver agreement: the kappa statistic." *Family Medicine*, vol. 37, no. 5, pp. 360–363, 2005.

[22] P. Xu, G. N. Brock, and R. S. Parrish, "Modified linear discriminant analysis approaches for classification of high-dimensional microarray data," *Computational Statistics and Data Analysis*, vol. 53, pp. 1674–1687, 2009.

[23] J. Ye, R. Janardan, Q. Li, and H. Park, "Feature reduction via generalized uncorrelated linear discriminant analysis," *IEEE Transaction on Knowledge and Data Engineering*, vol. 18, pp. 1312–1322, 2006.

[24] Y.-C. Yeh, W.-J. Wang, and C. W. Chiou, "Cardiac arrhythmia diagnosis method using linear discriminant analysis on ECG signals," *Measurement*, vol. 42, pp. 778–789, 2009.

Chapter 4

Multi-Class Segmental Cardiac Dysfunction Classification

4.1 Multi-Class Segmental Cardiac Dysfunction Classification via Statistical MRI Features

Automatic detection of regional cardiac abnormality has recently sparked an impressive research effort as discussed in chapter 1. Furthermore, most of existing methods require delineations of the endo- and/or epi-cardial boundaries in all the frames of a cardiac sequence. Former investigation of regional abnormality detection used echocardiography [3, 9, 12], using different techniques including shape statistics [3, 9] or hidden Markov models [12]. Recently, MRI modality based techniques have been used as ground-truths for cardiac regional assessment and therefore have attracted research attention [15, 11, 21, 4, 10, 14]. Cardiac MR imaging has great potential for diagnosis of the LV function as examination is not limited by an acoustic window, and cardiac MR imaging allows an exhaustive myocardial evaluation

---

[1]This chapter is based on the paper:

1) Afshin, M., Ben Ayed, I., Islam, A., Goela, A., Ross, I., Peters, T., Li, S., "Automatic Diagnosis of Segmental Cardiac Dysfunction via Statistical Features in Short-axis MRI ", under revision in IEEE Transaction on Biomedical Engineering.

with excellent spatial resolution [4]. As discussed in section 1.7.1, all existing algorithms addressed a *binary* classification problem, where each cardiac segment is characterized as normal or abnormal.

The purpose of this study is to investigate more the general problem, where each regional segment is classified into one of four classes: (1) *normal* (2) *hypokinetic* (3) *akinetic* and (4) *dyskinetic*. Starting from a simple user input in only one frame in the sequence, we build a set of statistical MRI features based on a measure of similarity between distributions for all the regional segments and all subsequent frames. We demonstrate that over a cardiac cycle, the statistical features are related to the blood and myocardium proportion within each segment, and can therefore characterize segmental cavity/myocardium contraction without the need for LV segmentation in all the frames. We use these features as inputs for multi-class Support Vector Machine (SVM) classifier, and obtain a 4-class assessment of each segment. We report a comprehensive experimental evaluation of the proposed algorithm over 928 cardiac segments obtained from 58 subjects. These results are compared to ground-truth labels obtained by experienced radiologists with an overall 4-class accuracy of 74.14%.

4.2 Methods

The proposed method consists of three main steps:

- Identifying 16 regional segments in one single frame, using user-provided inner and outer LV boundaries.

- Computing image statistics as input features to a multi-class SVM classifier for each of the 16 segments of a given subject.

- Classifying regional segments into 4 classes: (1) normal; (2) hypokinetic; (3) akinetic; and (4) dyskinetic.

4.2.1 Identifying 16 Segments in Only One Frame:

This step constructs the regional segments following the regulations that have already been discussed in section 3.2.

4.2.2 Building Segmental Statistical Features from MRI Images

We propose to use image statistics as input features for the diagnosis of regional myocardial segment dysfunction.

Let $\mathcal{I}$ be a cardiac MRI sequence containing J frames[1], each comprising S slices[2] $\mathcal{I}_{s,j}$: $\Omega \subset \mathbb{R}^2 \to \mathbb{R}^+$ with $(s, j) \in [1 \ldots S] \times [1 \ldots J]$.

For each frame, we have I regional segments [3] $\mathcal{K}_{i,j}, (i, j) \in [1 \ldots I] \times [1 \ldots J]$.

Consider the following definitions and notations:

- **I** is the reference frame, which consists of 3 reference images, $\mathbf{I}_s$, each associated with a different slice level (apical, basal, and mid-cavity).

---

[1] J is typically equal to 20 -25.
[2] S is typically equal to 10.
[3] The number of segments per subject (I) is equal to 16.

110

- Let Γ_{in}^s and Γ_{out}^s denote the endo- and epi-cardial boundaries in $\mathbf{I}_s$ respectively (refer to Fig. 4.2.b).

- Let $\Gamma^i : [0,1] \to \Omega$ denote the boundary of segment i. (refer to Fig. 4.2.c).

Now, let us systematically superimpose segment boundary Γ^i onto the remaining frames as shown in Fig. 4.1 (b-d), and compute the corresponding image statistics. Here, we describe the method in detail for one mid-cavity segment (Fig. 5). However, the procedure is the same for all the others.

| (a) | (b): frame1 | (c): frame7 | (d): frame19 |
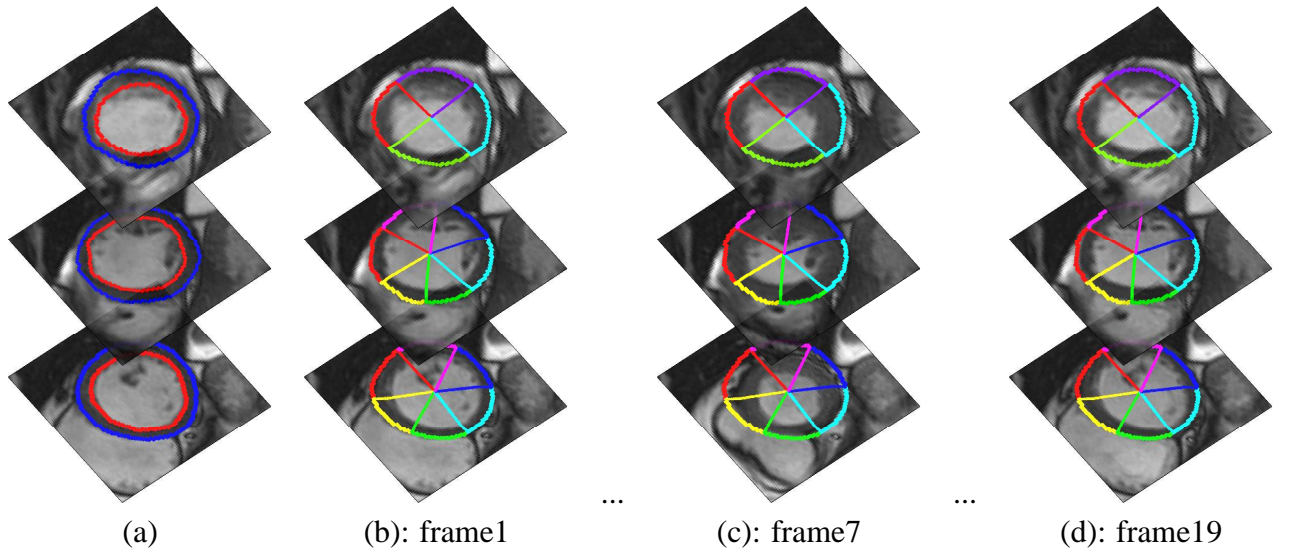
Figure 4.1: Identifying 16 regional segments in the reference frame. (a): user-provided segmentation of the reference frame. (b): 16 regional segments of the reference frame. (c-d): regional segments of the reference frame superimposed systematically to the rest of the frames.

Let $\mathbf{R}_\Gamma \subset \Omega$ be the region within Γ, $\Gamma \in \{\Gamma_{in}^s, \Gamma_{out}^s, \Gamma^i\}$, and $P_{\mathbf{R}_\Gamma,A}$ the kernel density estimate of the distribution of an image $A \in \mathcal{I}_{s,j}$ within region $\mathbf{R}_\Gamma$ [1]:

$$P_{\mathbf{R}_\Gamma,A}(z) = \frac{\int_{\mathbf{R}_\Gamma} K(z - A(x))dx}{a_{\mathbf{R}_\Gamma}}, \tag{4.1}$$

with K the Gaussian Kernel:

$$K(y) = \frac{1}{\sqrt{2\pi\sigma^2}} exp^{-\frac{y^2}{2\sigma^2}}, \tag{4.2}$$

111
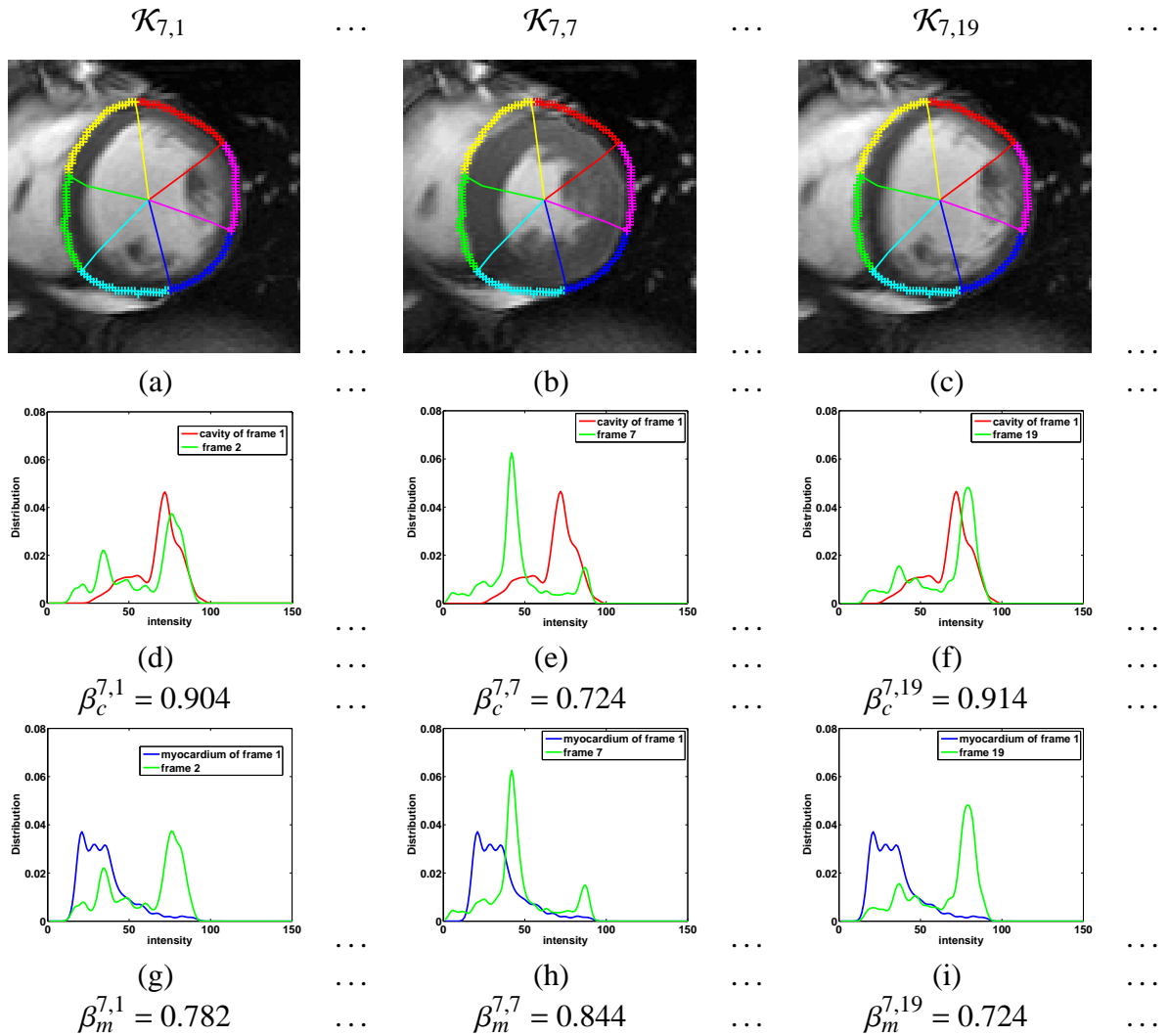
Figure 4.2: (a-c): mid-cavity regional segments superimposed on subsequent frames. (d-f): the similarity measures between the cavity region in the first frame and the regional segments in all other frames. (g-i): the similarity measures between the myocardium region in the first frame and regional segments in all other frames.

and $a_{\mathbf{R}}$ the area of region $\mathbf{R}$:

$$a_{\mathbf{R}} = \int_{\mathbf{R}} dx \tag{4.3}$$

We assume the following:

- The reference-image distribution within the region inside Γ_{in}^s ($P_{\mathbf{R}_{\Gamma_{in}^s}, \mathbf{I}_s}$) approximates the cavity distribution;

112
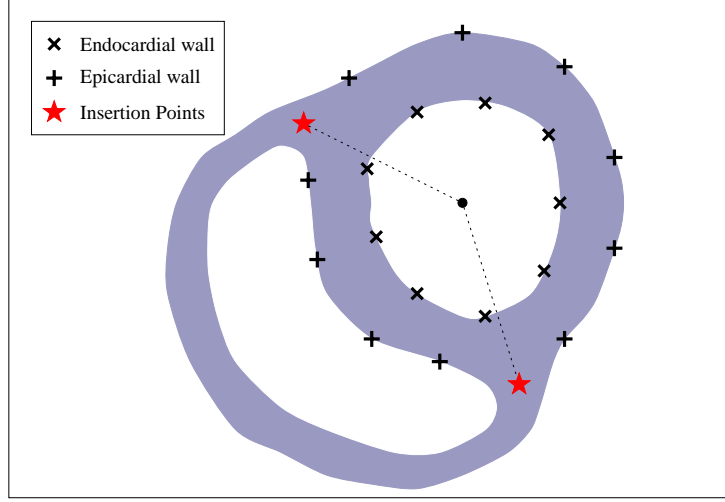
Figure 4.3: User input to specify initial segmentation and anatomical landmarks on the first frame.

- The reference-image distribution of the region between Γ_{in}^s and Γ_{out}^s ($P_{\mathbf{R}_{\Gamma_{btwn}^s},\mathbf{I}_s}$ s.t. $\mathbf{R}_{\Gamma^s{}_{btwn}} = \mathbf{R}_{\Gamma_{out}^s} - \mathbf{R}_{\Gamma_{in}^s}$) approximates the myocardium distribution.

Now, as features for each regional segment $\mathcal{K}_{i,j}$, we consider the following similarity measures between the distribution of the $j-th$ frame ($\mathcal{I}_{s,j}$) within the segment and the cavity/myocardium distributions:

$$\beta_c^{i,j} = \mathbf{B}(P_{\mathbf{R}_{\Gamma_{in}^s},\mathbf{I}_s}, P_{\mathbf{R}_{\Gamma^i},\mathcal{I}_{s,j}}), \tag{4.4}$$

$$\beta_m^{i,j} = \mathbf{B}(P_{\mathbf{R}_{\Gamma_{btwn}^s},\mathbf{I}_s}, P_{\mathbf{R}_{\Gamma^i},\mathcal{I}_{s,j}}), \tag{4.5}$$

where:

$$\mathbf{B}(f,g) = \int_{\mathbb{R}^+} \sqrt{f(z)g(z)}dz, \tag{4.6}$$

$\mathbf{B}$ is the Bhattacharyya coefficient [14] whose range is $[0,1]$, with 0 indicating no overlap between the distributions and 1 indicating a perfect match.

Features $\beta_c^{i,j}$ and $\beta_m^{i,j}$ are related to the proportion of blood and myocardium within regional segment $\mathcal{K}_{i,j}$. We illustrate such a relationship experimentally by the typical example pro-

vided by Fig. 5, which shows that the more overlap between the distributions of the cavity (or myocardium) and regional segment $\mathcal{K}_{i,j}$, the larger the proportion of blood (or myocardium) within the segment. Therefore, we anticipate that over a cardiac cycle, the set of features $\beta_c^{i,j}$ and $\beta_m^{i,j}$, $j \in [1 \ldots J]$, can characterize segmental cavity/myocardium contraction. Another way to see how features $\beta_c^{i,j}$ and $\beta_m^{i,j}$ can describe segmental function is to consider the extreme case where the regional myocardium does not move. In such case, the proportions of blood and myocardium are constant over a cardiac cycle, and so are the features.

4.2.3 Assessment of Regional Segment Dysfunction Using Multi-Class Support Vector Machine

We used the well-known one-versus-all multi-class SVM [6, 13, 10, 16, 15, 2] to classify each regional segment $i, i \in [1 \ldots I]$, into four classes:

1. normal

2. hypokinetic

3. akinetic

4. dyskinetic.

For each segment i, the input of the SVM classifier is a feature vector of the form $v^i = [u_c^i; u_m^i]$, where u_c^i and u_m^i are two J-dimensional row matrices containing the Bhattacharrya statistics: $u_c^i = \left\{ \beta_c^{i,j} \right\}$ and $u_m^i = \left\{ \beta_m^{i,j} \right\}$. The output is a label $l \in \{1, 2, 3, 4\}$, which corresponds to one of the four classes. In the training phase, we proceeded to a leave one-subject-out approach. We used the standard parameters of the multi-class SVM [6], and a radial-basis function as a kernel type.

4.3 Results and Discussion

4.3.1 Data Acquisition

The data comprise 58×3 short-axis image datasets (i.e., apical, mid-cavity and basal), each consisting of 20 functional 2D images acquired from 21 normal and 37 abnormal hearts, acquired on a 1.5T MRI scanners with fast imaging employing steady state acquisition (FIESTA) mode. The details of the datasets are presented in Table. 3.1. The data consists of images from 41 male and 17 female subjects, and the average age of subjects is 52.3 ± 15.0 years. The temporal resolution (ΔT) is equal to 45.1 ± 8.8 ms.

For each subject, three slices were respectively chosen from apical, mid-cavity and basal frames, and *anatomical landmarks* were identified manually on the first frame[4](refer to Fig. 4.3). The apical, mid-cavity and basal slices were automatically partitioned, into 4, 6 and 6 segments respectively, following the AHA standard [2], which results in 16 segments per subject. The 17th segment, apex, was not analyzed.

The results of 928 myocardial segments (58 subjects × 16 segments) were compared with a single ground truth classification. The ground truth was built by three experienced radiologists, each of whom annotated a different portion of the data set. Among the 928 segments, 537 segments were marked as normal, 283 segments were marked as hypokinetic, 73 segments as akinetic and 25 as diskinetic. Among the 37 abnormal subjects, 12 were diagnosed with infarction, 10 with dilated cardiomyopathy and 15 with various heart diseases including resuscitated cardiac arrest, coronary artery occlusion, cardioembolic cerebrovascular accident and pseudo-aneurysm.

---

[4]As suggested by [2], the attachment of the right ventricular wall to the LV is used to identify and separate the septum from the LV anterior and inferior free walls.
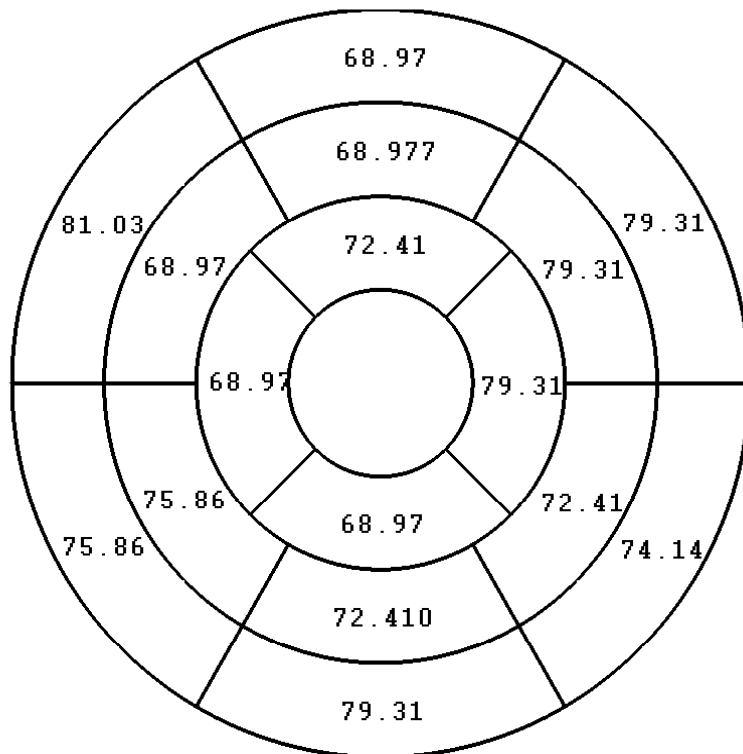
Figure 4.4: Accuracy(%) for each of the 16 regional segments. The average accuracy over all 16 segments is equal to 74.14%.

4.3.2 Classification Performance

We assessed the performance of the proposed algorithm with three criteria: the accuracy, confusion matrix, and bull's eye plot.

Accuracy

The accuracy for segment i is the number of cases classified correctly divided by total number of the cases. Fig. 4.4 reports the accuracy for each of the 16 segments (The display follows the bull's eye standard plot of the AHA [2]). The average accuracy over all 16 segments is equal to 74.14%.

The clinical study in [5] showed a very high inter-observer variability for multi-class assessments of regional segments. For instance, Table.2. in this paper shows the assessments of 3 radiologists, each compared to a panel ground-truth obtained by an independent consensus.

The lowest radiologist performance is 55% and the highest is 86%, indicating a substantial inter-observer difference of 24%. Therefore, the problem is really challenging, and we believe an algorithm performance of 74% is an acceptable rate because the inter-observer variability can be as high as 24%.

Confusion Matrix

Table 4.1 reports the confusion matrices for basal, midcavity, and apical segments. The diagonal elements indicate the number of segments that were classified correctly, whereas those on the off-diagonal indicate the number of mis-classified segments along with the corresponding incorrect classes. Among 348 basal segments, 266 were classified correctly (76.4%); among 348 midcavity segments, 254 were classified correctly (73.0%); and among 232 apical segments, 168 were classified correctly (72.4%).

		Predicted Condition			
		normal	hypokinesia	akinesia	dyskinesia
Basal ground-truth	normal	193	15	1	0
	hypokinesia	35	68	1	0
	akinesia	9	12	5	0
	dyskinesia	4	4	1	0
Mid-cavity ground-truth	normal	188	21	0	0
	hypokinesia	42	62	0	0
	akinesia	7	15	4	0
	dyskinesia	4	5	0	0
Apical ground-truth	normal	110	19	0	0
	hypokinesia	23	52	0	0
	akinesia	2	14	5	0
	dyskinesia	2	3	1	1

Table 4.1: Confusion matrix

Bull's eye Plots:

Fig. 4.5 shows the results for 14 randomly selected subjects. The colours depict the four classes: red for normal, green for hypokinetic, yellow for akinetic and white for dyskinetic. Note that normal and hypokinetic conditions are detected in most of the cases whereas the

dyskinetic conditions are missed, which can be explained by the small proportion of dyskinetic

segments in our training data.
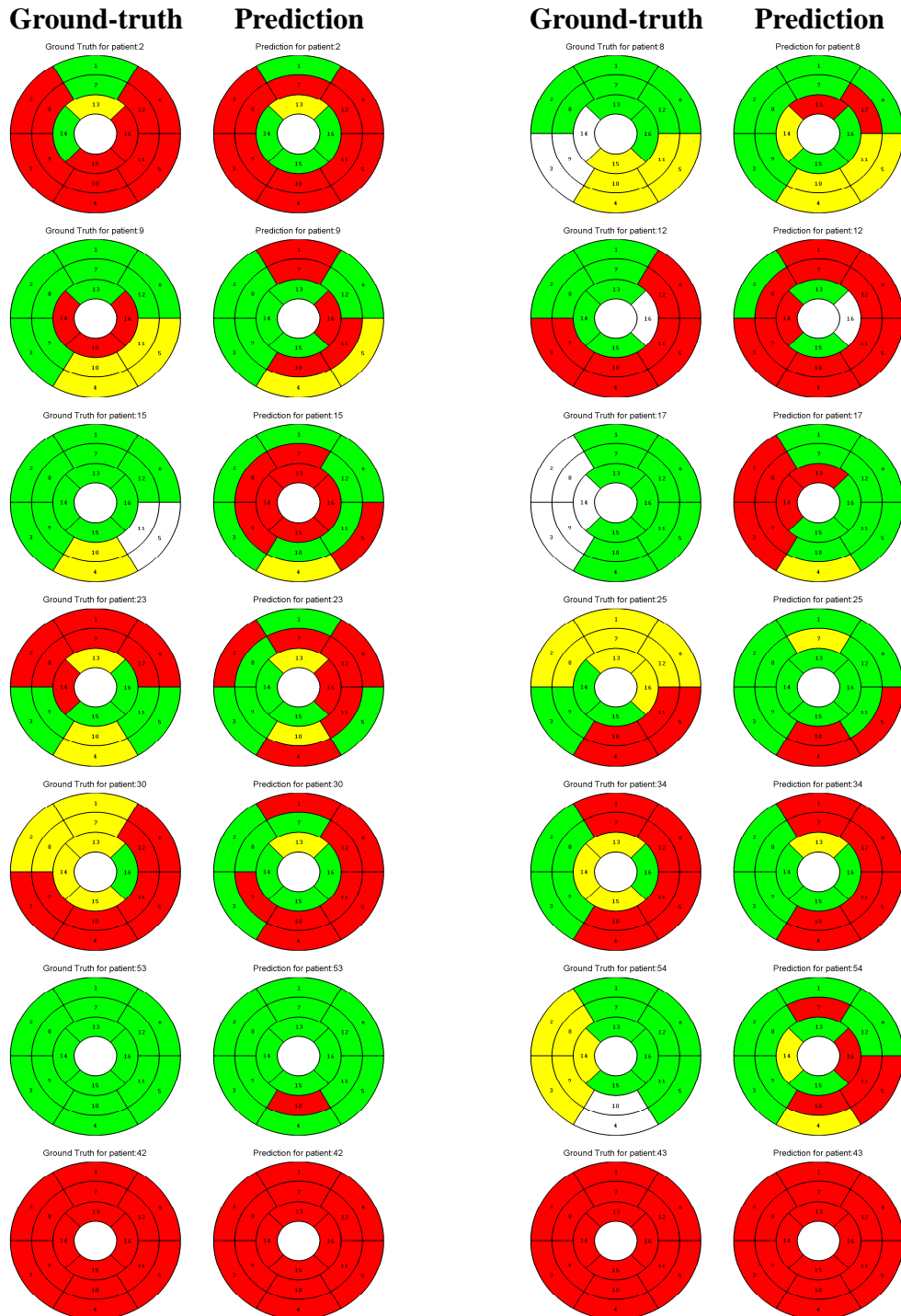
Figure 4.5: Bull's eye plot obtained from ground-truth in column 1,3. The colors depict the four classes: red for normal, green for hypokinetic, yellow for akinetic and white for dyskinetic.

4.4 Conclusion

This study investigated classifying regional cardiac segments into one of four classes: (1) normal; (2) hypokinetic; (3) akinetic; and (4) dyskinetic. Starting from a minimum user input in only one frame in a cardiac sequence, we built for all the regional segments and all subsequent frames a set of statistical MRI features which can characterize segmental cavity/myocardium contraction without the need for delineating the LV boundaries in all the frames. Using these features as inputs to a multi-class support vector machine (SVM) classifier, we obtained a 4-class assessment of each segment. A comprehensive experimental evaluation over 928 cardiac segments obtained from 58 subjects showed a very promising performance of the algorithm, with an overall 4-class accuracy of 74.14%.

References

[1] I. Ben Ayed, S. Li, and I. Ross, "A statistical overlap prior for variational image segmentation," *International Journal of Computer Vision*, vol. 85, no. 1, pp. 115–132, 2009.

[2] C. M. Bishop, *Pattern Recognition and Machine Learning*, 1st ed. Springer-Verlag, 2006.

[3] J. G. Bosch, F. Nijland, S. C. Mitchell, B. P. Lelieveldt, O. Kamp, J. H. Reiber, and M. Sonka, "Computer-aided diagnosis via model-based shape analysis: Automated classification of wall motion abnormalities in echocardiograms," *Academic Radiology*, vol. 12, no. 3, pp. 358 – 367, 2005.

[4] J. Caudron, J. Fares, F. Bauer, and J.-N. Dacher, "Evaluation of left ventricular diastolic function with cardiac MR imaging," *Radio Graphics*, vol. 31, pp. 239–259, 2011.

[5] M. D. Cerqueira, N. J. Weissman, V. Dilsizian, A. K. Jacobs, S. Kaul, W. K. Laskey, D. J. Pennell, J. A. Rumberger, T. Ryan, and M. Verani, "Standardized myocardial segmentation and nomenclature for tomographic imaging of the heart: A statement for healthcare professionals from the cardiac imaging committee of the council on clinical cardiologyof the American Heart Association," *Circulation*, vol. 105, no. 4, pp. 539–542, 2002.

[6] C.-C. Chang and C.-J. Lin, *LIBSVM : a library for support vector machines. ACM Transactions on Intelligent Systems and Technology, 2:27:1–27:27*, 2011.

[7] J. Garcia-Barnes, D. Gil, L. Badiella, A. Hernàndez-Sabaté, F. Carreras, S. Pujadas, and E. Martí, "A normalized framework for the design of feature spaces assessing the left ventricular function," *IEEE Transaction on Medical Imaging*, vol. 29, no. 3, pp. 733–745, 2010.

[8] K. Lekadir, N. Keenan, D. Pennell, and G. Yang, "An inter-landmark approach to 4-D shape extraction and interpretation: Application to myocardial motion assessment in MRI," *IEEE Transactions on Medical Imaging*, vol. 30, no. 1, pp. 52 –68, 2011.

[9] K. Y. Leung and J. G. Bosch, "Localized shape variations for classifying wall motion in echocardiograms," in *Medical Image Computing and Computer-Assisted Intervention; MICCAI*, vol. 4791, 2007, pp. 52–59.

[10] Y.-H. Liu, H.-P. Huang, and C.-H. Weng, "Recognition of electromyographic signals using cascaded kernel learning machine," *IEEE-ASME Transactions on Mechatronics*, vol. 12, pp. 253–264, 2007.

[11] Y. Lu, P. Radau, K. Connelly, A. Dick, and G. Wright, "Pattern recognition of abnormal left ventricle wall motion in cardiac MR," in *Medical Image Computing and Computer-Assisted Intervention; MICCAI*, vol. 5762, 2009, pp. 750–758.

[12] S. Mansor and J. Noble, "Local wall motion classification of stress echocardiography using a hidden Markov model approach," *International Symposium on Biomedical Imaging (ISBI) : From Nano to Macro*, vol. 1, pp. 1295–1298, 2008.

[13] G. Mercier and M. Lennon, "Support vector machines for hyperspectral image classification with spectral-based kernels methods," *IEEE International Geoscience and Remote Sensing Symposium*, vol. 1, no. C, pp. 288–290, 2003.

[14] O. Michailovich, R. Yogesh, and A. Tannenbaum, "Image segmentation using active contours driven by the bhattacharyya gradient flow," *IEEE Transaction on Image Processing*, vol. 16, no. 11, pp. 2787–2801, 2007.

[15] K. Polat and S. Günes, "A novel approach to estimation of e. coli promoter gene sequences: Combining feature selection and least square support vector machine," *Applied Mathematics and Computation*, vol. 190, no. 2, pp. 1574–1582, 2007.

[16] K. Polat, S. Güneş, and A. Arslan, "A cascade learning system for classification of diabetes disease: Generalized discriminant analysis and least square support vector machine," *Expert System Application*, vol. 34, pp. 482–487, 2008.

[17] K. Punithakumar, I. Ben Ayed, A. Islam, I. Ross, and S. Li, "Regional heart motion abnormality detection via information measures and unscented kalman filtering," in *Medical Image Computing and Computer-Assisted Intervention; MICCAI*, vol. 6361, 2010, pp. 409–417.

[18] Z. Qian, Q. Liu, D. N. Metaxas, and L. Axel, "Identifying regional cardiac abnormalities from myocardial strains using spatio-temporal tensor analysis," in *MICCAI2008*, vol. 5241, 2008, pp. 789–797.

[19] A. Suinesiaputra, A. Frangi, T. Kaandorp, H. Lamb, J. Bax, J. Reiber, and B. Lelieveldt, "Automated detection of regional wall motion abnormalities based on a statistical model applied to multislice short-axis cardiac MR images," *IEEE Transactions on Medical Imaging*, vol. 28, no. 4, pp. 595–607, 2009.

Chapter 5

Conclusion

5.1 General Discussion

The LV function is assessed using global indicators such as ejection fraction as well as local indicators such as segmental wall motion. In clinical practice, evaluation of the LV function relies on either visual assessment or manual segmentation and interpretation of global as well as segmental LV wall motion. As discussed in chapter one, visual assessments are subject to high inter-observer variabilities, and are inaccurate and non-reproducible procedures [16, 5]. Manual LV segmentation is also a subject-dependent and time-consuming process. This task is subject to intra and inter-observer variability.

We proposed accurate, real-time techniques for global and regional assessment of cardiac LV using MR images. The proposed methods can be used as a diagnostic tool to assist the radiologists in such assessments.

5.2 Cardiovascular Magnetic Resonance Imaging

As discussed in chapter one, CMR is an accurate and reproducible [7, 12, 8] imaging modality and patients can undergo several CMR scans without being exposure to ionizing radiation [20]. These features make it an ideal technique for monitoring the treatment and progression

of cardiac disease.

In this project, a set of 2D short-axis cine MR images of subjects was acquired through the cardiac cycle on a 1.5T scanner with fast-imaging employing steady-state acquisition (FIESTA) image sequence mode.

The experiments in chapters two, three and four have been done on a set of 20, 58 and 58 subjects respectively. The dataset used in chapters three and four contained short-axis image datasets (i.e., apical, mid-cavity and basal) from 21 normal and 37 abnormal hearts. The subject population included 41 males and 17 females with the average age of subjects being 52.3 ± 15.0 years. More details have been provided in each chapter.

The performance of the proposed techniques were compared with ground truths built by three experienced radiologists, each of whom annotated a different portion of the data set.

5.3   Global Assessment of Cardiac Function

We investigated a technique for global assessment of the LV in real-time by computing the cardiac Ejection Fraction (EF) in chapter two. The EF depends on the variation in the volume of the LV cavity during a cardiac cycle, and is an essential measure in the diagnosis of cardio-vascular diseases. It is often estimated via manual segmentation of several images in a cardiac sequence, which is prohibitively time consuming. Alternatively, automatic segmentation can be used, but this is a challenging and computationally expensive task that may result in high estimation errors .

We proposed to estimated the EF directly (without segmentation) from Magnetic Resonance image statistics via machine learning. From a simple user input in a single image, we built statistics for all the images in a subject dataset. These image statistics were based on the Bhattacharyya coefficients of similarity between image distributions, which were shown to be non-linearly related to the LV cavity areas. We used an ANN to find the relation between the image statistics and the corresponding LV cavity areas in each subject dataset.

We estimated the LV cavity area in each single image using a trained ANN. The LV cavity volume in each frame was estimated by integrating the corresponding areas. The EF were estimated from the volumes in end-diastole and end-systole.

A comprehensive experimental evaluation over 20 subjects demonstrated an excellent conformity between the automatically estimated EFs and those computed from manual segmentations. The proposed method yielded correlation coefficients of 0.89 and 0.91 for the LV cavity areas and volumes, respectively, indicating a high correlation between manual and automatic estimations. Moreover, we performed a comprehensive evaluation on the effect of user-provided input and ANN design. The proposed method relies on an approximate user-provided localization of the LV cavity. We evaluated the robustness of the method with respect to variation in user-provided input. We showed that the mean error is significantly increased by the size of the region enclosed within the user-provided curve. We also investigated the effect of the choice of number of neurons on the results.

Several comparisons with graph-cut and level-set estimation of the *EF* based on recent segmentation algorithms confirmed that the proposed method can yield a competitive performance, while significantly reducing the computational load.

5.4   Regional Assessment of Cardiac Function

Chapter three proposed a real-time method for automating the detection and localization of segmental (regional) myocardial abnormalities in MRI. The method is a machine-learning and image-statistic based approach to evaluate segmental LV function. As discussed in chapter three, in practice, assessment of the segmental cardiac function is considered an essential diagnosis and follow-up component [1]. It is often assessed *visually* following the American Heart Association (AHA) [2] standard, which prescribes selecting representative 2D cardiac slices so as to generate 17 standardized LV segments. Alternatively, automating the detection and localization of regional abnormality has recently been focus of research [15, 11, 21, 4, 14, 10].

126

Regardless of such effort, a fast and accurate technique is still desired.

The proposed technique requires minimal user input in only one frame in a subject image dataset. For all the regional segments and all subsequent frames we build a set of statistical MRI features based on the Bhattacharyya measure of similarity between distributions. We demonstrated that over a cardiac cycle the estimated statistical features are correlated with the proportion of blood within each segment, and can therefore be used to describe segmental contraction with minimal user effort. We found the optimal direction along which the proposed image features are most descriptive via a Linear Discriminant Analysis (LDA). Then, using the results as inputs to a Linear Support Vector Machine (LSVM) classifier, we estimated the abnormality of each standard cardiac segments in real-time.

We showed experimental evaluations of the proposed algorithm over 928 cardiac segments obtained from 58 subjects. We demonstrated the performance of the LSVM using (1) the ROC (Receiver Operating Characteristic) curves with the corresponding AUCs (Area Under the Curve) and (2) the Bhattacharyya measure [3] to evaluate the discriminative power of the features. Furthermore, we assessed the classifier performance with a leave-one-third-of-the-subjects-out approach, i.e., by training our algorithm using 2/3 of the dataset and testing on the remaining data. The proposed algorithm yielded an overall classification accuracy of 86.09% and a kappa measure of 0.73. We further reported meta-analysis comparisons with several recent methods, which showed that the proposed method can yield a competitive performance while reducing the computational load and user efforts.

In chapter four we studied the more general and challenging multi-class problem, where each regional segment is classified into one of four classes: (1) normal; (2) hypokinetic; (3) akinetic; and (4) dyskinetic. We built a set of statistical MRI features for all of the regional segments and subsequent frames using minimal user input in only one frame. These estimated features could be used to characterize segmental cavity and myocardium contraction without requiring manual segmentation of the LV in all frames. We used these features as inputs for a multi-class SVM classifier and obtained a 4-class assessment of each segment.

We assessed the performance of the proposed algorithm with three criteria: the accuracy, confusion matrix, and bulls eye plot. Experimental evaluation over 928 cardiac segments obtained from 58 subjects demonstrated the strong performance of the algorithm, with an overall 4-class accuracy of 74.14%.

5.5   Future Direction

In chapter two, the estimation of the EF relies on an approximate user-provided localization of the LV cavity, with the user being required to provide an initial box close the LV in a single 2D image. Since, the LV localization plays an important role in estimating the image features, LV localization has the potential to be fully automatic by applying, a localization technique. LV localization techniques based on blob detection, optical flow and machine learning techniques can be used to approximately find the LV location in the end-diastole frame. Such technique would be able to reduce the error (discussed in Fig. 2.25) caused by user input.

In chapters three and four, the proposed regional myocardial abnormality detection framework is based on image statistics. This framework requires user inputs, to specify an initial delineation and several anatomical landmarks on the first frame. Again in the future it would be interesting to fully automate the process to remove the possibilities of user bias or error.

In chapter four, we assessed the segmental cardiac dysfunction using a Support Vector Machine fed by statistical image features, based on a measure of similarity between distributions. The accuracy of the classification technique can potentially be improved through the use of alternative techniques:

1. The accuracy could be increased by training the SVM classifier with a large number of abnormal datasets. The proposed method produced comprehensive results for normal and hypokinetic segments because we had access to more dataset related to these conditions. We predict that by increasing the number of datasets corresponding to the other conditions, the accuracy for additional conditions could be improved.

2. The image features used in the proposed method are intensity based. Other robust image features, e.g., those based on the shape information could potentially be mixed with the current features to increase the accuracy.

Additional future work includes application of the proposed method to estimate other cardiac functions such as muscle thickening and right ventricle abnormality detection. The proposed method is based on the consistency of the image distributions within the cavity across different frames, and can therefore be readily extended to other modalities where such consistency is verified.

References

[1] G. Buckberg, "Left ventricular form and function: Scientific priorities and strategic planning for development of new views of disease," *Circulation*, vol. 110, pp. e333–e336, 2004.

[2] M. D. Cerqueira, N. J. Weissman, V. Dilsizian, A. K. Jacobs, S. Kaul, W. K. Laskey, D. J. Pennell, J. A. R. andThomas Ryan, and M. S. Verani, "Standardized myocardial segmentation and nomenclature for tomographic imaging of the heart," *Journal of the American Heart Association*, vol. 105, pp. 539–542, 2002.

[3] D. Comaniciu, V. Ramesh, and P. Meer, "Kernel-based object tracking," *IEEE Transactions on Pattern Analysis and Machine Intelligence*, vol. 25, no. 5, pp. 564–577, 2003.

[4] J. Garcia-Barnes, D. Gil, L. Badiella, A. Hernàndez-Sabaté, F. Carreras, S. Pujadas, and E. Martí, "A normalized framework for the design of feature spaces assessing the left ventricular function," *IEEE Transaction on Medical Imaging*, vol. 29, no. 3, pp. 733–745, 2010.

[5] R. Hoffmann, S. von Bardeleben, J. D. Kasprzak, A. C. Borges, F. ten Cate, C. Firschke, S. Lafitte, N. Al-Saadi, S. Kuntz-Hehner, G. Horstick, C. Greis, M. Engelhardt, J. L. Vanoverschelde, and H. Becher, "Analysis of regional left ventricular function by cineventriculography, cardiac magnetic resonance imaging, and unenhanced and contrast-enhanced echocardiography: A multicenter comparison of methods," *Journal of Amercican College of Cardiology*, vol. 47, no. 1, pp. 121–128, 2006.

[6] T. D. Karamitsos, J. M. Francis, S. Myerson, J. B. Selvanayagam, and S. Neubauer, "The role of cardiovascular magnetic resonance imaging in heart failure," *Journal of the American College of Cardiology*, vol. 54, no. 15, pp. 1407–1424, 2009.

[7] T. D. Karamitsos, L. E. Hudsmith, J. B. Selvanayagam, S. Neubauer, and J. M. Francis, "Operator induced variability in left ventricular measurements with cardiovascular magnetic resonance is improved after training," *Journal of Cardiovascular Magnetic Resonance*, vol. 9, pp. 777–783, 2007.

[8] P. J. Kilner, P. D. Gatehouse, and D. N. Firmin, "Flow measurement by magnetic resonance: a unique asset worth optimising," *Journal of Cardiovascular Magnetic Resonance*, vol. 9, pp. 723–728, 2007.

[9] T. Kuznetsova, L. Herbots, Y. Jin, K. Stolarz-Skrzypek, and J. A. Staessen, "Systolic and diastolic left ventricular dysfunction: from risk factors to overt heart failure," *Expert Review of Cardiovascular Theroapy*, vol. 8, no. 2, pp. 251–258, 2010.

[10] K. Lekadir, N. Keenan, D. Pennell, and G. Yang, "An inter-landmark approach to 4-D shape extraction and interpretation: Application to myocardial motion assessment in MRI," *IEEE Transactions on Medical Imaging*, vol. 30, no. 1, pp. 52 –68, 2011.

[11] Y. Lu, P. Radau, K. Connelly, A. Dick, and G. Wright, "Pattern recognition of abnormal left ventricle wall motion in cardiac MR," in *Medical Image Computing and Computer-Assisted Intervention; MICCAI*, vol. 5762, 2009, pp. 750–758.

[12] H. Mahrholdt, A. Wagner, T. A. Holly, M. D. Elliott, R. O. Bonow, R. J. Kim, and R. M. Judd, "Reproducibility of chronic infarct size measurement by contrast-enhanced magnetic resonance imaging," *Circulation*, vol. 106, pp. 2322–2327, 2002.

[13] C. Petitjean and J.-N. Dacher, "A review of segmentation methods in short axis cardiac MR images," *Medical Image Analysis*, vol. 15, no. 2, pp. 169–184, 2011.

[14] K. Punithakumar, I. Ben Ayed, A. Islam, I. Ross, and S. Li, "Regional heart motion abnormality detection via information measures and unscented kalman filtering," in *Medical Image Computing and Computer-Assisted Intervention; MICCAI*, vol. 6361, 2010, pp. 409–417.

[15] Z. Qian, Q. Liu, D. N. Metaxas, and L. Axel, "Identifying regional cardiac abnormalities from myocardial strains using spatio-temporal tensor analysis," in *Medical Image Computing and Computer-Assisted Intervention; MICCAI*, vol. 5241, 2008, pp. 789–797.

[16] A. Redheuil, N. Kachenoura, R. Laporte, A. Azarine, X. Lyon, O. Jolivet, F. Frouin, and E. Mousseaux, "Interobserver variability in assessing segmental function can be reduced by combining visual analysis of CMR cine sequences with corresponding parametric images of myocardial contraction." *Journal of Cardiovascular Magnetic Resonance*, vol. 9, no. 6, pp. 863–72, 2007.

[17] V. L. Roger and et.al, "Heart disease and stroke statistics2012 update: A report from the American Heart Association," *Circulation*, vol. 125, pp. e2–e220, 2012.

[18] A. Sarwar, M. D. Shapiro, S. Abbara, and R. C. Cury, "Cardiac magnetic resonance imaging for the evaluation of ventricular function," *Seminars in Roentgenology*, vol. 43, pp. 183–192, 2008.

[19] J. Selvanayagam, S. Westaby, K. Channon, J. Francis, J. Eichhfer, S. Saito, and S. Neubauer, "Images in cardiovascular medicine. surgical left ventricular restoration: an extreme case." *Circulation*, vol. 107, p. e71, 2003.

[20] F. G. Shellock and J. V. Crues, "MR procedures: biologic effects, safety, and patient care," *Radiology*, vol. 232, pp. 635–652, 2004.

[21] A. Suinesiaputra, A. Frangi, T. Kaandorp, H. Lamb, J. Bax, J. Reiber, and B. Lelieveldt, "Automated detection of regional wall motion abnormalities based on a statistical model

applied to multislice short-axis cardiac MR images," *IEEE Transactions on Medical Imaging*, vol. 28, no. 4, pp. 595–607, 2009.

[22] T. F. Walsh and W. G. Hundley, "Assessment of ventricular function with cardiovascular magnetic resonance," *Magnetic Resonance Imaging Clinics of North America*, vol. 15, no. 4, pp. 487 – 504, 2007.

Office of Research Ethics

The University of Western Ontario

Western

Use of Human Subjects - Ethics Approval Notice

Principal Investigator: Dr. I. Ross

Review Number: 16634E

Review Date: December 04, 2009

Review Level: Expedited

Approved Local # of Participants: 100

Protocol Title: Computer assisted image based cardiac disease diagnosis and monitoring

Department and Institution: Imaging, London Health Sciences Centre

Sponsor: NSERC-NATURAL SCIENCES ENGINEERING RSRCH COU

Ethics Approval Date: July 20, 2010

Expiry Date: December 31, 2014

Documents Reviewed and Approved: UWO Protocol

Documents Received for Information:

This is to notify you that The University of Western Ontario Research Ethics Board for Health Sciences Research Involving Human Subjects (HSREB) which is organized and operates according to the Tri-Council Policy Statement: Ethical Conduct of Research Involving Humans and the Health Canada/ICH Good Clinical Practice Practices: Consolidated Guidelines; and the applicable laws and regulations of Ontario has reviewed and granted approval to the above referenced study on the approval date noted above. The membership of this REB also complies with the membership requirements for REB's as defined in Division 5 of the Food and Drug Regulations.

The ethics approval for this study shall remain valid until the expiry date noted above assuming timely and acceptable responses to the HSREB's periodic requests for surveillance and monitoring information. If you require an updated approval notice prior to that time you must request it using the UWO Updated Approval Request Form.

During the course of the research, no deviations from, or changes to, the protocol or consent form may be initiated without prior written approval from the HSREB except when necessary to eliminate immediate hazards to the subject or when the change(s) involve only logistical or administrative aspects of the study (e.g. change of monitor, telephone number). Expedited review of minor change(s) in ongoing studies will be considered. Subjects must receive a copy of the signed information/consent documentation.

Investigators must promptly also report to the HSREB:

a) changes increasing the risk to the participant(s) and/or affecting significantly the conduct of the study;
b) all adverse and unexpected experiences or events that are both serious and unexpected;
c) new information that may adversely affect the safety of the subjects or the conduct of the study.

If these changes/adverse events require a change to the information/consent documentation, and/or recruitment advertisement, the newly revised information/consent documentation, and/or advertisement, must be submitted to this office for approval.

Members of the HSREB who are named as investigators in research studies, or declare a conflict of interest, do not participate in discussion related to, nor vote on, such studies when they are presented to the HSREB.

Chair of HSREB: Dr. Joseph Gilbert
FDA Ref. #: IRB 00000940

Curriculum Vitae

Education
Ph.D. Candidate, Biomedical Engineering   **2008-Present**
The University of Western Ontario, London, Canada
> "**Automatic Estimation of Left Ventricle Cardiac Function from MR Images**"
> **Advisors:** Dr. Terry Peters & Dr. Shuo Li

Masters of Engineering Science (M.E.Sc.), Electrical Engineering   **2005-2007**
The University of Science and Technology, Tehran, Iran
> "**Background modeling and producing a panoramic image from video frames**"

Bachelor of Engineering Science (B.E.Sc.), Electrical Engineering   **1998-2003**
Semnan University, Semnan, Iran

Engineering Employment Experience
Digital Imaging Group of London   **2008-Present**
GE-Healthcare, London, Canada
Robarts Research Institute, London, Canada
Research Assistant:

- Improved cardiovascular disease prognosis using MRI
- Developed algorithm for global assessment of heart function
- Estimated essential criterion (Ejection Fraction) for cardiac evaluation
- Presented a technique for regional cardiac assessment.
- Produced MRI cardiac report to facilitate radiologist diagnostic procedure
- Published pioneer research work in several medical Imaging Journals and International conferences

Western University (UWO), London, Canada   **2008-Present**
Graduate Teaching Assistant
- Lectured various undergraduate courses
- Prepared technical presentation for course material
- Evaluation of student performance on assignments and laboratory reports

University of Rafsanjan, Department of Physics, Rafsanjan, Iran   **2007-2008**
Lecturer
- Selected taught courses: Advanced Physics, Electrical Circuit Theory
- Taught laboratories: Introduction to Electronics, Advanced Physics

Nasb-Ehdas Company, Tehran, Iran   **2005-2007**
Project Manager
- Supervised the manufacturing machinery regular maintenance
- Worked closely with the maintenance staffs to ensure the quality of work
- Prepared monthly reports of the operation for the supervisors regular meetings

Nasb-Ehdas Company, Tehran, Iran   **2003-2005**
Design Engineer
- Designed and implemented machinery test protocols and equipments
- Trained new employees on the simulation tools and performing studies

Siemens Corporation, Tehran, Iran   **2003**
Undergraduate Internship
- Prepared technical summaries from IEEE transactions and standards
- Assisted senior engineers with design of AC/DC panel board
- Provided statistics to other lines of business

Tutor,   **1999-2003**
(Physics and Applied mathematics for Engineering)
- Developed lessons designed to meet the goals and needs of engineering students
- Documented monthly summaries of the materials covered and the student's accomplishments

---

Skills and Qualifications
- Able to communicate and work with people from different academic backgrounds
- Self-motivated and strong problem-solver, Experienced trainer and organizer
- Excellent co-ordination, project management and team work abilities
- Fast learner with the ability to apply knowledge independently or co-operatively
- Extensive experience in research, teaching and experimental work
- Committed to the challenging work
- Reliable, responsible and hardworking with strong professional ethics
- Excellent oral communication skills developed through various presentations and seminars

Computer proficiency:

Productivity	MS Office (Outlook, Excel, Word, and Power Point, Access), MS project, LaTex
Electrical Engineering	Hspice, Ledit, Work Bench, Pspice
Embedded software development	VHDL programming, FPGA (Max+plusII), Micro Controller (8051)
Medical Imaging Software:	3D Slicer, VTK, ITK
Technical Software:	Matlab, Visual Studio (Visual C++), Quick Basic

Professional Associations/Scientific Societies

- Chair, Engineering in Medicine and Biology Society (EMBS) student chapter of London, Canada
- Graduate Coordinator, Canadian Student Conference in Biomedical Computing Engineering 2010 (CSCBCE)
- Social Event Coordinator, Biomedical Engineering Department, UWO
- Seminar organizer, Canadian Institute of Health Research (CIHR) Strategic Training Program in Vascular research, Robarts Research Institute
- Journal club organizer, Digital Imaging Group of London

Honors and Awards

- Western Graduate Research Scholarship
- NSERC Collaborative Research and Training Experience (CREATE) Program in Computer-Assisted Medical Interventions
- Canadian Institute of Health Research (CIHR), Vascular Training Program
- Graduate Thesis Research Award
- Travel Bursary Award
- Ranked 2nd among Master students in Department of Electrical Engineering at University on Science & Technology in Iran

Publications

1) Afshin, M., Ben Ayed, I., Punithakumar, K., Islam, A., Goela, A., Ross, I., Peters, T.M., Li, S., "Global Assessment of Cardiac Function using Image Statistics in MRI", Medical Image Computing and Computer Assisted Interventions (MICCAI), Vol 7511, pp. 535-543 (2012).

2) Afshin, M., Ben Ayed, I., Islam, A., Goela, A., Ross, I., Peters, T.M., Li, S, "Estimation Of The Ejection Fraction From Image Statistics", IEEE International Symposium on Biomedical Imaging (ISBI), pp. 824-827 (2012).

3) Afshin, M., Ben Ayed, I., Neshat, H.R., Islam, A., Goela, A., Peters, T.M., Li, S., "Regional Assessment of Cardiac Left Ventricle from MRI with Minimum User Interaction", Radiological Society of North America (RSNA 2012).

4) Afshin, M., Ben Ayed, I., Punithakumar, K., Law, M.W.K., Islam, A., Ross, I., Peters, T.M., Li, S., "Assessment of Regional Myocardial Function via Statistical Features in MR Images", Medical Image Computing and Computer Assisted Interventions (MICCAI), Vol 6893, pp.107-114 (2011).

5) Afshin, M., Ben Ayed, I., Islam, A., Ross, I., Peters, T.M., Li, S., "Variational Level-Set Segmentation and Tracking of Left Ventricle Using Field Prior", Proc. SPIE 7962, 79622D (2011).

6) Afshin, M., Ben Ayed, I., Islam, A., Goela, A., Ross, I., Peters, T.M., Li, S., "Estimation of the Cardiac Ejection Fraction From Magnetic Resonance Image Statistics", under second revision in IEEE Transaction on Biomedical Engineering.

7) Afshin, M., Ben Ayed, I., Punithakumar, K., Islam, A., Goela, A., Ross, I., Peters, T.M., Li, S., "Regional Assessment of Cardiac Left Ventricular Myocardial Function via MRI Statistical Features", under revision in IEEE Transaction on Medical Imaging.

8) Afshin, M., Ben Ayed, I., Islam, A., Goela, A., Ross, I., Peters, T.M., Li, S., "Automatic Diagnosis of Segmental Cardiac Dysfunction via Statistical Features in Short-axis MRI", under revision in Journal of Cardiovascular Magnetic Resonance.